MIT

LANDSURFACE HYDROLOGY PARAMETERIZATION FOR ATMOSPHERIC GENERAL CIRCULATION MODELS: INCLUSION OF SUBGRID SCALE SPATIAL VARIABILITY AND SCREENING WITH A SIMPLE CLIMATE MODEL

by
DARA ENTEKHABI
and
PETER S. EAGLESON

RALPH M. PARSONS LABORATORY
HYDROLOGY AND WATER RESOURCE SYSTEMS

DEPARTMENT
OF
CIVIL
ENGINEERING

SCHOOL OF ENGINEERING
MASSACHUSETTS INSTITUTE OF TECHNOLOGY
Cambridge, Massachusetts 02139

Report Number 325

Prepared under the support of the
National Aeronautics and Space Administration

September, 1989

R89–23

LANDSURFACE HYDROLOGY PARAMETERIZATION FOR ATMOSPHERIC GENERAL CIRCULATION MODELS: INCLUSION OF SUBGRID SCALE SPATIAL VARIABILITY AND SCREENING WITH A SIMPLE CLIMATE MODEL

by

Dara Entekhabi

and

Peter S. Eagleson

RALPH M. PARSONS LABORATORY

HYDROLOGY AND WATER RESOURCE SYSTEMS

Report Number 325

Prepared under the support of the
National Aeronautics and Space Administration
Grant No. NAG 5–743

SEPTEMBER 1989

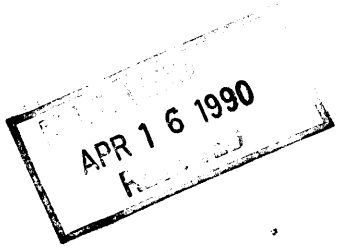
APR 1 6 1990

Abstract

Parameterizations are developed for the representation of subgrid hydrologic processes in atmospheric general circulation models. Reasonable a priori probability density functions of the spatial variability of soil moisture and of precipitation are introduced. These are used in conjunction with the deterministic equations describing basic soil moisture physics to derive expressions for the hydrologic processes that include subgrid scale variation in parameters. The major model sensitivities to soil type and to climatic forcing are explored offline of the climate model.

For more comprehensive sensitivity analyses, a one–dimensional model equipped with GCM physical parameterizations is used. The dynamic heat and moisture convergence are parameterized. The advantages of online sensitivity analyses with this one–dimensional model is that the major model climate landsurface–atmosphere feedbacks are essentially reproduced in this simple GCM analog. The climate model is then used to screen various alternatives and sensitivity simulation experiments.

Acknowledgements

This work has been supported by the National Aeronautics and Space Administration Grant NAG 5–743. We thank Professors Rafael L. Bras and Peter H. Stone of M.I.T., and Drs. David Rind and Randy Koster of NASA for their assistance.

Table of Contents

List of Figures

Page

Chapter II

Chapter III

Chapter IV

List of Tables

I. Introduction

The hydrologic cycle is imbedded in the general circulation of the atmosphere. Consequently, water balance at the surface and subsurface is strongly coupled with the patterns and behavior of the climatic system and the capability to simulate and predict the general circulation of the atmospheric fluid is thus of great relevance to hydrology.

Climatic general circulation models (GCMs) have been devised to reproduce the basic patterns and processes in the atmospheric system. These models are based on the numerical solution to equations describing flow in the atmospheric fluid at every node in a three–dimensional mesh representing the global atmosphere. The set of equations include the momentum conservation equation, the first law of thermodynamics, mass continuity equation, and the ideal gas law. Effects not solved for with these equations, such as solar insolation, thermal radiation, clouds, precipitation processes, etc. are parameterized. Beginning with few simple inputs, these climate GCMs produce the general seasonal and geographical patterns of global climate with remarkable realism.

The storage and flowpaths of water in the earth–atmosphere system are central to the proper simulation of weather patterns and climate. Coupled landsurface water and heat balances have strong influences on the intensity and patterns of atmospheric flow. Water has further significant effects on the model–simulated climate; the extent of polar ice caps affect the global heat budget, the amount of atmospheric water vapor determines its radiative properties, and large amounts of heat are involved in water phase changes. The accurate representation of the hydrological cycle and all its branches (atmospheric, surface, and ground storage) are of central importance in successful general circulation modeling.

GCMs are gateways to a fresh approach to the two basic tenets of hydrologic

science; the hydrologic cycle and water balance. The GCM can serve as the experimental apparatus for studying the spatial and temporal patterns in the atmospheric and surface branches of the hydrologic cycle. Furthermore, with climate models, the large–scale water balance and hydrology may be analyzed for their influences on regional climate. The role of landsurface–atmosphere feedbacks that are critical in the maintenance of the climatic system may be examined using GCMs.

Numerous experiments in regional hydrology may be performed using climate GCMs. Scenarios of climate change produced by increasing carbon dioxide, paleoclimate conditions, modified landsurfaces, etc. may be explored with these models. Most importantly, climate GCMs may finally allow hydrologists to study the atmospheric branch of the hydrological cycle; an important hydrologic process, so far neglected due to the lack of the proper research tool.

Some topics in the agenda of global hydrology may be approached directly using GCMs. The issue of teleconnections, the association of distant and disparate processes with the climate of a region, may be analyzed in a controlled manner using GCMs. The degree of local water recycling in an area, i.e. local evaporation versus oceanic sources for the precipitation of a region, is an additional global hydrology issue that GCM studies can clarify. Since much of the variability in the hydrologic cycle is introduced through the atmospheric branch, the traditional water–supply concerns of hydrologists may be addressed more effectively by expanding the analysis of the hydrologic cycle to include its atmospheric branch.

There are, however, numerous GCM components that require significant improvement before these models can be used operationally and for regional studies. The surface hydrology parameterization is chief among them. Most GCMs in current use are equipped with rather simplistic, one–dimensional, empirical runoff ratio and evapotranspiration efficiency functions (Carson, 1982)(runoff ratio is the

ratio of the surface precipitation excess to the incident precipitation; evapotranspiration efficiency is the ratio of the actual to the potential evapotranspiration). Reliable and physically–based relations for determining the surface rainfall excess, evaporation, plant transpiration, snow and permafrost thermodynamics, and other surface processes are needed. Given that GCM grids are typically 10^4 to 10^5 km^2, the significant effects of spatial heterogeneities on surface hydrology also need to be parameterized.

New parameterizations for the runoff ratio and evapotranspiration efficiency functions are introduced in Chapters II and III here. These functions are distinct from earlier ones in that they explicitly account for some of the subgrid heterogeneity in hydrologic conditions. Furthermore, the new parameterizations attempt to incorporate some physically–based equations where empirical ones governed before. In order to introduce the hydrologic model developed herein, and in order to delineate it from earlier and concurrent efforts, a brief history of the problem is presented below. This history includes some survey of literature; one, that is geared more towards outlining the foundations of the problem rather than summarizing its entire bibliographic history.

1. Selective summary of literature

The recognition that hydrologically– and thermodynamically–active upper soil and vegetation layers are indispensable to the proper description of climate is evident in the early elucidations of the numerical climate simulation idea itself. In 1922, Lewis F. Richardson published *Weather Prediction by Numerical Process* where he proclaimed: "The atmosphere and the upper layers of the soil or sea form together a united system...A forecast for the land and sea might be attempted concurrently with that for air. Let this be the ideal which we here set before us...The changes in the soil may be described by two differential equations, one for

the conduction of heat, the other for the transference of water."

Since then, various GCM modelling groups have adopted different but equally simple and empirical equations in order to represent the surface hydrology in their numerical models of climate. Recently, more complex soil hydrology and vegetation canopy models have been introduced (Dickinson et al., 1981; Sellers et al., 1986). These latter models are basically composed of multiple and discrete soil and vegetation layers linked by a series of resistances representing plant stomatal control and/or soil diffusivity. L. F. Richardson, in 1922, was quite aware of this possibility when he wrote: "By analogy with electric conduction, the rate of transpiration may be said to be inversely as the resistance of the stomata...The resistance consists of two parts in series...The rate of motion of vapour (in unsaturated soils, *D.E.*) will be proportional to the gradient of density $\frac{\partial F}{\partial z}$." The conceptual basis for the treatment of landsurface hydrologic processes in numerical models of climate is apparent even in the early exposition of L. F. Richardson. Since then, GCM modellers have tried to capture the difficult problem within the confines of simple parameterizations.

Almost by definition, a parameterization, as opposed to a solution, implies that compromises have been made.

Clearly, the scale of landsurface hydrologic processes is grossly incompatible with the dimensions of GCM grid areas. The first compromise is, therefore, to assume that a large land area may be modelled as a uniform hydrologic unit. Each GCM grid is hence characterized by prognostics that are assumed to be representative of all points within the region.

Since GCMs as a whole consume enormous amounts of computer resources, all constituitive modules and parameterizations are constrained to be as parsimonious and efficient as possible. Accordingly, the landsurface hydrologic parameterizations in most GCMs have applied simple functions relating runoff to precipitation and

actual evapotranspiration to potential evaporation. Mostly, these are linear or broken–linear functions where the constant of proportionality is a fraction of the relative soil saturation in the topmost soil layer. For example, Equations E7 and E8 represent the runoff ratio and evaporation efficiency functions employed in the NASA Goddard Institute for Space Studies GCM.

As mentioned earlier, the landsurface hydrology parameterization of GCMs is chiefly composed of the runoff ratio and the evapotranspiration efficiency functions. These are dimensionless expressions for the runoff and evapotranspiration rates normalized by the precipitation and potential evaporation rates respectively. Hence the precipitation and potential evaporation are forcing terms of the landsurface hydrologic parameterization. The precipitation rate at the surface results from the analyses in the atmospheric component of GCMs. The potential evaporation is the evaporation from a free water surface at ground temperature. The evaporation rate, in this case, is proportional to the vertical gradient in vapor partial pressures between the surface and a level in the atmosphere. The constant of proportionality is related to the static stability within the confined air layer and it is parameterized as a function of temperature gradients and wind speed.

The basic consequence of including a porous soil layer at the atmospheric surface boundary is to dampen the mass and energy fluxes across this boundary. The moisture mass added to the soil store is released back to the atmosphere with delays considerably longer than that characteristic of moisture residence in the atmosphere. The time scale associated with soil moisture depletion is on the order of tens of days.

Similarly, the thermal capacity of a soil layer is significantly higher than that of the overlying atmospheric column. Thus the energy flux across the lower boundary of the atmosphere is stored and then returned with a delay.

Both the thermal and moisture mass capacities of the soil store, which

determine its effectiveness as a 'porous' boundary condition to the numerical climate model, are critically dependent on the depth assumed for the soil layer. The depth of the surface soil layer is thus an important *parameter* in GCMs. The inclusion of multiple soil layers has been used as a method to increase the capacity of the soil reservoir and thus further dampen the seasonal and diurnal cycles in the model boundary conditions.

More recent and altogether new approaches to the landsurface hydrology parameterization are based on multiple soil and canopy levels. Dickinson et al. (1981) developed the Biosphere–Atmosphere Interaction Scheme (BATS) with two soil layers and a single canopy level. Sellers et al. (1986) construct a similar model, the Simple Biosphere (SiB) model, that includes three soil stores and two canopy levels. In both SiB and BATS the moisture flux between soil layers, infiltration, and exfiltration are all based on resistance formulation. As for the canopy, it is assumed that the intercellular spaces in leaves are saturated. The stomatal resistances are parameterized as functions of vegetation type and climatic conditions.

Though SiB and BATS are more physically–based than landsurface hydrology parameterizations in current GCMs (i.e. those that define the runoff ratio and evapotranspiration efficiency as linear or broken–linear functions of soil moisture), they nevertheless assume surface homogeneity of conditions over the GCM grid area. The recognition that the subgrid spatial heterogeneity of surface conditions, especially that of the surface soil moisture, are essential to the realistic formulation of the GCM landsurface hydrologic parameterization prompted an alternative approach to evapotranspiration modelling in GCMs. Wetzel and Chang (1987, 1988) estimate areally–averaged evapotranspiration rates when, at subgrid scale, the surface soil moisture is normally distributed about the grid mean value. Using transpiration and bare soil evaporation equations similar to SiB and BATS, they

compute the fluxes at several different soil moisture values and then find the grid mean rate by numerically weighting according to the discretized normal distribution.

2. Overview of report contents

The approach followed here addresses the concerns that prompted both the development of SiB and BATS as well as the extensions that include subgrid heterogeneities. In Chapter II, parameterizations for the runoff ratio, bare soil evaporation efficiency, and transpiration efficiency functions are developed that are both physically–based and incorporate the effects of subgrid spatial variability in some conditions. The parameterizations in Chapter II account for the subgrid heterogeneity of surface soil moisture by prescribing a statistical distribution to the point values. Then using the physically–based equations of infiltration, exfiltration, and root soil water extraction, analytical expressions for areally–averaged fluxes are derived using the statistical distributions. The runoff parameterization also accounts for the fractional coverage of storms over grid areas and the mesoscale structure of point rainfall intensity within storms.

The parameterizations in Chapter II are closed–form mathematical expressions that are nonlinear functions of the grid–mean soil moisture, rainfall, and potential evaporation. The expressions are conditional on soil type, vegetation type, fractional wetting by rainfall, and the prescribed degree of spatial variability in surface soil moisture. These parameterizations constitute the basic outline of the statistical–dynamical approach to the modelling of surface moisture fluxes in GCMs. In Chapter III, a series of extensions to the basic outline are made. The transpiration efficiency function is modified to include an alternative root soil water extraction expression. Furthermore, the possibility of multiple soil layering and root soil water extraction from deeper soil levels is incorporated into the

transpiration efficiency function in a consistent manner. Lastly, in Chapter III, the evapotranspiration parameterization is modified to include the effects of subgrid energy advection when the soil or the vegetation reduce the rate of moisture loss below the atmospheric evaporative demand.

The behavior and sensitivities of the landsurface hydrologic parameterization including subgrid scale spatial variability developed in Chapters II and III (hereafter referred to simply as the subgrid hydrology) are investigated both analytically and numerically within a climate model. Implicitly in every landsurface hydrologic parameterization, there is an equilibrium value for soil moisture when the climatic conditions are held constant. With a given set of runoff ratio and evapotranspiration efficiency functions, one may analytically solve the inverse problem for the longterm mean soil moisture based on the prescribed precipitation and potential evaporation atmospheric forcing. In Appendix E, the sensitivity of the equilibrium surface relative soil saturation to climate is investigated in this manner. Comparisons are made between the climates resulting from the subgrid hydrology model and the current soil hydrology parameterization in the GCM at NASA Goddard Institute for Space Studies.

There are, however, numerous landsurface–atmosphere feedbacks that are not apparent in the analytic study of Appendix E. The water and energy balance at the surface are strongly coupled. Alterations and shifts in one will results in modifications of the other. Furthermore, the precipitation regime is strongly affected by the degree of local water and heat recycling which is partly determined by the GCM landsurface parameterization. It is thus necessary to test the subgrid hydrology parameterization of Chapters II and III within a numerical climate model environment.

Ideally, the new hydrologic parameterization should be implemented in a full three–dimensional GCM where all the model feedbacks are present. However, in

order to perform numerous sensitivity tests efficiently, a simplified numerical climate model is used. In Chapter IV, the basic construct of a one–dimensional (in the vertical) climate model is outlined. This model solves the physical processes in a GCM (i.e. radiation, precipitation processes, soil hydrology) and parameterizes the dynamic convergence of heat and moisture. Its basic structure is similar to that of an atmospheric column over one GCM grid.

The major landsurface–atmosphere feedbacks in GCMs are due to the physical processes. There are, however, some geographical feedbacks resulting from the pattern of dynamic mass fluxes in the numerical climate model. The simplified one–dimensional climate model does capture most of the physical feedbacks but it cannot realistically reproduce the geographic influences due to the GCM's dynamical component.

In the introduction to Chapter IV, basic issues in using simplified climate models are discussed. The advantages and shortcomings are outlined as well. The simplified one–dimensional climate model is a screening tool that serves to narrow the focus of subsequent sensitivity tests with the full three–dimensional GCM.

II. Landsurface Hydrology Parameterization for Atmospheric General Circulation Models Including Subgrid Scale Spatial Variability

1. *Introduction*

In this chapter we derive runoff ratio and evapotranspiration efficiency functions that incorporate spatial variability through simple assumptions about the statistical distribution of the relevant parameters at the subgrid scale. Throughout we strive for computational economy, use only dimensionless variables, and remain as true as possible to the physics of the problem.

Vertical soil infiltration and exfiltration processes are affected by gravity and soil capillary forces. The parameterizations introduced here incorporate both these effects and demonstrate the relative magnitude of each for different soil types and wetness conditions.

2. *Infiltration and runoff*

a. *Mechanics of runoff generation*

Surface runoff is generated, for the most part, by the independent interaction of several spatially variable processes. The excess of precipitation intensity over soil infiltrability at a point, and the occurrence of precipitation over saturated and impermeable surfaces have been identified as two major mechanisms of inducing surface runoff. The former type of runoff is generally referred to as Horton runoff in the hydrologic literature (Freeze, 1974). Its occurrence is limited to localized areas of low permeability experiencing intense rainfall. The latter type of surface runoff mentioned above is largely responsible for the rapid response of streams to precipitation. Hewlett (1961) and Hewlett and Hibbert (1965) suggested that expanding saturated zones along hill and valley bottoms result in a *partial area* contribution to storm runoff. All precipitation over these areas that are saturated

by the rising shallow water table becomes surface runoff. Dunne and Black (1970) later produced observational evidence of this partial area contribution, and in most hydrologic literature the term Dunne runoff is employed to denote this mechanism of surface flow generation. We will incorporate both the Horton and Dunne processes in our parameterization of surface runoff.

For GCM grid area scales, the area–average precipitation intensity rarely assumes magnitudes exceeding the area–averaged soil infiltrabilities. The conventional spatial averaging inherent in GCM area discretization thus restricts the generation of surface runoff to those rare cases of intense precipitation over grid areas of low average permeability and high average water table. Subdivision of the GCM grid into smaller units of variable properties has been explored by Koster et al. (1988) as a solution to this problem. They find the technique useful for off–line sensitivity studies but costly for use in operational GCMs.

An alternative approach to the increasing of GCM resolution or the further subdivision of the landsurface component into smaller units is to regard a few relevant grid prognostics as the area–means of variables that have subgrid variance in the manner of Warrilow et al. (1986). This is analogous to the treatment of temporal variability by Eagleson (1978c) in his one–dimensional model of the average annual water balance. The current focus on surface runoff generation warrants treating the grid precipitation and the surface soil layer's hydraulic state as such distributed parameters.

b. Fractional wetting by precipitation

Precipitation over the grid area is determined by the combined, and sometimes coupled, moist–convective and large–scale condensation schemes of GCMs. Generally, fractions of grid volumes are treated as parcels that are forced to rise until convective stabilization governs the entire affected atmospheric profile.

he fraction may be a constant or a variable, in which case it is dependent on convergence and vertical fluxes in the lower troposphere. Vapor condensates are allowed to evaporate as they fall through the atmospheric layers. Separately, and often simultaneously, any cases of supersaturation within the grid volumes are regarded as large–scale condensation. After satisfying all the conditions of precipitation formation and re–evaporation, any residual at the lowest atmospheric layer is regarded as precipitation reaching the land surface and is distributed uniformly over the entire grid area. Given the typically large area of individual GCM surface grids and the long time increments in GCM integration, the model precipitation intensities reaching the surface are generally unrealistically low. Furthermore, given the scale of typical GCM grid areas, storm coverages may only be fractional. We thus recognize the need for fractional wetting parameterization within GCMs.

Let us define that, at any time for each grid, a fraction κ of the grid area is affected by precipitation reaching the surface. The parameter κ may be related to the plume fraction of the grid volume that is active during moist–convective events. Theoretical and observational studies of κ are found in the literature (Eagleson 1984; Eagleson and Wang 1985; Eagleson et al. 1987). We follow Warrilow et al. (1986) in assuming that over fraction κ of the GCM grid area, the point precipitation intensity at any time, P, is exponentially distributed, with mean $E[P]/\kappa$, as in

$$f_P(P) = \frac{\kappa}{E[P]} e^{-\frac{\kappa P}{E[P]}} \quad P > 0. \tag{2.1}$$

The parameter κ represents the scaling necessary to redistribute the GCM grid precipitation over the typical scale of precipitation events (mesoscale). Depending

on the governing GCM spatial and temporal resolution, κ ranges between zero and one. The expectation of precipitation over the entire grid area, E[P], is taken as the GCM resultant simulation of all precipitation reaching the land surface, due to moist–convective and large scale condensation events, at any time step over any grid area. Figure 2.1 illustrates the observed spatial variability of total storm depth for air mass thunderstorm rainfall in Arizona (Eagleson et al. 1987) in which case κ is about 0.66 . Over the storm–affected fraction κ of the grid area, the point precipitation intensity is distributed such that there are lesser areas of high intensity corresponding to the tail of the probability density function (pdf) in (1).

c. Spatial heterogeneity of soil hydraulic conditions

The ground hydrology in current GCMs is modeled using a layered system of soils with known hydraulic properties. For each grid area the soil of each layer is usually defined as a hybrid yet spatially invariant type and is characterized by a spatially uniform pattern of water content.

Important hydrologic processes depend on the heterogeneity of soil hydraulic conditions. At the soil surface, infiltration and exfiltration, hence runoff and bare soil evaporation, depend on the distributed nature of soil properties and states. These include type, texture, permeability, slope, elevation, and water content.

The surface runoff process is strongly and nonlinearly dependent on the soil water content in particular. The Horton component of surface runoff is the residual of precipitation intensity over the soil infiltrability, and the latter is highly sensitive to soil moisture conditions. The Dunne component of surface runoff is directly related to localized areas where the moisture content θ in the first soil layer equals the saturation value θ_{sat}. This chiefly applies to the low–land areas along stream

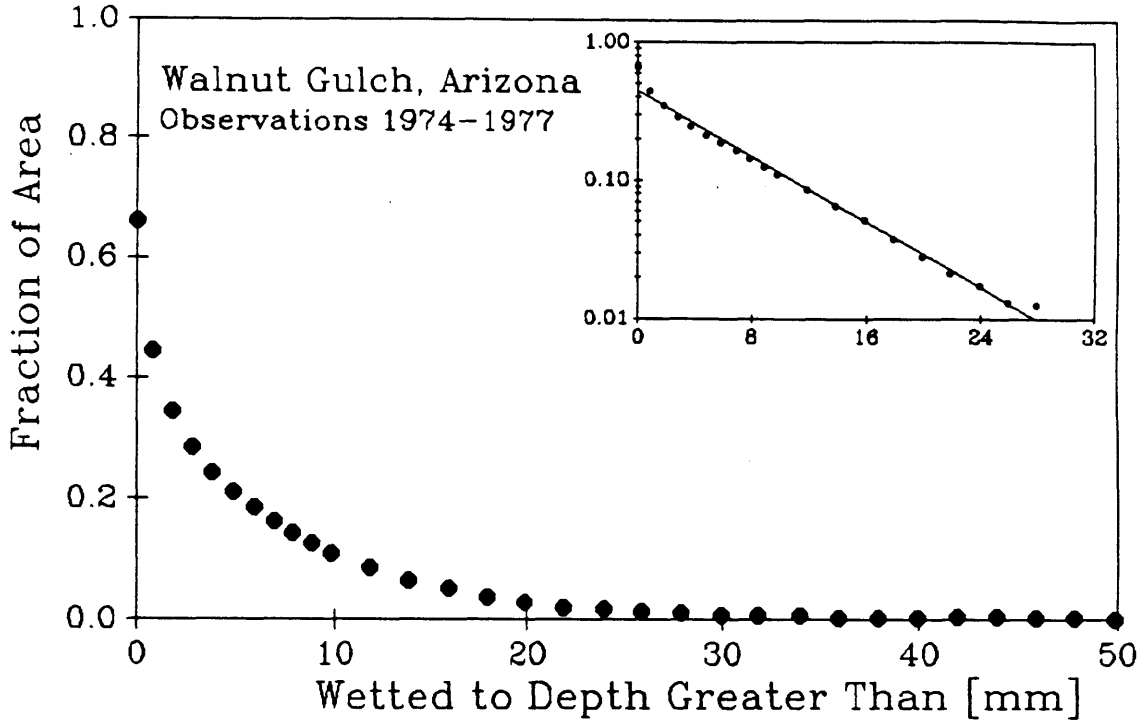

Fig. 2.1 Spatial distribution of total storm depth of airmass thunderstorm rainfall over a basin in Arizona (Adapted from Eagleson et al. 1987). Inset Fig. illustrates a log–linear curve fit to the data

channels, depressions, focal regions of closed drainage basins, zones of overall low soil thickness, high water table, and other impermeable surfaces. Spatial variability of surface soil moisture content also results from lateral moisture redistribution in a sloped drainage network. Areas of lower altitude and close to seepage faces tend to accumulate moisture. In addition, low permeability zones such as those associated with rock outcrops, crusted soils, and increasingly, agricultural and urban areas, are further contributors to runoff generating surfaces.

Observational evidence of the spatial heterogeneity in surface moisture content is documented by Bell et al. (1980) and Owe et al. (1982) for small fields. The magnitude of the coefficient of variation of soil moisture content (which we will call *cv*) increases with the size of the field due to increased heterogeneity of topography and geology at larger scales.

As a first order approximation to the spatial heterogeneity in surface moisture content, we take the point values within the large field to be distributed independent of other factors according to a two–parameter gamma pdf:

$$f_s(s) = \frac{\lambda^{\alpha}}{\Gamma(\alpha)} s^{\alpha-1} e^{-\lambda s} \qquad \lambda,\alpha,s > 0 \qquad (2.2)$$

where s is the surface layer point effective relative soil saturation defined by

$$s = \frac{\theta}{\theta_{sat}} = \frac{\theta}{n} \qquad (2.3)$$

where θ is the active (mobile) volumetric soil moisture content and n is the effective soil porosity. Bulk soil properties such as porosity are highly variable in space and have small correlation scales. For hydrologic processes averaged over the GCM grid scale, however, it is convenient to assume that the soil profile is composed of

homogeneous parallel layers with spatially–averaged hydraulic properties.

At any time step and for every GCM land grid area, the grid mean surface layer relative soil saturation E[s] is known and is propagated in successive GCM integrations as a model prognostic. The parameters of the gamma distribution are related, through the mean E[s], according to

$$\lambda = \alpha \,/\, \mathrm{E[s]} \tag{2.4}$$

The parameter α is related to the cv of gamma distribution as

$$\alpha = cv^{-2} \tag{2.5}$$

Notice that we have not bounded the soil moisture pdf by the physical saturation value s = 1. The mass of the pdf above s = 1 mathematically represents the fraction of the grid area characterized by effective saturation. The dimensionless parameter α of the gamma pdf determines the shape of the distribution. The value $\alpha = 1$ represents the collapse of the gamma pdf to the exponential. With successively higher values of α (smaller cv's), the gamma pdf achieves greater central distribution. With the high cv's characteristic of the point distribution of surface relative soil saturation over large fields, the gamma pdf will possess a notable left skew. This is consistent with the physical situation in which, over entire watersheds, the surface soil moisture is laterally redistributed in a sloped terrain and hence upland areas with the larger fraction of the total watershed area will experience soil saturations below the watershed mean. The relatively smaller areas in and around the drainage network or terrain foci will experience point relative soil saturations above the field mean, including some complete saturation.

d. Surface runoff

For a physically realistic parameterization of surface runoff, both the Horton and Dunne mechanisms of overland flow must be modeled. The two mechanisms of runoff generation may be summarized by:

surface runoff (q) contributors =

Horton mechanism ($P - f^*$ for $P > f^*$ and $s < 1$) +

Dunne mechanism (P for $s \geq 1$), (2.6)

where f^* is the infiltrability of the first soil layer. The first term on the right hand side of (2.6) represents that portion of the point precipitation intensity that exceeds the infiltration rate into the soil. The second term refers to the precipitation that falls directly onto impermeable or saturated (ponded) surfaces. Where the first soil layer is saturated from below, the infiltrability is assumed to be zero. With this condition, and assuming independence of s and P, the general relationship for runoff rate (q) from the entire GCM grid during a time step is

$$\kappa^{-1} q = \int_0^1 \int_{f^*}^{\infty} (P - f^*)\, f_P(P)\, dP\, f_s(s)\, ds + \int_1^{\infty} \int_0^{\infty} P\, f_P(P)\, dP\, f_s(s)\, ds. \quad (2.7)$$

The two terms on the right hand side correspond directly to the respective terms in (2.6).

After substituting (2.1) and (2.2) into (2.7) and integrating we find the dimensionless runoff ratio ($R = q / E[P]$) to be :

$$R = \left[\frac{\alpha}{E[s]}\right]^{\alpha} \frac{1}{\Gamma(\alpha)} \int_0^1 s^{\alpha-1} e^{-\frac{\kappa f^*}{E[P]} - \frac{\alpha s}{E[s]}} ds + 1 - \frac{\gamma(\alpha, \frac{\alpha}{E[s]})}{\Gamma(\alpha)} \qquad (2.8)$$

where $\gamma(\ ,\ )$ is the incomplete gamma function, and $\Gamma(\ )$ is the complete gamma function. The soil infiltrability f^* is dependent on the moisture conditions of the soil, i.e. $f^* = f^*(s)$. With the determination of the functional form of $f^*(s)$, the integration of (2.8) may be completed.

e. Infiltration rates

The general equation of vertical steady flow into unsaturated porous media is

$$q_z = K(s) \left[\frac{d\Psi}{dz} + 1 \right] \qquad (2.9)$$

where $K(s)$ is the unsaturated hydraulic conductivity of the soil at relative soil saturation s and Ψ is the matric potential. The terms inside the bracket represent the gradients of the capillary and gravity forces respectively in the vertical, z, direction. The capillary term dominates when soils are dry. This effect is more pronounced for finer textured soils. Moisture flow in coarse sandy soils, on the other hand, is largely gravitational.

With soil saturation at the very surface due to ponding, the vertical flow into the underlying unsaturated first soil layer is, after (2.9) and for a flat surface,

$$f^* = K(1) \left[\left.\frac{d\Psi}{dz}\right|_{\Psi=\Psi(1)} + 1 \right] \qquad (2.10)$$

where conductivity and capillary effects are evaluated at the interface of saturation. Applying the chain rule to (2.10),

$$f^* = K(1) \left[\left. \frac{d\Psi}{ds} \right|_{s=1} \frac{1 - s}{-\Delta z} + 1 \right] \qquad (2.11)$$

where Δz is the thickness of the top soil layer and $\left(\frac{d\Psi}{ds} \right)$ is the slope of the so–called "moisture–retention curve" for soils. The moisture–retention curves do not have theoretical derivations, and they exhibit hysteresis which complicates their empirical determination. Experimental data on repeated draining and re–saturating of soil columns, however, yield numbers that are fitted with simple curves [see Appendix A, (A.8) to (A.10)].

We may write (2.11) in a more compact manner as

$$f^* = K(1)\, v\, s + K(1)\, (1 - v) \qquad (2.12)$$

where

$$v = \left. \frac{d\Psi}{ds} \right|_{s=1} \frac{1}{\Delta z} \qquad (2.13)$$

The soil thickness Δz is restricted to be comparable to the penetration depth of the infiltration front over the model time–step.

f. The runoff ratio function

Equation (2.8) may be combined with (2.12) to yield a general expression for the runoff ratio under conditions of distributed moisture and precipitation intensity. We define the dimensionless saturated hydraulic conductivity ratio,

$$I = K(1) \,/\, E[P] \qquad (2.14)$$

in order to write the runoff ratio as

$$R = 1 - \frac{\gamma(\alpha, \frac{\alpha}{E[s]})}{\Gamma(\alpha)} + \frac{e^{-\kappa I(1-v)} \quad \gamma(\alpha, \kappa I v + \frac{\alpha}{E[s]})}{(\frac{\kappa I v E[s]}{\alpha} + 1)^{\alpha} \quad \Gamma(\alpha)} \tag{2.15}$$

This is the result of convolving the two independent distributions of soil moisture and precipitation with a kernel that represents the physical equation of moisture infiltration into partially saturated soils. The expression further depends on the soils' capillary properties under conditions of less–than–full saturation.

To perform diagnostic studies of this runoff relationship, we take the simple case of gravitational flow only [$v \to 0$ in (2.12)] in which case

$$f^* \simeq K(1) \tag{2.16}$$

and (2.15) becomes

$$R = \left[1 - \frac{\gamma(\alpha, \frac{\alpha}{E[s]})}{\Gamma(\alpha)} \right] + \left[\frac{\gamma(\alpha, \frac{\alpha}{E[s]})}{\Gamma(\alpha)} \right] e^{-\kappa I} \tag{2.17}$$

The interpretation is now simple. A saturated fraction $\left[1 - \frac{\gamma(\alpha, \frac{\alpha}{E[s]})}{\Gamma(\alpha)} \right]$, representing the integral of the probability density function $f_s(s)$ above 1, has runoff ratio unity. Over this saturated fraction, all precipitation is runoff. The remaining or unsaturated fraction, $\left[\frac{\gamma(\alpha, \frac{\alpha}{E[s]})}{\Gamma(\alpha)} \right]$ has runoff ratio $e^{-\kappa I}$. As the wetted fraction κ becomes smaller, as the precipitation becomes more intense, or the saturated hydraulic conductivity becomes smaller, then the

unsaturated fraction will have a higher runoff ratio. On the other hand, as ratio I grows, that is as soils become exceedingly permeable, the contribution to the runoff ratio from the unsaturated fraction diminishes.

In either (2.15) or (2.17), the Dunne runoff $\left[1 - \frac{\gamma(\alpha, \frac{\alpha}{E[s]})}{\Gamma(\alpha)} \right]$ is the lower limit to the runoff ratio. Any contribution to the runoff ratio in excess of this lower limit is due to interactions of the precipitation intensity and the soil's moisture condition, i.e. Horton runoff.

g. The relative role of runoff types

The non–vanishing lower limit to the runoff ratio for moist soils is a distinct improvement over current parameterizations. For most soils and typical GCM grid precipitation intensities, the ratio I is expectedly large. Under non–distributed conditions, with the hydraulic conductivity of soils larger than the precipitation intensity, runoff is unlikely. With the assumed distributions and the physically realistic equations of moisture flow, however, significant runoff is possible even for large I.

We begin analyzing the behavior of the runoff ratio by assuming a fixed value of unity for the *cv* associated with the point distribution of the first soil layer relative saturation. Figure 2.2 shows the runoff ratio as a function of the GCM grid mean relative saturation for negligible soil capillarity, for $\alpha = 1$, and for the 60% fractional wetting which is consistent with observations for mesoscale rainfall (Eagleson 1984; Eagleson et al. 1987). The multiple curves correspond to various values of the ratio I which in this example represents moisture flow under gravity only. The lower the excess of saturated hydraulic conductivity with respect to precipitation (i.e. the lower I), the greater the possible runoff. At the other extreme, however, as the soil becomes more and more conductive (i.e. greater I),

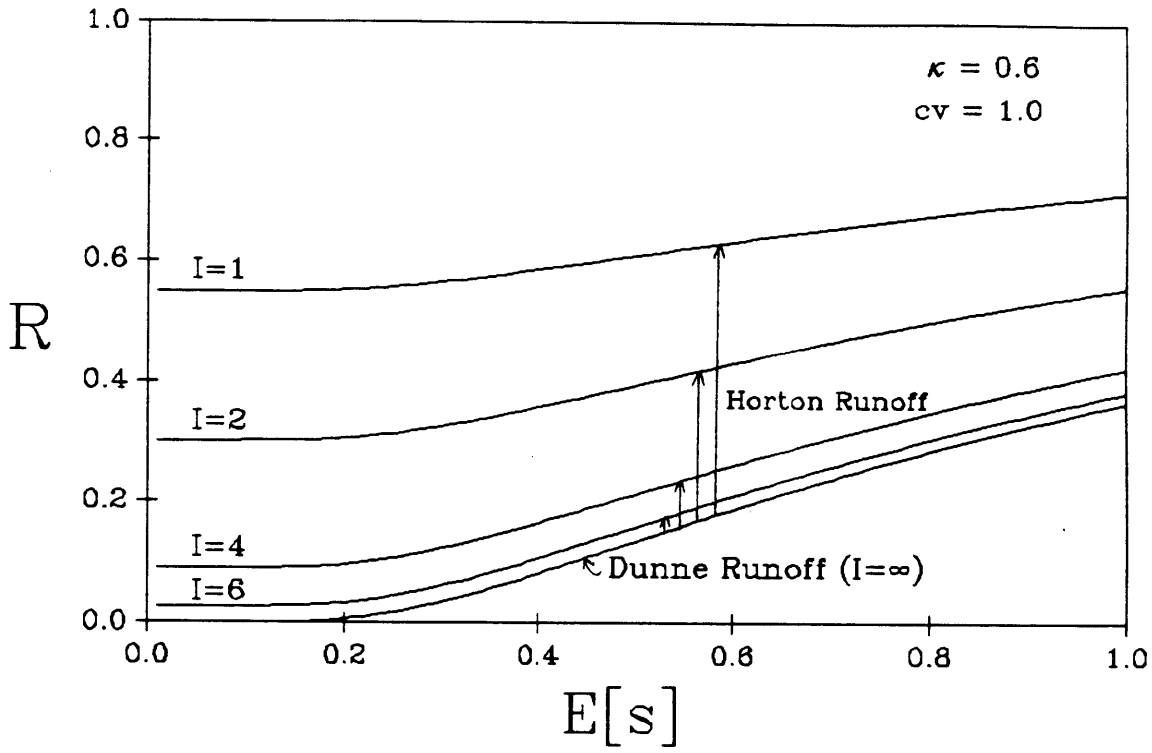

Fig. 2.2 Surface runoff ratio function for negligible soil capillarity, $\kappa = 0.6$, and $cv = 1$

the runoff rates reduce but conveniently never vanish when the soil is relatively moist. This is due to the presence of a fraction of saturated surfaces within the basin.

Figure 2.3 also represents gravity–only infiltration, but here the ratio I is fixed at a lower value I = 2 and the wetted fraction κ is varied from 20% to 80%. The excess of runoff above the partial area–type lower limit may again be attributed to surface flow via the Horton mechanism. The smaller the wetted region, the higher is the precipitation intensity and thus the higher the Horton runoff rate.

Clearly the $\left[1 - \frac{\gamma(\alpha, \frac{\alpha}{E[s]})}{\Gamma(\alpha)} \right]$ lower limit to all runoff under any precipitation, soil moisture, soil type, and fractional wetting conditions refers to partial area–type (i.e. Dunne mechanism) surface runoff. Any runoff generated above this rate may be attributed to the Horton mechanism and is critically dependent on precipitation intensity. The existence of a distributed precipitation intensity field is thus an effective method of inducing surface runoff by the Horton mechanism as has been shown in another way by Milly and Eagleson (1988). However this does not necessarily imply relative importance of the Horton mechanism as can be seen when typical soil properties are considered as in Fig. 2.4.

Figure 2.4a compares the runoff ratios for sandy loam soil (75% sand, 20% silt, and 5% clay) with [Eq. (2.15)] and without [Eq. (2.17)] the capillary effect and including the I = ∞ limit. For such soils the saturated hydraulic conductivity can be as high as tens and even hundreds of millimeters per hour; thus with typical precipitation intensities, the ratio I will be quite large. Notice for I= 15, the runoff ratio lies at the partial area–type lower limit. Therefore, for permeable soils, even with distributed precipitation intensities, the Horton mechanism is a minor contributor to total surface flow when compared with the Dunne mechanism.

For the heavier clay loam soil (30% sand, 35% silt, and 35% clay) the

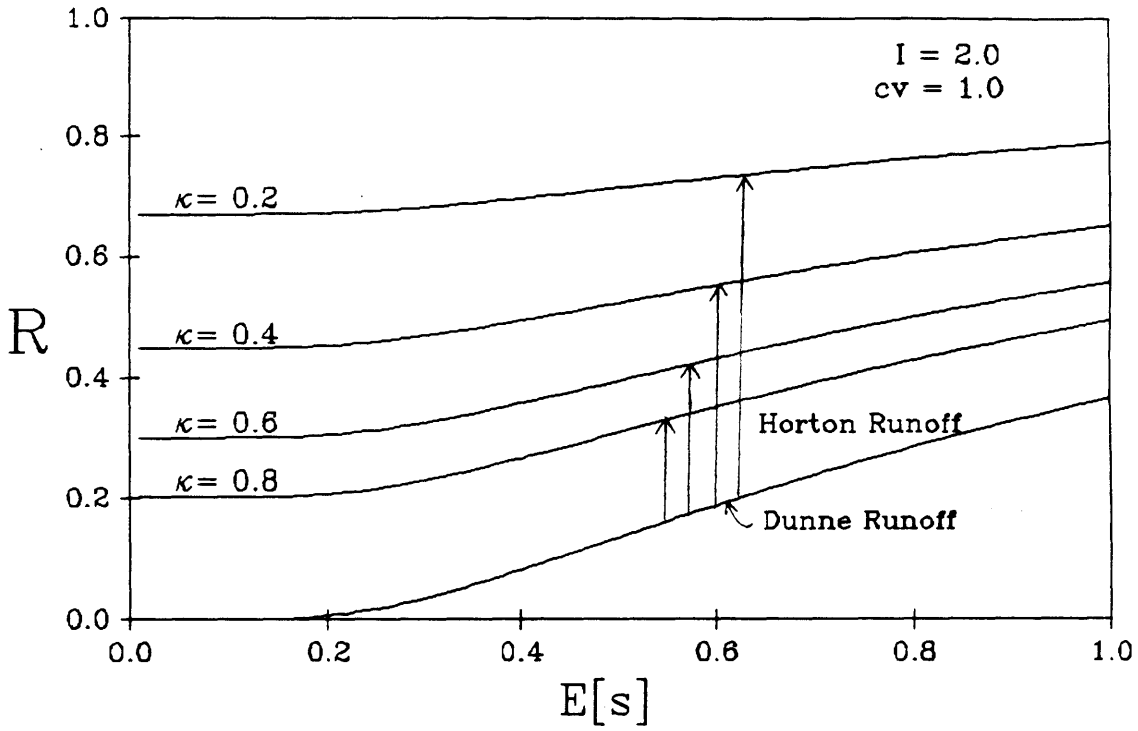

Fig. 2.3 Surface runoff ratio function for negligible soil capillarity, I = 2, and $cv = 1$

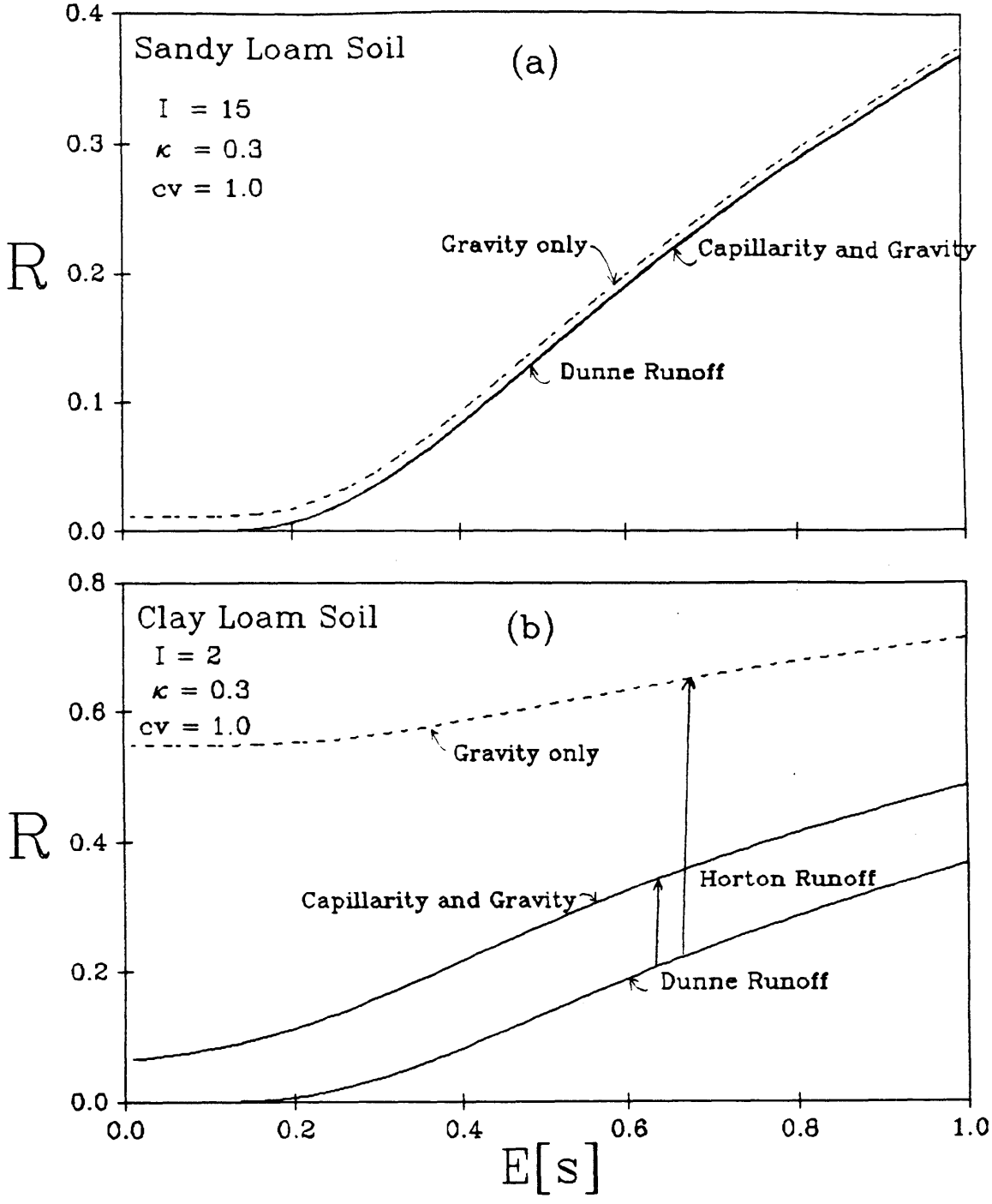

Fig. 2.4 Surface runoff ratio function with and without soil capillarity, $\kappa = 0.3$, $cv = 1$, depth of first soil layer = 0.1 m. (a) Sandy loam soil (75% sand, 20% silt, and 5% clay), and (b) clay loam soil (30% sand, 35% silt, and 35% clay)

saturated hydraulic conductivity can be as low as a few millimeters per hour, and the ratio I may turn out to be as low as I = 2. For these soils the capillary effect is significant as can be seen in Fig. 2.4b which is plotted at half the vertical scale of Fig. 2.4a. For gravity only infiltration (Fig. 2.2) small I leads to large Horton runoff, but when capillarity is considered (Fig. 2.4b) even with small I, the Horton runoff is sharply reduced.

In summary, we see that for $\alpha = 1$ and over the normal range of saturated soil permeabilities, runoff is predominantly of the partial–area type except for clay soils where the Horton mechanism can play a significant role. This soil moisture parameterization is shown to be an improvement over those in current use in that it generates surface runoff when realistic values of soil conductivity and precipitation intensity are encountered. The distributed precipitation intensities over a fraction κ of the grid are shown to be important in allowing the possibility of surface runoff by the Horton mechanism.

h. Effect of spatial variability on the runoff ratio

Figure 2.5 illustrates the effect of the soil moisture distribution shape on the runoff ratio. In this figure $\kappa = 0.3$ and, for economy of presentation, only the $I = \infty$ case is considered. The shape of the soil moisture distribution is varied through changes in α (and therefore in the coefficient of variation of the underlying gamma distribution). The curves reflect the fraction of the GCM grid area that is saturated. This is equivalent to the probability mass concentrated above s = 1 for the particular gamma pdf. With $cv < 1$ and at lower mean soil saturations (E[s] << 1), a lesser amount of the gamma pdf mass falls above s = 1 when compared to distributions with higher cv and the same E[s]. In the limit $cv = 0$ the soil moisture is uniform everywhere and there will be runoff in the $I = \infty$ case only with E[s] = 1 at which point R = 1. Furthermore, unsaturated soils with $cv = 0$ experience no

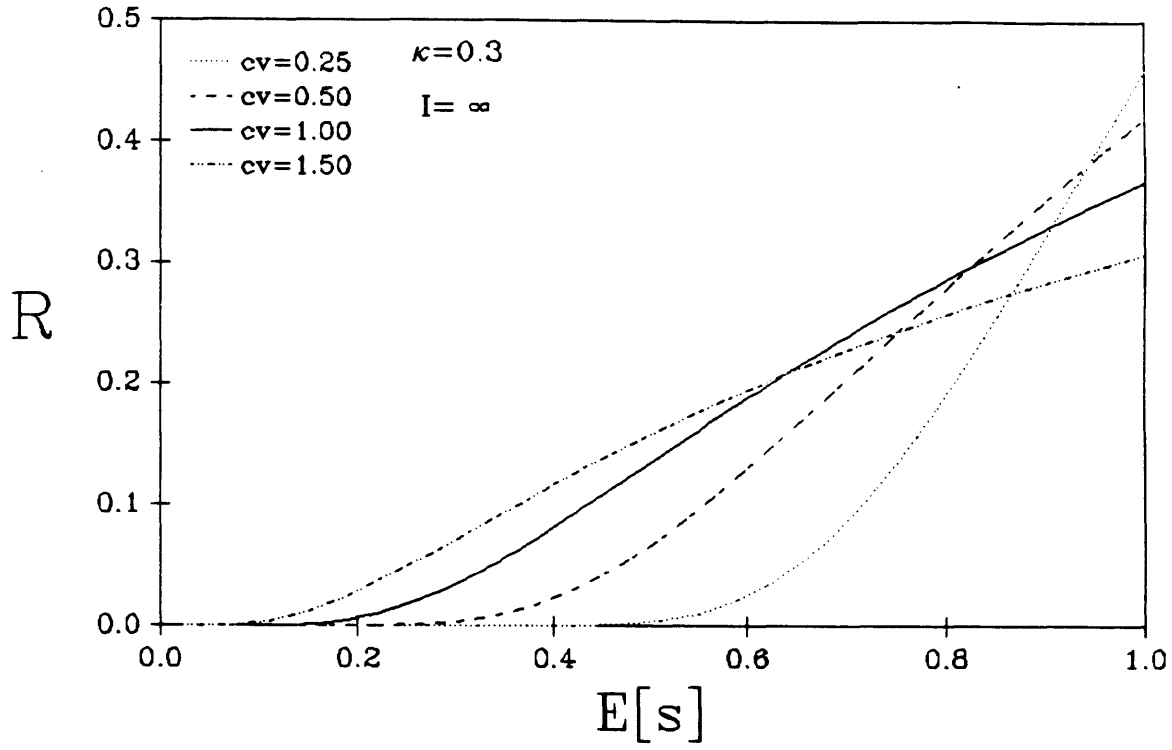

Fig. 2.5 The effect spatial variability of soil moisture on the runoff ratio function with $\kappa = 0.3$, and $I = \infty$

surface runoff if $I \leq 1$ and the duration of the storm event is short.

3. *Soil moisture losses due to evapotranspiration*

Evapotranspiration is conveniently normalized by its limiting value, the atmospheric vapor transport capacity (i.e. potential evapotranspiration) e_p to obtain what is known as the evapotranspiration efficiency. This efficiency is currently parameterized as an empirical function of soil moisture in most GCMs (e.g. Sud and Fennessy 1982). In this section, a derived distribution of the evapotranspiration efficiency is obtained utilizing the basic soil moisture physics and an assumed heterogeneity of the process.

a. Subgrid heterogeneity of soil hydraulic conditions

Following the satisfaction of the canopy surface retention and surface runoff requirements, the residual precipitation depth is added to storage in the soil. Removal of the accumulation on the canopy and in the soil is then forced by the atmospheric evaporative demand. When the canopy surface is clear of retention depth, the plant may transpire and thereby remove soil moisture from the rooted soil layers.

Both bare soil evaporation and root soil moisture extraction processes are strongly dependent on the hydraulic state of the soil. The hydraulic state is in turn a function of soil type and saturation level. In Section 2c, the soil moisture content of the first soil layer is assumed to be spatially distributed over the GCM grid [Eq. (2.2)]. There, the tail of the pdf above the soil saturation value represents the fraction of the GCM grid area that is characterized by soil saturation. In the evapotranspiration parameterization, a similar distribution is assumed for the relative saturation of the first soil layer.

b. Evaporation from bare soils

Under steady atmospheric forcing the loss of moisture from soil storage may cause a shift in the control of the evaporation rate from bare soils. When wet, a given soil may be capable of delivering moisture from soil storage to the surface at a rate equal to or greater than the atmospheric vapor transport capacity. Such cases are termed "climate–controlled" or "energy–limited" (Eagleson 1978c) as the actual evaporation rate will equal the climate–determined potential rate.

Continuing depletion of the stored soil moisture decreases the rate at which the soil can deliver moisture to the surface. At some moisture state, assuming constant climatic conditions, the rate of soil moisture delivery falls below the potential evaporation rate. At this and lower moisture states, the evaporation rate is then termed "soil–controlled" or "water–limited" (Eagleson 1978c) and is a nonlinear function of the moisture content due to its dependence on the soil water diffusivity. The relative soil saturation s* at which the limits to evaporation shift is a function of the potential evaporation rate and of the soil properties.

c. Soil moisture desorption processes

In parameterizing the bare soil evaporation, we begin with the basic partial differential equation describing vertical moisture diffusion and moisture mass conservation in porous media,

$$\frac{\partial \theta}{\partial t} = \frac{\partial}{\partial z}\left[D(\theta) \frac{\partial \theta}{\partial z} \right] + \frac{\partial K}{\partial z} \qquad (2.18)$$

where $D(\theta)$ is the soil water diffusivity and is defined by

$$D(\theta) = K(s) \frac{\partial \Psi}{\partial \theta} \qquad (2.19)$$

The initial and boundary conditions are taken as

$$\begin{aligned} s\,(z,0) &= \theta_0/\theta_{sat} = s_0 \\ & \qquad\qquad z,t \geq 0 \\ s\,(0,t) &= \theta_1/\theta_{sat} = s_1 \end{aligned} \tag{2.20}$$

That is, a uniform moisture content s_0 characterizes the entire affected profile at time zero but a steady s_1 condition holds at the plane z=0.

Philip (1957b) provides an approximate solution to (2.18) subject to (2.20) in which the desorption rate is proportional to $t^{-1/2}$. The constant of proportionality is referred to as the sorptivity S_e. The exfiltration rate under the combined influence of gravity and capillarity is given by

$$f_e = \frac{1}{2} S_e\, t^{-1/2} - \frac{[K(s_0)+K(s_1)]}{2} \tag{2.21}$$

and with $s_1 << s_0$,

$$f_e \approx \frac{1}{2} S_e\, t^{-1/2} - \frac{1}{2} K(s_0) \tag{2.22}$$

This equation represents the rate at which a uniformly wetted, semi–infinite porous medium loses moisture to vertical (upward) desorption. The drying of the uniformly wetted profile proceeds at a rate inversely proportional to the square–root of time. Time scales associated with the substantial drying of soils are, however, generally larger than those used in integrating climate simulation models. This allows the time–averaging of the desorption rate over the GCM time step. At the end of each time step, the diagnostic variables such as the soil layer moisture contents are updated and restricted to uniform distribution. At the beginning of the

next time step, therefore, the desorption rate acts on an updated s_0 and $t = 0$ will again govern. The depth of the discretized (top) soil layer must be larger than the depth of moisture extraction during the time step in order for the semi–infinite initial condition to be valid.

The time–average desorption rate over the integration time T (GCM time step, e.g. one–hour) is

$$\overline{f}_e = \frac{1}{T} \int_0^T f_e(t)\, dt$$

$$= S_e T^{-1/2} - \frac{1}{2} K(s_0) \qquad (2.23)$$

The functional form of the desorptivity function S_e is derived in Appendix A.

d. Bare soil evaporation under soil–controlled conditions

The time–averaged desorption rate is a function of the moisture content and of the unsaturated hydraulic conductivity. The rate of vertical moisture desorption from the top soil layer may be defined by combining (A.9), (A.14), and (2.23) into

$$\overline{f}_e = K(1)\, \Omega\, s_0^{\frac{1}{2m} + 2} - \delta \frac{1}{2} K(1)\, s_0^{\frac{2}{m} + 3} . \qquad (2.24)$$

where Ω is a dimensionless soil parameter defined as

$$\Omega = \left[\frac{8\ n\ \Psi(1)}{3\ K(1)\ T\ (1+3m)(1+4m)} \right]^{1/2} \qquad (2.25)$$

The variable δ is a toggle which is either zero or one depending on whether the

gravity term is to be excluded or included. Equation (2.24) is the time–averaged flux rate dependent on the initial relative soil saturation s_0 of the surface layer.

e. Derived distribution of bare soil evaporation efficiency

The evaporation rate is given by (2.24) whenever $\bar{f}_e$ is less than the potential evaporation rate e_p. Otherwise e_p is the governing loss rate. We let the relative soil saturation of the upper soil layer have the value s* at the transition of evaporation rate control (i.e. $\bar{f}_e\big|_{s=s^*} = e_p$) , i.e.

$$\begin{aligned} s \geq s^* &\quad \text{climate–controlled evaporation} \\ s < s^* &\quad \text{soil–controlled evaporation} \end{aligned} \tag{2.26}$$

We combine these definitions and the spatial distribution of soil hydraulic states to write the spatial average bare soil evaporation from the GCM grid area as

$$E[\bar{f}_e] = e_P \int_{s^*}^{\infty} f_s(s)\, ds + \int_0^{s^*} \bar{f}_e\, f_s(s)\, ds \tag{2.27}$$

1. Gravity–neglected case

Beginning with the simpler case that neglects the gravity term ($\delta = 0$), the substitution of (2.24) into (2.27) results in

$$\beta_s = 1 - \frac{\gamma(\alpha, \frac{\alpha\, s^*}{E[s]})}{\Gamma(\alpha)} + \frac{K(1)}{e_P}\,\Omega\,\left(\frac{E[s]}{\alpha}\right)^{\frac{1}{2m}} + 2\left[\frac{\gamma(\frac{1}{2m}+2+\alpha, \frac{\alpha\, s^*}{E[s]})}{\Gamma(\alpha)}\right] \tag{2.28}$$

From the definition of s* (soil saturation at which $\bar{f}_e = e_p$) for gravity neglected case ($\delta = 0$),

$$e_p = K(1)\ \Omega\ s^{*\,\frac{1}{2m}} + 2 \tag{2.29}$$

Rewrite (2.29) as

$$\frac{K(1)}{e_p} = \left[\ \Omega\ s^{*\,\frac{1}{2m}} + 2\ \right]^{-1} \tag{2.30}$$

and eliminate $\frac{K(1)}{e_p}$ between (2.28) and (2.30) to write the bare soil evaporation efficiency as

$$\beta_s = 1 - \frac{\gamma(\alpha, \alpha\mathscr{E}^{-1})}{\Gamma(\alpha)} + (\alpha\mathscr{E}^{-1})^{-\frac{1}{2m}} - 2\left[\frac{\gamma(\frac{1}{2m}+2+\alpha, \alpha\mathscr{E}^{-1})}{\Gamma(\alpha)}\right] \tag{2.28}$$

where the dimensionless parameter $\mathscr{E}$ is simply

$$\mathscr{E} = E[s] / s^* . \tag{2.29}$$

Combining (2.29) and (2.32) yields

$$\mathscr{E} = E[s]\left[\frac{K(1)\ \Omega}{e_p}\right]^{\frac{2m}{1+4m}} . \tag{2.33}$$

As with the case of runoff, we first assume $cv = 1$ (i.e. exponential pdf) in

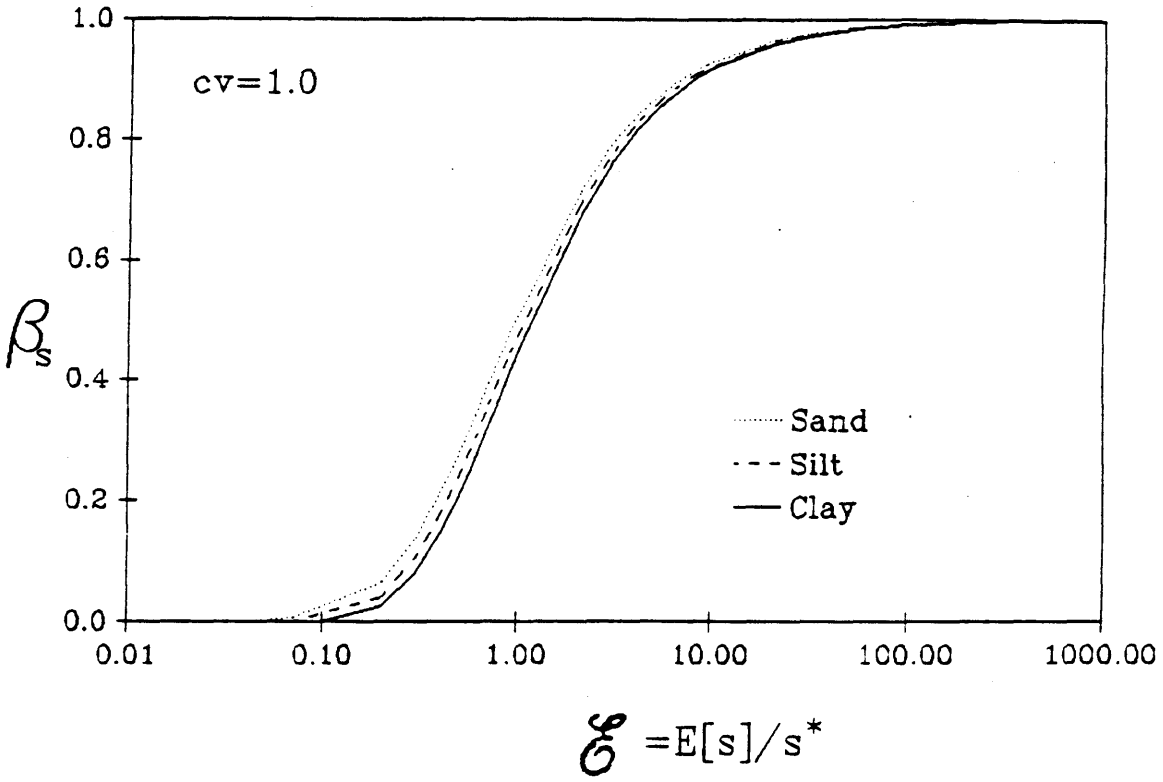

Fig. 2.6 Bare soil evaporation efficiency, $cv = 1$, and gravity neglected

order to study the behavior of the evaporation efficiency function with respect to the soil type and climate variables.

The bare soil evaporation efficiency (gravity–neglected) is plotted in Fig. 2.6 for various soil types. From the definition of δ we see that the evaporation efficiency is significantly increased as s* decreases, and the climate, rather than the soil, becomes the controlling factor in determining the moisture loss from soil storage. We also note that other than through δ, the bare soil evaporation efficiency is only weakly dependent on soil type. The ratio δ itself is strongly dependent on soil type even when similar atmospheric evaporative demands are imposed (Fig. 2.7).

2. Gravity–included case

When the soil is rather moist and/or the soil is characterized by a high hydraulic conductivity, the gravity term may be a significant fraction of the desorption term. Under these circumstances, we take the full form of (2.24) with $\delta = 1$ and substitute it into (2.27) to derive the gravity–included bare soil evaporation efficiency,

$$\beta_s = 1 - \frac{\gamma(\alpha, \alpha\delta^{-1})}{\Gamma(\alpha)} + \tag{2.34}$$

$$\frac{K(1)}{e_p} \frac{\Omega(\alpha^{-1}\delta)^{\frac{1}{2m}+2}\gamma(\frac{1}{2m}+2+\alpha, \alpha\delta^{-1}) - \frac{1}{2}(\alpha^{-1}\delta)^{\frac{1}{2m}+3}\gamma(\frac{1}{2m}+3+\alpha, \alpha\delta^{-1})}{\Gamma(\alpha)}$$

Again the transitional relative soil saturation s* is defined through equating e_p and $\overline{f}_e$, i.e.,

$$e_p = K(1)\,\Omega\, s^{*\,\frac{1}{2m}+2} - \frac{1}{2} K(1)\, s^{*\,\frac{2}{m}+3}. \tag{2.35}$$

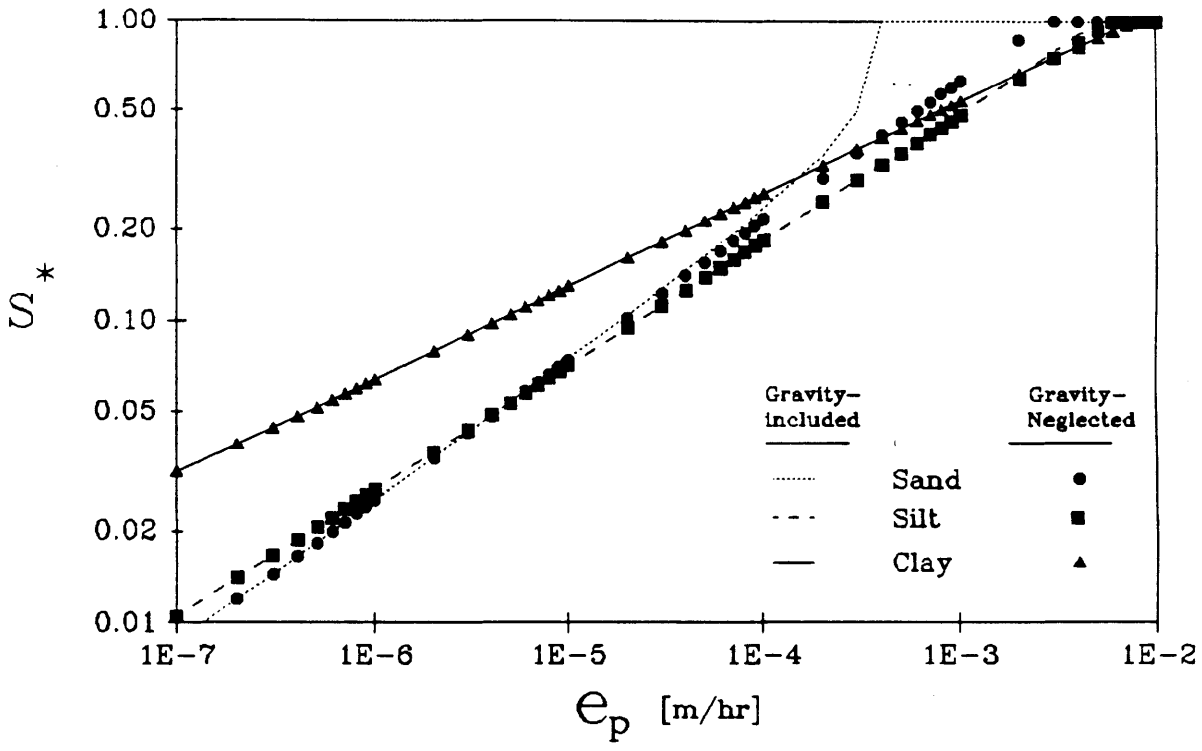

Fig. 2.7 The effect of gravity on the transitional relative soil saturation s* as a function of the potential evaporation rate

Eliminate $\frac{K(1)}{e_p}$ between (2.34) and (2.35) and write

$$\beta_s = \frac{\left[\Omega' \quad \gamma(\frac{1}{2m}+2+\alpha,\alpha\delta^{-1}) - \frac{1}{2} \quad \gamma(\frac{2}{m}+3+\alpha,\alpha\delta^{-1}) \right]}{\left[\Omega'(\alpha\delta^{-1})^{\frac{1}{2m}+2} \quad -\frac{1}{2}(\alpha\delta^{-1})^{\frac{2}{m}+3}\right]\Gamma(\alpha)}$$

$$+ 1 - \frac{\gamma(\alpha, \alpha\delta^{-1})}{\Gamma(\alpha)} \tag{2.36}$$

where

$$\Omega' = \Omega \left[\frac{\alpha}{E[s]} \right]^{\frac{3}{2m}+1}. \tag{2.37}$$

3. *Relative importance of gravity*

Figure 7 illustrates values for the transitional soil relative saturation s* under a variety of soil and climatic conditions. The gravity–inclusive and –neglected Eqs. (2.29) and (2.35) are used to define s*. In inspecting Fig. 2.7, we notice that over a wide range of soil and potential evaporation conditions, the gravity term does not significantly affect the resultant values of s*. Thus the parameter δ may be approximated as equivalent for both physical situations, in which case a rather simple expression may be presented relating bare soil evaporation efficiencies with and without the gravity term. Defining the dimensionless term

$$\Lambda = \frac{2\ \Omega' \quad - \quad \dfrac{\gamma(\frac{2}{m}+3+\alpha,\alpha\delta^{-1})}{\gamma(\frac{1}{2m}+2+\alpha,\alpha\delta^{-1})}}{2\ \Omega' \quad - \quad (\alpha\delta^{-1})^{\frac{3}{2m}+1}} \tag{2.38}$$

allows us to write

$$\left[\beta_s\right]_{\substack{\text{gravity-}\\\text{included}}} = \Lambda \left[\beta_s\right]_{\substack{\text{gravity-}\\\text{neglected}}} + (1-\Lambda)\left[1 - \frac{\gamma(\alpha, \alpha\delta^{-1})}{\Gamma(\alpha)}\right] \qquad (2.39)$$

The parameter Λ represents the factor by which the water–limited evaporation efficiency is reduced due to the incorporation of gravity in the vertical soil moisture exfiltration formulation. Because gravity acts only to retard exfiltration out of the soil column, then $0 \leq \Lambda \leq 1$. With soil moisture subgrid spatial variablility, a fraction $\left[1 - \frac{\gamma(\alpha, \alpha\delta^{-1})}{\Gamma(\alpha)}\right]$ will have $s \geq s^*$ where the bare soil evaporation will be climate–controlled and independent of gravity. Reduction of the evaporation efficiency over both the water–limited and climate controlled regimes by Λ is the cause for the appearance of the compensating term $(1-\Lambda)\left[1 - \frac{\gamma(\alpha, \alpha\delta^{-1})}{\Gamma(\alpha)}\right]$ on the right–handside of (2.39).

In Fig. 2.8 the linear *gravity–effect* term Λ is plotted for various soil and climatic conditions. As Λ approaches unity, the gravity term diminishes in significance when compared to the desorptive term [Eq. (2.39)]. The gravity term is less important for fine–textured soils and thus the values of Λ are practically equal to unity for silt and clay under all conditions. Only sandy soils wetted to near saturation exhibit slight reduction (mostly < 20%) in evaporation efficiency due to the inclusion of the gravity term. When transitional relative soil saturation s^* is low, the bare soil evaporation over much of the GCM grid is climate–controlled. In this case and irrespective of soil type, the gravity term does not contribute significantly to the GCM grid evaporation efficiency.

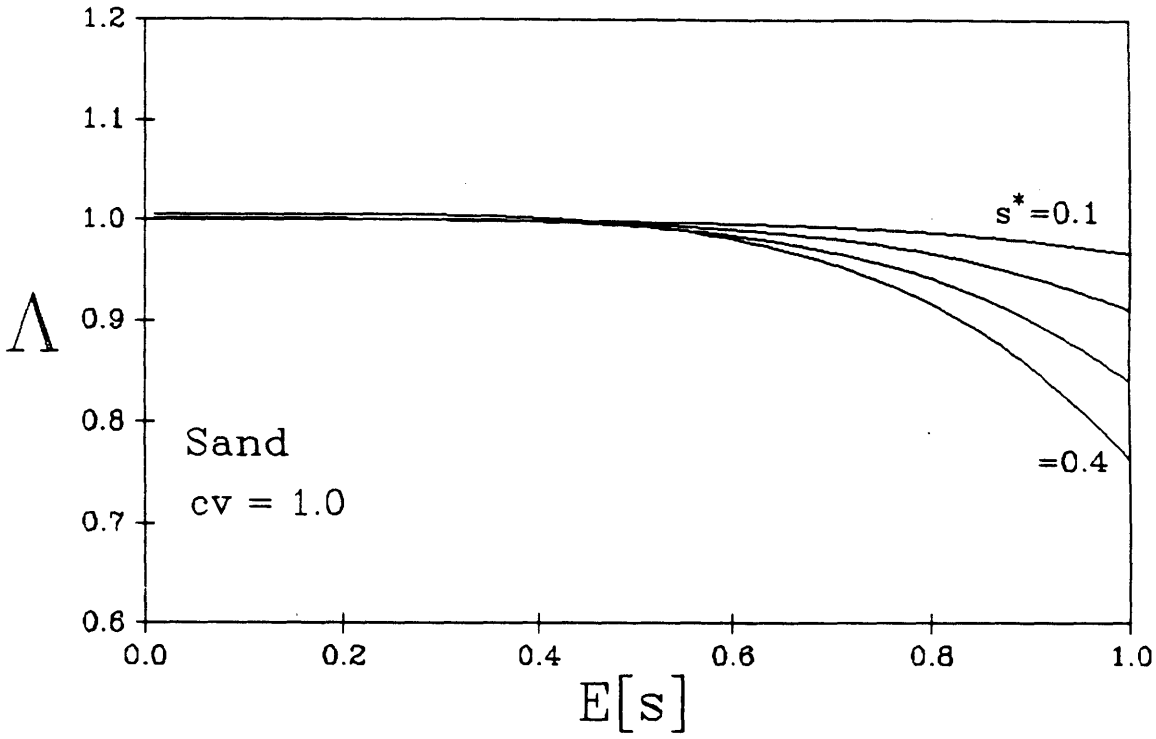

Fig. 2.8 Reduction in bare soil evaporation efficiency due to the inclusion of gravity

f. Soil–water extraction by plant roots

Over the vegetated fraction of the GCM grid landsurface, the plant roots are active in releasing soil moisture into the atmosphere through transpiration. Transpiration is only possible when the canopy–intercepted moisture has evaporated.

The process of moisture extraction by roots escapes simple treatment. Molz (1981) catalogues various common approaches to bulk parameterization. Among the models that incorporate atmospheric, soil, and vegetation factors, the approach of Feddes et al. (1978) [also cited in Molz (1981)] is parsimonious and nontrivial. In this parameterization, for any single layer, the soil moisture extraction function $e_v(s)$ by roots is

$$e_v(s) = \begin{cases} 0 & 0 \le s \le s_w \\ e_P \dfrac{s - s_w}{s^* - s_w} & s_w < s < s^* \\ e_p & s^* \le s < 1 \\ 0 & \text{saturated} \end{cases} \qquad (2.40)$$

where s_w is the relative soil moisture state below which the plant shuts its stomata and eventually wilts and s^* is that above which the transpiration by plants is limited by the evaporative demand of the atmosphere. We arbitrarily take this latter transition point above which transpiration is climate–controlled and below which transpiration is stomatal and soil–controlled, to be identical to that defined for bare soil evaporation. The gravity–neglected desorption is used. This is obviously only a practical approximation of a process which would otherwise require detailed consideration of microphysical processes in and around plant membranes embedded in porous media. For intermittently flooded regions where our unlimited soil moisture variable takes on the analytical state $s > 1$, the loss of soil moisture to

the atmosphere by terrestrial plant root extraction ceases. However direct evaporation at the potential rate from the canopy and surface is possible and will occur at the potential rate. For simplicity we also assume that the aquatic vegetation of perennial wetlands transpire at the potential rate e_p . Thus over the vegetated fraction of the GCM grid land surface area, a statement of moisture loss by evapotranspiration will effectively include the plant root extraction relations of (2.40) with the provision of potential evaporation rates for all $s > s^*$.

The second transition point in the soil relative saturation is the wilting level s_w. Both soil and vegetation characteristics contribute to the definition of this point. For various vegetation types, the wilting matric potential is generally assumed known and constant. This level is translated into s_w by accounting for the soil hydraulic characteristics. Working with (A.8), s_w is defined as

$$s_w = \left[\frac{\Psi_{wilt}}{\Psi(1)} \right]^{-m} \tag{2.41}$$

In the following derivations of a transpiration efficiency function, we assume independent distributed conditions for the topmost soil layer only. The remaining soil layers will have parameterizations that are discussed in Chapter III.

Using the gamma distribution of soil moisture in the first soil layer, the spatial average transpiration over the vegetated fraction is

$$E[e_v] = \int_{s_w}^{s^*} e_v(s)\, f_s(s)\, ds + e_p \int_{s^*}^{\infty} f_s(s)\, ds \tag{2.42}$$

Substituting (2.33) and (2.40) into (2.42) and integrating we have the spatial average transpiration efficiency

$$\beta_v = \frac{E[e_v(s)]}{e_p} = \tag{2.43}$$

$$1 + \frac{\gamma(\alpha+1,\alpha\mathscr{E}^{-1}) - \alpha\mathscr{E}^{-1}\,\gamma(\alpha,\alpha\mathscr{E}^{-1}) - \gamma(\alpha+1,\alpha\mathscr{W}^{-1}) + \alpha\mathscr{W}^{-1}\gamma(\alpha,\alpha\mathscr{W}^{-1})}{\Gamma(\alpha)\quad(\alpha\mathscr{E}^{-1} - \alpha\mathscr{W}^{-1})}$$

where

$$\mathscr{W} = E[s] \,/\, s_w \qquad . \tag{2.44}$$

This equation represents the reduction of transpiration below the potential value due to soil and vegetation factors under conditions of independently distributed soil moisture over the GCM grid area. Above relative saturation equal to the combined soil–atmosphere parameter s*, transpiration proceeds at its potential rate. Below the wilting level s_w, the root extraction of moisture (and hence transpiration) is identically zero. And for relative soil saturations between s_w and s*, the transpiration efficiency rises linearly from zero to unity. Unlike the bare soil case, the lower bound to s* is s_w. The upper bound is unity. In fact, when $s^* \to s_w$ ($\mathscr{E} \to \mathscr{W}$) or $s_w \geq s^*$ ($\mathscr{W} \leq \mathscr{E}$), β_v reaches a limit that is only visible after applying L'Hôpital's rule to (2.43):

$$\underset{s^* \to s_w}{Limit}\quad \beta_v = 1 - \frac{\gamma(\alpha, \alpha\mathscr{W}^{-1})}{\Gamma(\alpha)} \,. \tag{2.45}$$

In this special case (herbaceous crops and short grasses, for example) the transpiration efficiency is unity for the fraction of the grid area that has soil relative saturation above wilting under the defined spatial distribution.

In Fig. 2.9 β_v is plotted against the parameter $\mathscr{E}$ for the two limits $s_w = 0$ and

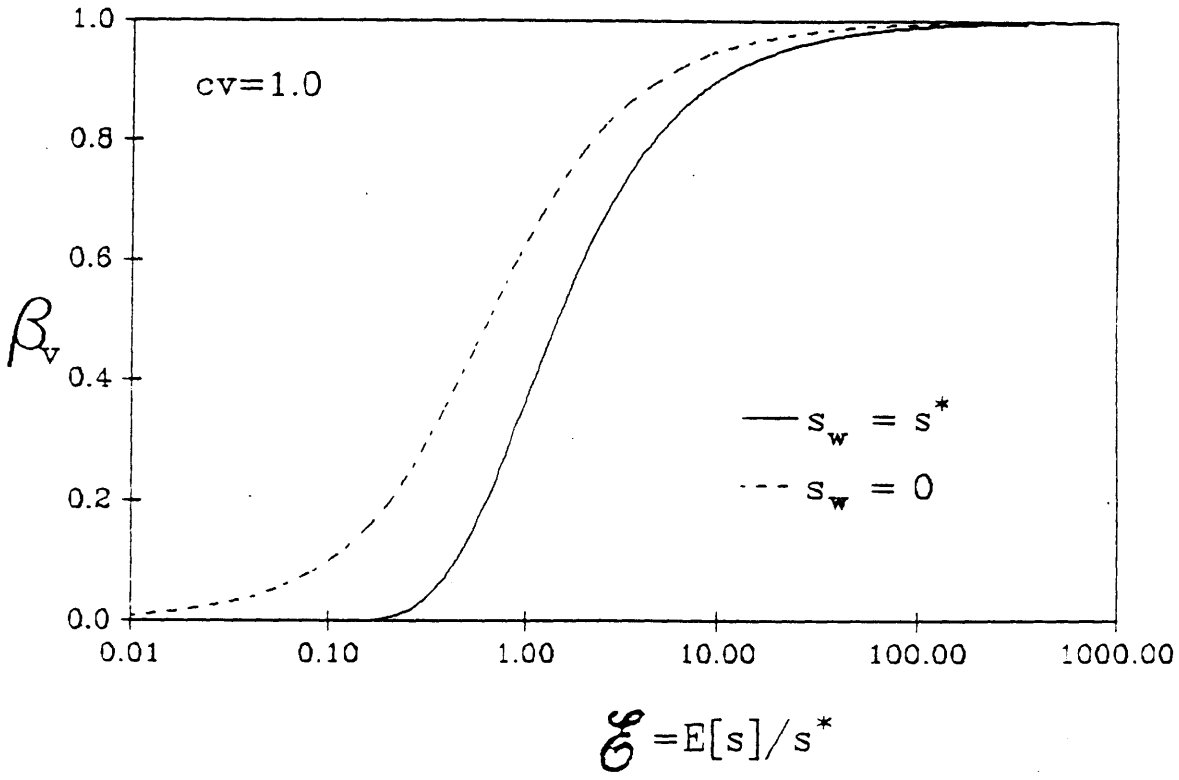

Fig. 2.9 Transpiration efficiency with $cv = 1$

$s_w = s^*$ with $\alpha = 1$. In sandy soils, setting $s_w = 0$ would be reasonable since, over the typical range of values for Ψ_{wilt}, the relative soil saturation at the wilting point generally stays close to zero. In heavier soils, however, strong matric potentials are present even with high relative saturations. There, s_w may be the limit to s^* and thus (2.45) the limit to (2.43).

g. Effect of spatial variability of soil moisture on the bare soil evaporation and the transpiration efficiencies

In Figs. 2.10 and 2.11, β_s and β_v are plotted against $\delta = E[s] / s^*$ for $m = 1$ and *cv* values 0.25, 0.5, 1.0, and 1.5. Also plotted are the curves for the $cv = 0$ limit in which case the soil moisture is uniform everywhere over the GCM grid area. In the vicinity of $\delta = 1$, we see that β is sensitive to *cv*. Again lower *cv*'s imply greater central distribution and less variance about the mean for the gamma pdf of the surface moisture conditions. With higher *cv*'s, the probability mass of the gamma pdf has greater dispersion about its mean $E[s] / \alpha$.

For $\delta >> 1$, β's are large because the average soil moisture condition exceeds that for which the climate controls the evaporation or transpiration. Under this condition increasing *cv* means more of the soil will be under soil control and hence the values of the β's decline.

For $\delta << 1$ on the other hand, the average soil moisture condition is less than that for which the climate controls the evaporation. Under this condition increasing *cv* means more of the soil will be under climate control and hence the values of the β's rise. This reversal behavior occurs where the median s equals s^* which is at $\delta > 1$ due to the characteristic skew of the gamma pdf.

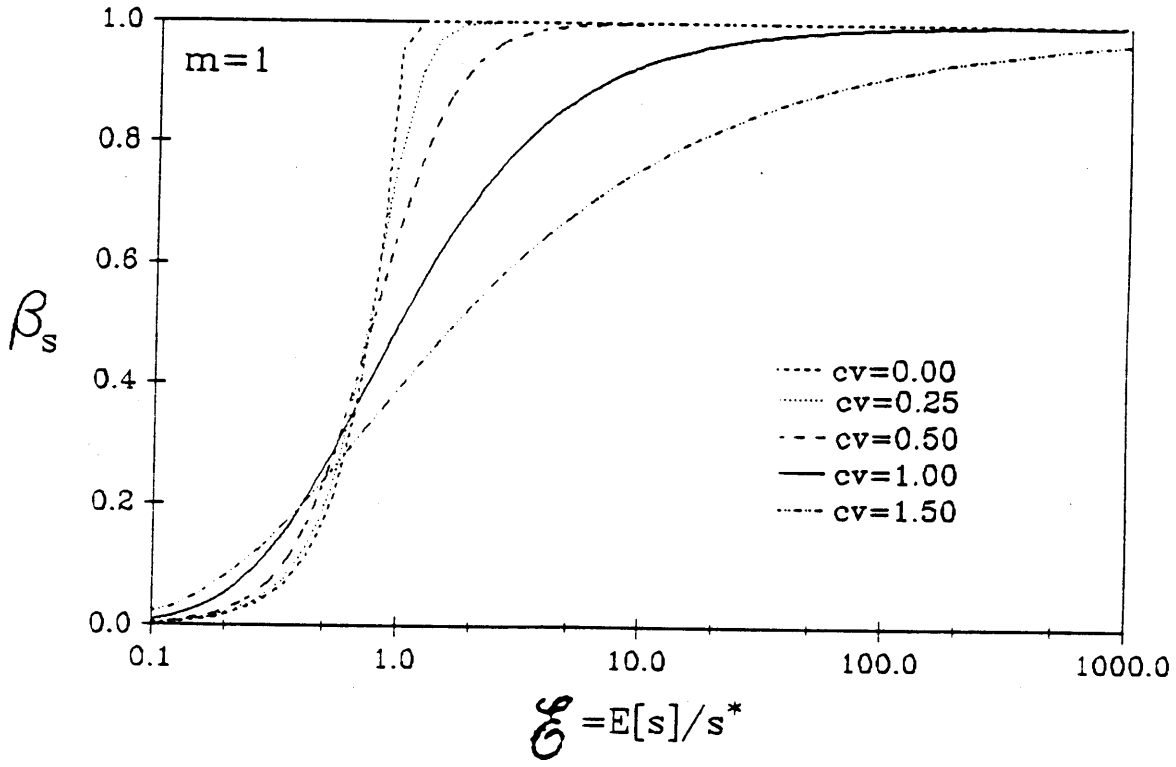

Fig. 2.10 Sensitivity of the bare soil evaporation efficiency to spatial variability of soil moisture with m = 1

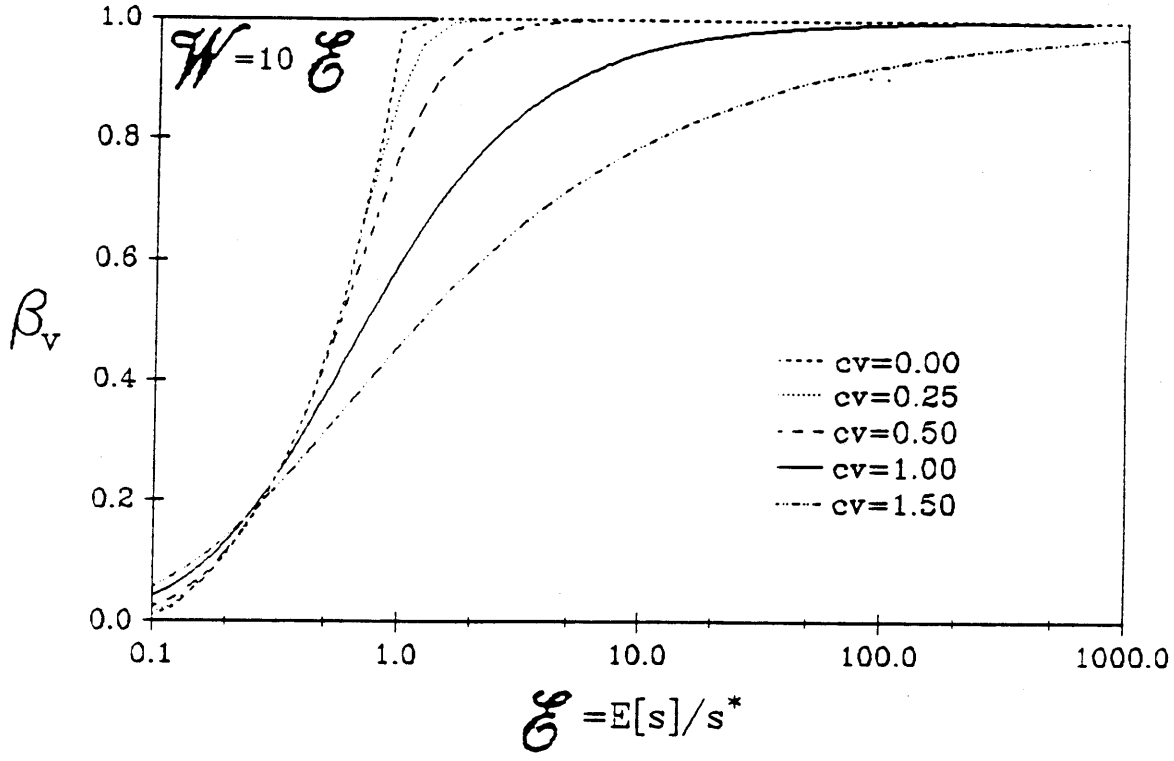

Fig. 2.11 Sensitivity of the transpiration efficiency function to spatial variability of soil moisture with $\mathcal{W} = 10$ $\mathcal{E}$ or $s_w = 0.1$ s*

4. *Implementation*

The practical use of the proposed subgrid parameterization of surface hydrologic processes described here requires the definition of several fixed parameters. Table 2.1 lists values that we consider to be reasonable.

The fractional wetting by rainfall events (κ) may be related to the relative size of the airmass parcel in GCMs that have moist convection parameterizations with variable plume fractions (Kuo–type). Remote sensing of variables such as outgoing longwave radiation may be used as a way to determine the climatology of convectively active areas within larger fields. Eagleson (1984) and Eagleson et al. (1985, 1987) demonstrate that generally about 60% of storm areas are actually wetted by rainfall. Depending on the ratio of the GCM grid area to typical storm areas, this value is proportionally scaled. For most GCMs in current use, typical storms cover about half of the grid area. We assume that large–scale condensation occurs over the entire storm area but convective precipitation covers 60% of the total storm area.

The *cv* of the subgrid distribution of surface soil moisture content may be intrinsically dependent on the grid mean value (Bell et al., 1980; Owe et al. 1982). It is strongly dependent on the area of the field used to compute the statistics of spatial heterogeneity. For areas on the order of 10^2 to 10^5 km^2, comparable to GCM grids, $cv = 1$ (exponential pdf) is a reasonable operational choice. With $\alpha = 1$, the analytical expressions are simplified considerably thus reducing the computational burden. Again remote sensing of soil moisture on fields with various areas and in different climates may provide clues as to the choice of *cv*.

Representative values for the empirical parameters K(1), $\Psi(1)$, and m used in characterizing the hydraulic properties of unsaturated soils are based on our interpretation of the case studies compiled by Mualem (1976, 1978). It should be noted that θ is the effective water content, i.e. the water content with the immobile

residual water content subtracted. The variable s is thus the effective relative soil saturation. Furthermore $\Psi(1)$, the 'saturated' matric potential is a parameter of the fitted moisture retention curve.

The thickness of the first soil layer appears explicitly as a parameter in the runoff parameterization. Its presence is only implicit in the bare soil evaporation efficiency function. The value of Δz for the runoff case must be comparable in magnitude to the effective depth of infiltrating water during GCM integration steps. In the presence of soil capillarity, we take Δz to be near ten centimeters. To be compatible with the assumption of a semi–infinite soil column in deriving the desorption rate equation, the effective depth of moisture extraction due to bare soil evaporation must be less than Δz. A depth of ten centimeters satisfies this criterion for the given typical GCM time–step T.

The vegetation wilting point matric potential and fraction of active roots in different layers depends on the data–base used in the GCM ground hydrology submodel. In Table 2.1 we present some typical values for the former.

Table 2.1 **Parameters of the surface hydrologic subgrid parameterization**

Rainfall	κ (fractional wetting)	Storm area to GCM grid area fraction for large-scale condensation. For moist convection, reduce this value 60% or relate to parcel size.		
Soils	*cv* (coefficient of variation)	1.0 (exponential) or tie to grid mean soil saturation		
	Δz (top layer thickness [m])	0.1		
		Sand	Silt	Clay
	m (soil pore-size distribution)	3.3	1.2	0.4
	K(1) (saturated conductivity) [10^{-3} m hr^{-1}]	7.5	2.2	0.3
	$\Psi(1)$ (saturated soil matric potential) [m]	0.23	0.46	0.93
	n (effective porosity)	0.25	0.35	0.45
Vegetation	Ψ_{wilt} (wilting matric potential) [10^2 kPa]	-15 for swamp plants and herbaceous crops; -15 to -25 for grasses; -15 to -25 for temperate zone woody species; -18 to -25 for conifers; and -55 to -90 for desert plants		

III. Extensions to the Basic Landsurface Hydrology Parameterization

1. Alternate formulation of the transpiration efficiency function

The transpiration efficiency function (Equation (2.43)) is based on the parameterized root soil–water extraction model

$$e_v(s) = \begin{cases} 0 & 0 \le s \le s_w \\ \dfrac{s - s_w}{s^* - s_w} e_p & s_w \le s \le s^* \\ e_p & s^* < s \le 1 \\ 0 & \text{saturated} \end{cases} \qquad (3.1)$$

This expression basically states that root soil–water extraction is completely suppressed below the plant wilting point (at soil saturation below s_w); it proceeds at the potential rate above the transitional soil saturation s^* (i.e., soil saturation at which the transition from a water–limited to a climate–controlled evaporative regime occurs); and the rate is linearly dependent on soil saturation between s_w and s^*.

Molz (1981) notes that, in modelling some vegetation and for some soils, the transpiration rate, between the wilting level and climatic transitional level, is linear in soil matric suction Ψ rather than soil saturation s. In this case

$$e_v(\Psi) = \begin{cases} 0 & 0 \le \Psi \\ \dfrac{\Psi - \Psi_w}{\Psi^* - \Psi_w} e_p & \Psi_w \le \Psi \le \Psi^* \\ e_p & \Psi^* < \Psi \le \Psi(1) \\ 0 & \text{saturated} \end{cases} \qquad (3.2)$$

With the Brooks and Corey (1966) parameterization for soil–water retention (Equation A.8),

$$\Psi(s) = \Psi(1)\, s^{-\frac{1}{m}} \tag{3.3}$$

we may write

$$e_v(s) = \frac{s^{-\frac{1}{m}} - s_w^{-\frac{1}{m}}}{s^{*-\frac{1}{m}} - s_w^{-\frac{1}{m}}} e_p \qquad \text{for } s_w \leq s \leq s^* \tag{3.4}$$

Again using the gamma spatial distribution for the surface soil saturation, we may write the transpiration efficiency function as

$$\beta_v = \frac{\lambda^\alpha}{\Gamma(\alpha)} \left\{ \int_{s_w}^{s^*} \frac{s^{-\frac{1}{m}} - s_w^{-\frac{1}{m}}}{s^{*-\frac{1}{m}} - s_w^{-\frac{1}{m}}} s^{\alpha-1} e^{-\lambda s}\, ds + \int_{s^*}^{\infty} s^{\alpha-1} e^{-\lambda s}\, ds \right\}$$

which evaluates as

$$\beta_v = 1 + \frac{\gamma(\alpha-\frac{1}{m}, \alpha\delta^{-1}) - \gamma(\alpha-\frac{1}{m}, \alpha\gamma^{-1}) - (\alpha\delta^{-1})^{-\frac{1}{m}}\gamma(\alpha, \alpha\delta^{-1}) + (\alpha\gamma^{-1})^{-\frac{1}{m}}\gamma(\alpha, \alpha\gamma^{-1})}{\Gamma(\alpha)\ \{(\alpha\delta^{-1})^{-\frac{1}{m}} - (\alpha\gamma^{-1})^{-\frac{1}{m}}\}} \tag{3.5}$$

where again

$$\gamma = \frac{E[s]}{s_w} \tag{3.6}$$

and

$$\mathscr{E} = \frac{E[s]}{s^*} \tag{3.7}$$

As evident analytically in (3.3), if m = −1 the solution for the linear–in–Ψ and the linear–in–s transpiration efficiency functions must be identical. This check validates Equation (3.5). For realistic values of the soil pore disconnectedness index (m), however, the transpiration efficiency will be higher since $s^{-\frac{1}{m}} > s$ for $0 \leq s \leq 1$ and $m > 0$. This is evident in Figure 1 where the transpiration efficiency function (linear–in–Ψ) is evaluated for the two soil mixtures (light and heavy) as defined in Chapter II. Also included, for comparison, is the linear–in–s transpiration efficiency function. Where the evaporative regime is mostly water–limited (low values of $\mathscr{E}$), the differences in the two approaches to transpiration efficiency are most apparent. Again this is due to the fact that $s^{-\frac{1}{m}} > s$ for $0 \leq s \leq 1$.

2. *Extension of the transpiration efficiency to multiple soil layers*

Of the three hydrologic processes considered so far (surface runoff, bare soil evaporation, and soil moisture extraction by plant roots), only the last may have direct influence on the deeper soil horizons. Surface runoff generation and the drying of exposed soil surfaces are processes whose instantaneous magnitudes depend primarily on the near surface soil conditions. In this section, we present an extension of the transpiration efficiency function to include soil moisture extraction by plant roots from multiple soil layers.

In the consideration of a multiple layer soil system, the subscripted indices on the relevant parameters will represent the characteristics of the respective soil level. The spatial heterogeneity within the large GCM grid area has again been modelled as a random process whose expectation is the mean grid condition. The realization

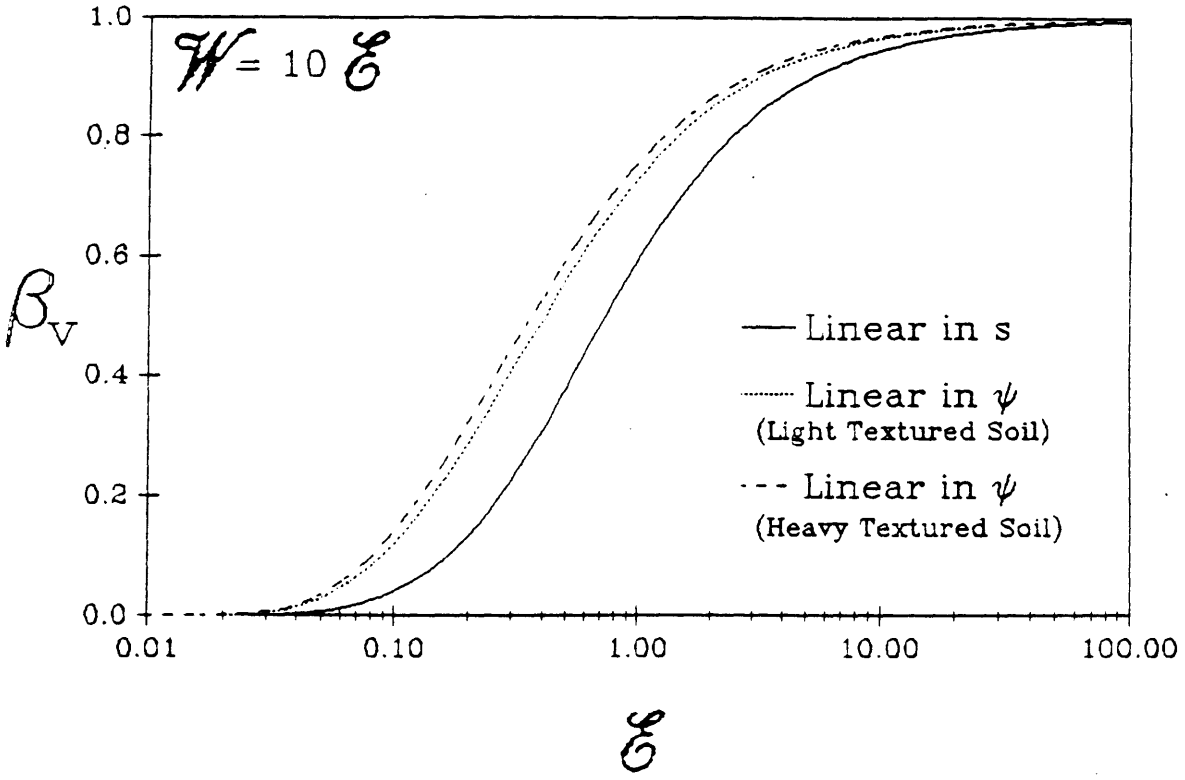

Fig. 3.1 The transpiration efficiency function with an alternate formulation of the root soil water extraction parameterization

of the process over all points in the GCM grid area follows a gamma distribution. Consider each such point to be the focus of a hydrologic subarea within the larger GCM grid area. In the parameterization of multiple soil layered systems, we assign a spatial probability density function to only one layer (e.g. topmost layer), hereafter referred to as the base–line process with subscript j. All other soil layers i ($i = 1,2, ..., N ; i \neq j$) have *no* probability distributions themselves, but their soil moisture states are dependent on the realization of the random process at the base–line level due to physical considerations. Within the same hydrologic subarea, we expect the soil moisture at all levels i ($i \neq j$) to be consistent with the base–line j–level process. We require that wet (dry) soil layers are not haphazardly stacked on dry (wet) adjacent layers within the same hydrologic subarea.

Though the soil moisture states at levels i ($i \neq j$) do not have explicit spatial probability distributions, we nevertheless require that they scale consistently with the realization of the base–line process in the manner

$$s_i = g(s_j) = \frac{s_j}{E[s_j]} E[s_i] \qquad i = 1,2, ..., N; \; i \neq j \tag{3.8}$$

We assume that the pdf shape parameter α is the same for all layers. This relation holds independently for all levels i when paired with the base–line level j process. The expectation of the soil moisture states over all hydrologic subareas at level i, as represented by (3.8), will be equal to the GCM grid–average value that is propagated in every model integration step. To define the transpiration efficiency for the i–th soil level, we produce the derived distribution of s_i given that the base–line process has a gamma spatial distribution. The basic step is to apply

$$f_{s_i}(s_i) = \left| \frac{\partial g^{-1}(s_i)}{\partial s_i} \right| f_{s_j}(g^{-1}(s_i)) \,, \tag{3.9}$$

which when evaluated becomes

$$f_{s_i}(s_i) = \left[\frac{\alpha}{E[s_i]} \right]^{\alpha} \frac{s_i^{\alpha-1}}{\Gamma(\alpha)} e^{-\frac{\alpha s_i}{E[s_i]}} \tag{3.10}$$

The result is a gamma derived distribution of the i–th level soil moisture point distribution in the hydrologic subareas with independent parameter $E[s_i]$. We may now proceed directly to the equations describing single–layer transpiration efficiency to evaluate the transpiration efficiency within a multi–layered soil system. Introduce subscript i to denote the transpiration efficiency [Eq. (2.40)] evaluated for the independent parameters of the i–th soil layer with a fraction ϵ_i of the available roots. The total transpiration efficiency now becomes

$$\beta_v = \sum_{i=1}^{N} \epsilon_i \beta_{v_i} \tag{3.11}$$

with the choice of the base–line process (level j) being arbitrary.

3. *Energy–balance considerations under climate–controlled and water–limited evaporative regimes at the subgrid scale*

a. *Statement of problem*

The water and energy balance at the landsurface are coupled through their common dependence on the surface vapor flux. Subgrid variability in the water

balance components will necessarily impose similar scale variability in the energy balance. Due to the coupling, a feedback develops. In this section, we will introduce a parameterization that captures the essential dynamics of the physical feedbacks as realized through the evapotranspiration term.

In our approach to landsurface–atmosphere interaction in GCMs, we are considering two distinct scales. At the larger grid–scale (hereafter also called the regional scale), the potential evaporation is estimated using the GCM grid moist thermodynamic variables under the assumption of climate–controlled evaporation over the *entire* grid area. At the smaller subgrid scale (hydrologic subareas), the actual evaporation rate is estimated by taking into account the subgrid distribution of soil moisture values and accordingly reducing the regional potential evaporation rate by a dimensionless efficiency factor. The subgrid variability in actual evaporation values leads to the subgrid variability in the energy balance as well. This is due to the fact that evaporation consumes large amounts of energy in the process of liquid–vapor phase–change. In those subareas with actual evaporation below the grid–average value, some energy is made surplus. The localized excess energy can feedback into altering the energy and water balance on the small scales. The possible consequences are changes in local temperature, decreased humidity, and increased (thermal) instability. These may lead to an increased effective potential evaporation rate. The detailed accounting of these differences is far too complicated to model directly. Instead, we exploit the existing distinction in scales and introduce a parsimonious parameterization including these subgrid scale energy balance variations.

We are interested specifically in the manner in which the actual evaporation rates of hydrologic subareas are modified by subgrid energy balance variations. We already know the uniformly climate–controlled regional potential evaporation by using GCM grid–values for air temperature, and humidity. We will now derive the

hydrologic subarea potential evaporation rates. The parameterization will loosely employ ideas known as "regional evaporation" in the hydrologic literature (Morton, 1965)(Brutsaert and Stricker, 1979). A critical assumption of this concept is that, over short time periods, the latent and sensible heat fluxes (λe and H) are the two major competitors for the available energy. The net radiative and deep ground heat fluxes (R_n and G) have far longer response times.

The concept of "regional evaporation" is still an unverified postulate in hydrology. The landsurface parameterization developed in Chapter II is extended to include the regional evaporation correction but the use of the modified equations should be preceded by detailed testing of the assumptions. In this respect, a numerical boundary layer model is well suited to test the hypothesis concerning the competition between λe and H within short time periods.

b. Derivation of potential evaporation rates for hydrologic subareas

The local energy balance with the hydrologic subarea evaporation rate is

$$R_n - G = \lambda e + H \tag{3.12}$$

Now introducing the effective potential evaporation for the same hydrologic subarea with subscript p,

$$R_{n_p} - G_p = \lambda e_p + H_p \tag{3.13}$$

In addition to e_p, we may define another quantity $\overline{\overline{e}}_p$. The potential evaporation $\overline{\overline{e}}_p$ represents the grid (uniform) rate that would be present if the entire grid area is under the climate–controlled evaporative regime. The quantity $\overline{\overline{e}}_p$, as opposed to the effective potential evaporation e_p, may be estimated readily from the GCM grid temperature and humidity prognostics. Under the uniformly

climate–controlled evaporative regime, the energy balance is

$$\overline{\overline{R}}_{n_p} - \overline{\overline{G}}_p = \lambda \overline{\overline{e}}_p + \overline{\overline{H}}_p \tag{3.14}$$

Proceed by subtracting (3.14) from both (3.12) and (3.13) to write

$$\begin{aligned} (R_{n_p} - \overline{\overline{R}}_{n_p}) + (\overline{\overline{G}}_p - G_p) &= (\lambda e_p - \lambda \overline{\overline{e}}_p) + (H_p - \overline{\overline{H}}_p) \\ (R_n - \overline{\overline{R}}_{n_p}) + (\overline{\overline{G}}_p - G) &= (\lambda e - \lambda \overline{\overline{e}}_p) + (H - \overline{\overline{H}}_p) \end{aligned} \tag{3.15}$$

When the evaporation rate at a hydrologic subarea is less than the potential for the grid as a whole, an amount of energy q is instantaneously made available over the subarea. The deficit in latent heat flux is immediately replaced by increased sensible heat flux from the surface. That positive amount of energy is therefore equivalent to the difference in the sensible heat fluxes

$$q = H - \overline{\overline{H}}_p \tag{3.16}$$

This surplus energy q now provides for possible increase in the hydrologic subarea energy consumption by latent heat exchange. The effective potential evaporation over the hydrologic subarea (e_p) now increases by consuming the excess energy q. When e_p is raised above $\overline{\overline{e}}_p$ due to the energy feedback, the competitor sensible heat flux H_p is accordingly reduced below $\overline{\overline{H}}_p$. This difference is also equal to q and may be written as

$$q = -(H_p - \overline{\overline{H}}_p) \tag{3.17}$$

Eliminate

$$q = (H - \bar{\bar{H}}_p) = -(H_p - \bar{\bar{H}}_p) \tag{3.18}$$

from (3.15), then add the two equations to write

$$(R_{n_p} - 2\bar{\bar{R}}_{n_p} + R_n) - (G_p - 2\bar{\bar{G}}_p + G) = \lambda(e_p - 2\bar{\bar{e}}_p + e) \tag{3.19}$$

At the time scale of GCM integrations, we can assume that the net radiation and deep ground heat flux components exhibit relatively minor spatial variations due to their relatively slow response to energy feedbacks. In other words, the sensible and latent heat fluxes are the chief competitors at the surface and over short time periods. We thus write (3.9) as

$$e_p = 2\bar{\bar{e}}_p - e \tag{3.20}$$

This is the expression that corrects the subarea effective potential evaporation rate e_p for subgrid variations in energy balance. Equation (3.20) relates the hydrologic subarea effective potential evaporation to the grid–average climate–controlled potential evaporation $\bar{\bar{e}}_p$. The energy feedback due to subgrid variability in the latent heat fluxes is parameterized in this simple though physically–based manner

Some of the limiting conditions of (3.20) are noteworthy. The lower limit of e_p occurs when energy–controlled climatic regime dominates the entire grid area. Then

$$\lim_{e \to e_p} e_p = \bar{\bar{e}}_p \tag{3.21}$$

When water is limiting, then (3.20), with increasing dryness, determines the upper limit to the effective potential evaporation as

$$\lim_{e \to 0} e_p = 2\bar{\bar{e}}_p \tag{3.22}$$

c. The bare–soil evaporation efficiency function

The bare–soil evaporation expression has explicit functional dependence on the potential evaporation rate over only a subset of all possible values of relative soil saturation s ($s \geq s^*$). For s in the interval $(0,s^*)$, the moisture flux from the bare–soil surface is parameterized as a desorptive process in porous media with idealized and fixed boundary conditions (function $\bar{f}_e$). Only over the interval (s^*,∞) the flux of moisture from the surface is limited by its potential value. Here the transitional relative soil saturation s^* is dependent on e_p. Doubling e_p, however, results in only minor changes in s^* as evident in Figure 2.7. The effects of subgrid scale spatial variability in e_p on s^* are not included in the following parameterizations.

With the gamma distribution of relative soil saturations over the grid area, we have the following expression for the bare–soil evaporation efficiency

$$\beta_s = \frac{E[\bar{f}_e]}{\bar{\bar{e}}_p} = \int_0^{s^*} \bar{f}_e \, f_s(s) \, ds + \int_{s^*}^{\infty} f_s(s) \, ds \tag{3.23}$$

which when evaluated becomes as before (2.28)

$$\beta_s = 1 - \frac{\gamma(\alpha, \alpha\mathscr{E}^{-1})}{\Gamma(\alpha)} +$$

$$\frac{K(1)\Omega}{\bar{\bar{e}}_p}\left[\frac{E[s]}{\alpha}\right]^{\frac{1}{2m}+2} \frac{\gamma(\alpha + \frac{1}{2m} + 2,\ \alpha\mathscr{E}^{-1})}{\Gamma(\alpha)} \qquad (3.24)$$

The energy–advection correction is introduced into the expression by the way of the accompanying equation relating the transitional relative soil saturation s* and the potential evaporation (2.29)

$$e_p = 2\bar{\bar{e}}_p - \bar{f}_e = \Omega\, K(1)\, s^{*\frac{m}{2}+2} \qquad (3.25)$$

Over the small interval (0,s*) the bare–soil evaporation function does not depend on the local potential evaporation rate (i.e. we use the desorption equation); with the bulk approximation $\bar{f}_e = E[\bar{f}_e]$ over this range, we write (3.25) as

$$\frac{K(1)\Omega}{\bar{\bar{e}}_p} = (s^*)^{\frac{m}{2}+2}\ (2 - \beta_s) \qquad (3.26)$$

Substituting (3.26) into (3.24) and noting as before

$$\mathscr{E} = \frac{E[s]}{s^*} \qquad (3.27)$$

results in an expression for the grid–average bare soil evaporation efficiency. The expression

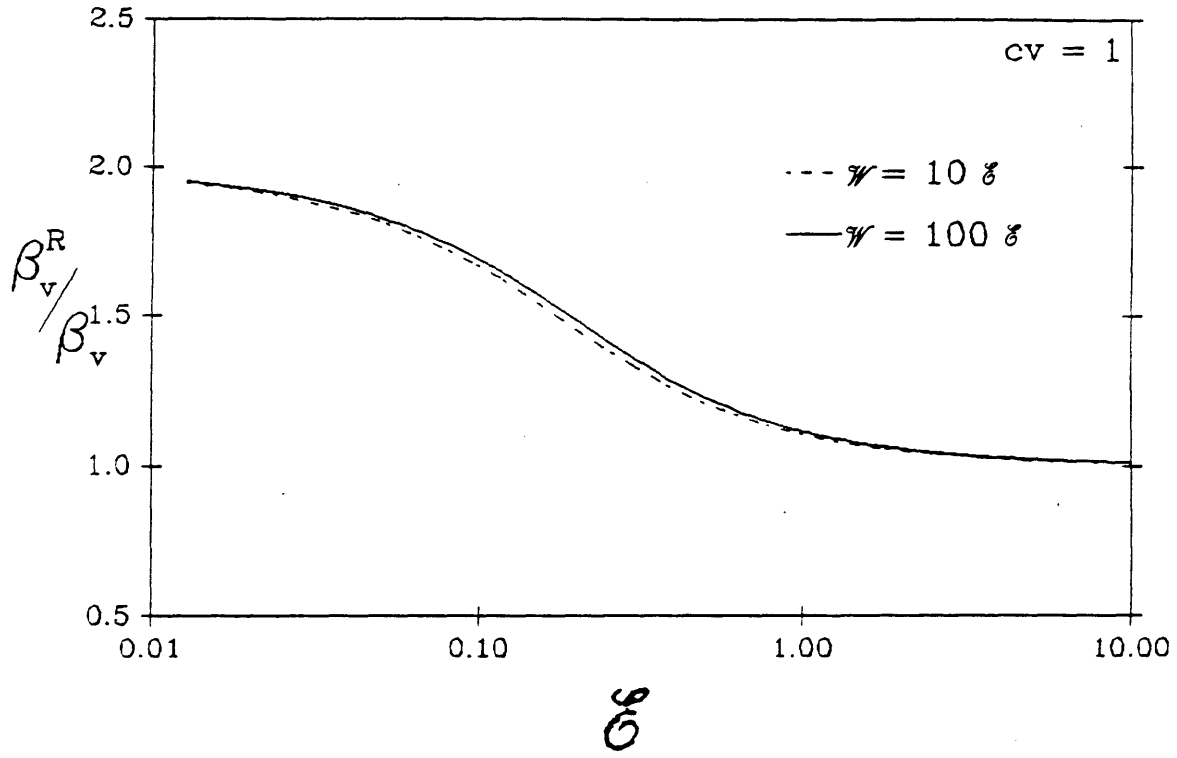

Fig. 3.2 Ratio of the energy–corrected bare soil evaporation efficiency function to the original function for various values of *cv*

$$\beta_s^R = \frac{\Gamma(\alpha) - \gamma(\alpha, \alpha\delta^{-1}) + 2(\alpha\delta^{-1})^{-\frac{1}{2m}} - 2\ \gamma(\alpha + \frac{1}{2m} + 2, \alpha\delta^{-1})}{\Gamma(\alpha) + (\alpha\delta^{-1})^{-\frac{1}{2m}} - 2\ \gamma(\alpha + \frac{1}{2m} + 2, \alpha\delta^{-1})} \tag{3.28}$$

is given the superscript R in order to distinguish the regional energy–balance correction that has been applied. To assess the effects of regional energy advection on the efficiency function, we consider the dependence of the ratio β_s^R/β_s on the dimensionless climate–soil parameter δ (Figure 3.2). For $\delta << 1$, the ratio asymptotically approaches 2. This is in agreement with the limit evident in (3.22). For energy–controlled evaporative regimes, $\delta > 1$, there is no significant surplus of energy due to non–potential vapor flux conditions in hydrologic subareas and, accordingly, the ratio tends to unity. The bare–soil evaporation efficiency with regional energy advection correction does not exceed unity anywhere even though its ratio with β_s rises as high as 2. This means that the moisture flux from the grid–area will never be above the GCM grid potential evaporation rate in magnitude.

Figure 3.2 also illustrates the effect of the *cv* of subgrid relative soil saturation on the β_s^R/β_s ratio. With the greater central distribution characterized by less spatial variance, the transition interval between climate–controlled and water–limited regimes becomes narrower. This is because the GCM grid point–values of relative soil saturations are more homogeneous with respect to the grid–mean when the spatial variability is low.

d. The transpiration efficiency function

Unlike the bare soil evaporation case, the transpiration function under both water–limited and energy–controlled climatic regimes depends on the hydrologic

subarea (local) potential evaporation rate even when $s < s^*$. The substitution of (3.20) into the transpiration function yields

$$e_v(s) = \begin{cases} 0 & 0 \le s \le s_w \\ (2\bar{\bar{e}}_p - e_v(s)) \frac{s - s_w}{s^* - s_w} & s_w < s < s^* \\ \bar{\bar{e}}_p & s^* \le s \le 1 \end{cases} \qquad (3.29)$$

which may be rewritten as

$$e_v(s) = \begin{cases} 0 & 0 \le s \le s_w \\ 2\bar{\bar{e}}_p \frac{s - s_w}{s^* - 2s_w + s} & s_w < s < s^* \\ \bar{\bar{e}}_p & s^* \le s \le 1 \end{cases} \qquad (3.30)$$

Similar expressions for the transpiration function in (3.2) are analytically intractable. The grid–average transpiration efficiency with the regional energy considerations is

$$\beta_v^R = \frac{E[e_v(s)]}{\bar{\bar{e}}_p}$$

$$= \frac{1}{\bar{\bar{e}}_p} \int_{s_w}^{s^*} e_v(s)\, f_s(s)\, ds + \int_{s^*}^{\infty} f_s(s)\, ds \qquad (3.31)$$

where $f_s(s)$ is the probability density function of subgrid relative soil saturations. With spatially gamma distributed s,

$$\beta_v^R = 1 - \frac{\gamma(\alpha, \alpha\mathscr{E}^{-1})}{\Gamma(\alpha)} + \frac{2e^{-\alpha\mathscr{W}^{-1}}}{\Gamma(\alpha)}$$

$$\int_0^{\alpha\mathscr{E}^{-1} - \alpha\mathscr{W}^{-1}} \frac{x(x + \alpha\mathscr{W}^{-1})^{\alpha - 1}}{x + (\alpha\mathscr{E}^{-1} - \alpha\mathscr{W}^{-1})} e^{-x} dx \tag{3.32}$$

where

$$\mathscr{W} = \frac{E[s]}{s_w} \tag{3.33}$$

For $\alpha = 1$, relative soil saturations exponentially distributed, an exact analytical closed–form expression for (3.32) is possible. For this case

$$\beta_v^R = 2e^{-\mathscr{W}^{-1}} - e^{-\mathscr{E}^{-1}} + \tag{3.34}$$

$$2(\mathscr{W}^{-1} - \mathscr{E}^{-1})e^{\mathscr{E}^{-1} - 2\mathscr{W}^{-1}}[Ei(2\mathscr{W}^{-1} - 2\mathscr{E}^{-1}) - Ei(\mathscr{W}^{-1} - \mathscr{E}^{-1})]$$

where Ei( ) is the exponential integral (see Gradshteyn and Ryzhik, 1980).

When $\alpha \neq 1$, the analytical integration of (3.32) is not possible. In Appendix C an accurate but approximate expression (**J**) for the integral in (3.32) is defined. With a closed–form expression for **J**, the transpiration efficiency function with correction for subgrid scale spatial variability in energy balance and $\alpha \neq 1$ becomes

$$\beta_v^R = 1 - \frac{\gamma(\alpha, \alpha\mathscr{E}^{-1})}{\Gamma(\alpha)} + \frac{2e^{-\alpha\mathscr{W}^{-1}}}{\Gamma(\alpha)} + \mathbf{J} \tag{3.35}$$

To assess the effects of regional energy considerations, we again plot the ratio β_v^R/β_v. Figure 3.3 illustrates the effects of the regional energy balance correction on

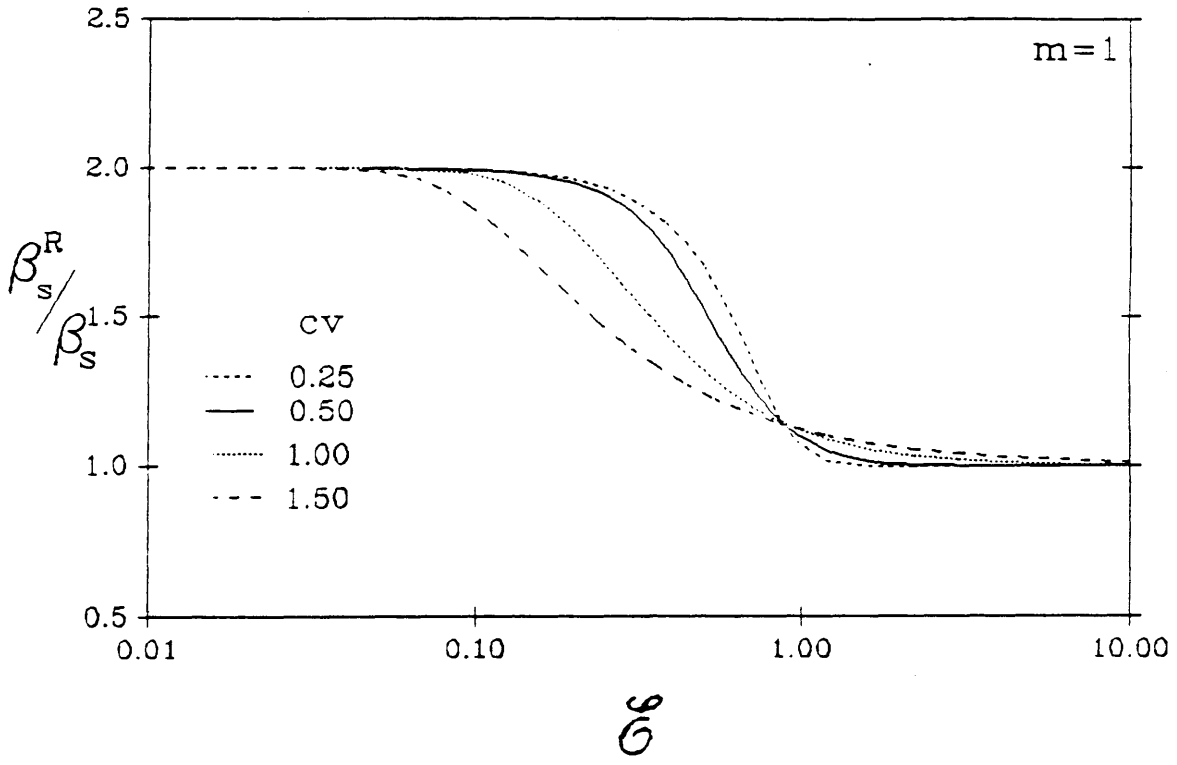

Fig. 3.3 Ratio of the energy–corrected transpiration efficiency function to the original function for $cv = 1$

the transpiration efficiency function at different values of δ. The ratio is asymptotic to the value 2 as required by (3.20). As more subareas within the grid become climate–controlled, the ratio β_v^R/β_v approaches unity. At high values of δ, the difference between regional and hydrologic subarea estimates of potential evaporation is reduced (i.e. $e_p = \bar{e}_p$) since much of the grid surface is under the climate–controlled regime and no significant amount of energy is made surplus by an vapor flux deficit.

IV. The Screening Model: Construct

1. *Basic issues in efficient low–dimensional climate models*

The climate results from the interaction of many processes whose time and space dimensions cover a wide range of the scale spectrum. At the uppermost end of the spectrum, global scale waves in the atmospheric fluid determine the dynamics of the climate. There are, continuing to smaller scales, a myriad of physical phenomena on every scale that in some way affect the climate. Finally, at the Ångstrom scale, the selective absorption of solar radiation by molecules results in the heating that drives the entire climatic system. Clearly no numerical model of climate can be assembled such that the dynamics of climatic processes over the entire scale spectrum may be explicitly represented. Instead, efficient three–dimensional climate models are equipped with autonomous *parameterizations* designed to represent different dynamic and thermodynamic processes present at unresolved scales. These components are generally classified under either *dynamic* or *physical* modules within the larger GCM model.

The dynamic components of GCMs simulate the mass fluxes within the three–dimensional mesh discretization of global atmosphere. In this sense, they capture all fluid dynamical processes that occur at the grid scale and larger. This component of the GCM basically contains the Momentum, State, and Thermodynamic equations whose dependent variables are the wind vector $\mathbf{u}_{xyzt}$, density ρ_{xyzt}, and pressure P_{xyzt} (five equations in five unknowns). Subject to specified initial and boundary conditions, these differential equations are solved numerically over the grid environment.

The physical components of GCMs are designed to represent those climatic processes whose dynamics, unlike $\mathbf{u}$, ρ, and P, cannot be resolved explicitly at the grid scale. They must, therefore, be *parameterized* within the model. There are

numerous aspect of climate that can only be parameterized; chief among them are radiative transfer, cloud processes, moist convection, water vapor condensation, landsurface hydrology, and sea–ice processes. Such subgrid parameterizations are central in the maintenance of the model climate. Furthermore, they are key in developing feedbacks when dealing with climatic variability.

The numerous feedbacks and teleconnections in the climatic system strongly depend on the coupling between processes modelled by the dynamic components and the physical parameterizations. The true nature of the model climate and its constituitive components can only be fully studied if they are all simultaneously present in the three–dimensional numerical laboratory. Of course, powerful computers are required to simulate this model climate.

When developing and testing new parameterizations for GCMs, problems emerge in studying the effects of the new code on the model climate. The computer costs for operating the full three–dimensional GCM is the obvious barrier to the extensive sensitivity analyses of parametizations via repeated simulation. Furthermore, extensive feedbacks present in the three–dimensional GCM make it difficult to isolate the specific climatic process under consideration.

In this regard, numerous GCM modelers have considered working with simplified versions of GCMs in order to screen various modifications before fully implementing them. There is, however, a trade–off in this practice. Simplifying the model by stripping various components results in a model that does not contain all the interactions and feedbacks characteristic of the GCM model climate. Depending on the application, nevertheless, various complexities may be removed such that the dynamics of the process under consideration is not seriously compromised.

In this application, the landsurface hydrology parameterization is the component of the GCM that is being modified. The objective here is to assemble a simplified GCM screening model such that the major climatic processes interacting

with the landsurface hydrology are present. It turns out that most of the physical parameterizations (radiative transfer, moist convection , water vapor condensation) are indispensable in such a screening model. They are all, incidently, one–dimensional processes in that their dynamics is confined to the vertical column of atmosphere. The landsurface hydrology parameterizations in GCMs are one–dimensional in the vertical as well.

Besides the physical parameterizations, however, the landsurface hydrology is dependent on the GCM model dynamics. The lateral convergence of heat and moisture at various locations within the three–dimensional model influences the surface heat and water balance.

The interaction of the landsurface hydrology and the large–scale dynamics of GCMs is, however, important mostly to establishing the climate at particular locations over the surface of the earth. Within the screening model context, the dynamic convergence of heat and moisture may be parameterized in order to perform sensitivity analyses of landsurface hydrology. A distinct advantage of parameterizing the model dynamics is that the screening model is then a completely one–dimensional apparatus. Its implementation and off–line use to a GCM is thus greatly simplified.

Several GCM modelers have used such screening models for the sensitivity analyses of landsurface hydrology parameterizations. Two notable among them are the Koster, Eagleson and Broecker (1988) and Warrilow (1986) one–dimensional climate models that were developed independently. In general the construct of these two models are similar. They consist of discrete atmospheric layers similar to the full GCM but over only one grid area. The radiation, hydrology, moist convection, and large–scale condensation components of the GCM, all one–dimensional processes, are solved for the atmospheric column. The time–step for the screening models, similar to their parameterizations, are entirely derived from their parent

GCM. The Koster, Eagleson and Broecker (1988) model is based on the NASA Goddard Institute for Space Studies (GISS) GCM while the Warrilow (1986) model is derived from the UK Meteorological Office climate GCM.

The differences in the two models is in their treatment of lateral heat and moisture convergence. The Koster, Eagleson and Broecker (1988) model relies on the observed climatology of heat and moisture convergence as evident in global atmospheric data assimilation publications. The Warrilow (1986) model is based on the multivariate generation of synthetic traces (statistical autoregressive time–series); the model parameters are based on the statistical properties (mean, variance, correlation) of similar time–series derived from simulating with the three–dimensional GCM.

In this report, a one–dimensional screening model is again used to perform preliminary sensitivity analyses on the landsurface hydrology parameterization for GCMs. The moist convection, hydrology, radiation, and vapor condensation modules of a GCM are used for developing the climate of an atmospheric column with discrete layers. The column overlies a hydrologically active soil profile.

The screening model used here is derived from the one developed by Koster, Eagleson and Broecker (1988). The primary point of departure between the two models is in their parameterization of lateral convergences. There are, however, numerous other differences; most notably in the radiative transfer component and, of course, the landsurface hydrology. In the next few sections, the structure of the screening model used here will be presented. Clearly, a complete description of the modules is infeasible here due to the enormous complexity of the modelled processes. Suffice that their basic construct, mostly based on current and familiar GCM practice, is described and outlined briefly.

2. *Model components*

The basic structure of the screening model is characterized by two adjoined atmospheric columns each divided into nine vertical levels similar to the GISS GCM (Hansen et al., 1983). The pressure levels are centered at 984, 917, 807, 650, 480, 329, 206, 105, and 27 millibars. For this model, due to the lack of dynamics, the pressure tendency is zero, i.e.

$$\frac{dP}{dt} = 0 \tag{4.1}$$

The two atmospheric columns are bordered by one–another as in two halves of a cylinder (see Figure 4.1). In this sense the model may be considered quasi two–dimensional, exhibiting zonal land–ocean contrasts. The adjacent atmospheric columns are characterized by distinct types of lower boundary; land and ocean surfaces respectively. For the column overlying the landsurface, an interactive 10 cm soil layer provides for landsurface hydrologic and thermodynamic exchange with the atmosphere. The ocean surface of the model has a fixed sea–surface temperature in order to account for the meridional flux of heat in the one–dimensional model. It also serves as an infinite source of moisture in the enclosed model.

The physical parameterizations of the screening model are largely based on the GISS GCM. In this respect, it contains a diurnal cycle. The basic time step is one hour; though the landsurface hydrology and radiative transfer modules have different time steps which will be discussed below.

a. *Heat and moisture convergence*

Since there are no dynamics within the model, it is necessary to parameterize the atmospheric convergence of heat and moisture. With parameterized mass

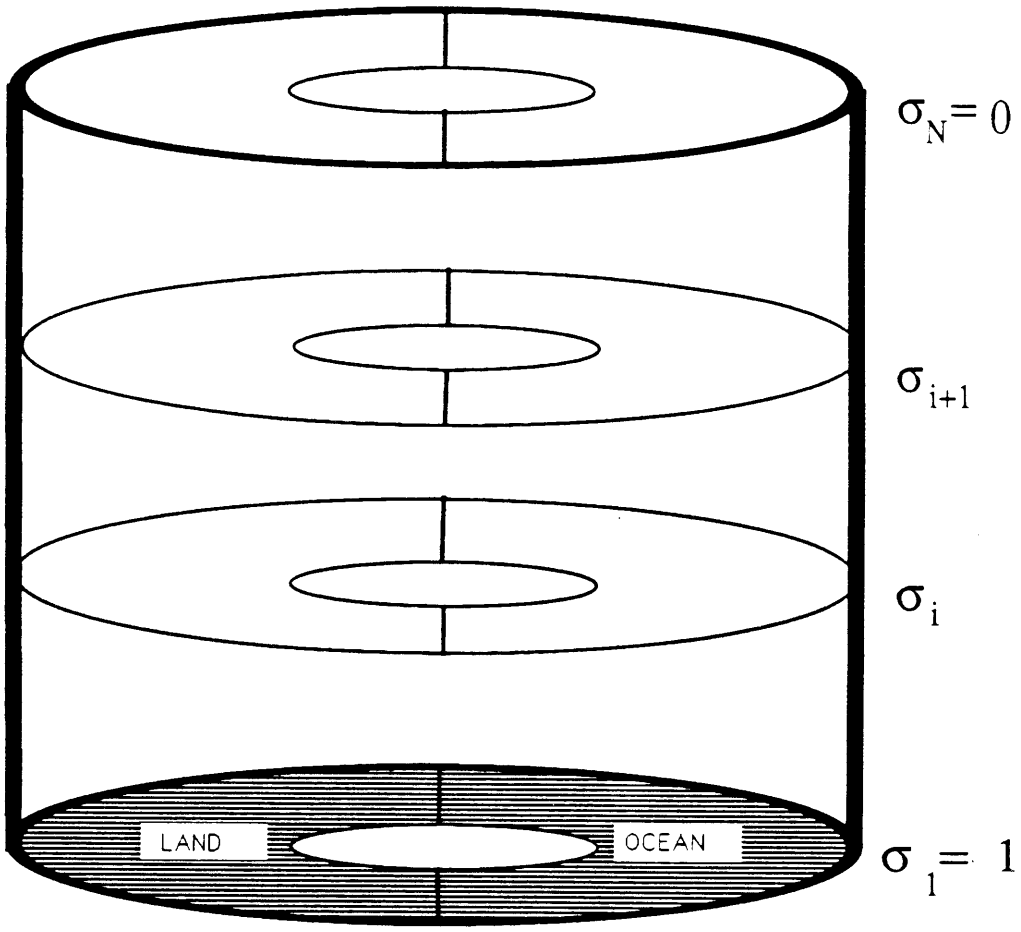

Fig. 4.1 A schematic of the screening model construct in $\sigma \left(= \frac{P}{P_s} \right)$ coordinates. Airmass exchange occurs between the independent discretized air columns over land and ocean

exchange between the land and ocean airmasses, the fixed ocean surface temperature serves as an infinite source of heat and moisture for the atmospheric column overlying the landsurface and ocean.

The heat and moisture flux from the ocean surface is mixed through the atmospheric column over the ocean (subscript o) by moist convection and radiative transfer processes. It is then transported over to the adjacent atmospheric column overlying the landsurface (subscript c for continent) by the following simple linear reservoir scheme,

$$\frac{df_{oi}}{dt} = \frac{f_{ci} - f_{oi}}{\chi}$$

$$\frac{df_{ci}}{dt} = \frac{f_{oi} - f_{ci}}{\chi} \qquad (4.2)$$

where, per unit mass,

$$f_i = \begin{cases} q_i & \text{moisture exchange} \\ c_p T_i & \text{heat exchange} \end{cases}$$

Here q_i and T_i are the specific humidity and temperature at level i in the atmosphere and c_p is the specific heat of air at constant pressure.

The linear reservoir parameter χ (units : T) is prescribed for the model. Exchange only occurs between land and ocean atmospheric masses at the same pressure level.

b. *Precipitation processes*

Moist convection and condensation processes produce precipitation and vertical mixing in the screening model. Both physical parameterizations are largely

based on the GISS GCM (Hansen et al, 1983) and the one–dimensional model of Koster, Eagleson, and Broecker (1988).

1. *Moist convection*

The moist convective scheme is based on the parcel method for finite amplitude stability analysis in an atmospheric column. By this method, a parcel of atmospheric mass is mechanically and moist adiabatically lifted through the air column until it becomes negatively or neutrally buoyant. The criterion of buoyancy is the saturated moist static stability.

In a moist convective event, the saturated moist static energy of a fraction of the airmass from the lowest atmospheric level is compared with that of the airmass in the next higher level. If the parcel is convectively unstable, the parcel is lifted moist adiabatically to the higher level. Comparisons are again made with the moist static energy of the airmass lying directly above the current parcel location. The parcel continues to move through the air column until it encounters an atmospheric level with respect to which it is neutrally (or negatively) buoyant. When the parcel from the first atmospheric level finally finds its point of neutral buoyancy, an equal amount of airmass at every atmospheric level in the path of the parcel undergoes adiabatic subsidence to the next lower level. Now beginning at the level where the parcel was finally deposited, supersaturated air is allowed to condense until it is only 100% saturated. The water substance is then deposited in the next lower level. The supersaturated moisture within the airmasses below the final parcel location are again removed as liquid water. If droplets fall into unsaturated air, they are evaporated until saturation is achieved at that atmospheric level. The latent heat of all condensation–evaporation events is accounted for in the parameterization.

Once the airmass and condensate tracking is completed for the parcel from the lowermost atmospheric level, a parcel is then taken from the next higher

atmospheric level. It is subjected to the same lifting and condensation–evaporation procedure as outlined for the parcel from the lowermost atmospheric level.

After completing the parcel test for all the levels and properly accounting for the precipitating condensates, the water mass that successfully reaches past the lowermost atmospheric level without completely evaporating in its descent from the higher atmospheric levels is considered to be precipitation at the surface.

The movement of the parcel in the atmospheric column, in the case of the screening model which has no dynamics, does not involve any momentum exchange. The size of the parcel is defined as the fixed fraction of the airmass at any level in the atmosphere. That fraction is set at 0.5 after the parameterization in the GISS Model II GCM; therefore moist convection involves half the airmass per unit area.

2. *Vapor condensation*

Prior to allowing for moist convection, however, precipitation due to large–scale condensation is removed. When lateral heat and moisture exchange between adjacent atmospheric levels in the screening model results in supersaturated airmass, condensation is allowed to take place until the airmass is only 100% saturated. That amount of condensed water is allowed to fall through the air column and evaporate if necessary. The latent heat of phase change is accounted for in both the condensation and evaporation processes. That amount of water droplets that finally reach past the lowest atmospheric level is considered to be surface precipitation.

c. *Radiative fluxes and heating*

The radiative transfer scheme used in the screening model is entirely different from both the one at GISS and the parameterization in the one–dimensional model of Koster, Eagleson, and Broecker (1988). The GISS radiation parameterization is

far too complicated and computationally burdensome. The scheme in the model of Koster, Eagleson, and Broecker (1988), on the other hand, is simple and efficient. It does not, however, allow for the interaction of moisture, clouds, and transient temperature profiles with the radiative fluxes.

Here, we modify the radiative equilibrium model of Hoffman (1981) to serve as a GCM radiation module. This scheme is not as computationally demanding as the GISS module; nevertheless it is more interactive with exact profiles of temperature, moisture, and absorber gases than the one used by Koster, Eagleson, and Broecker (1988).

A complete description of the Hoffman (1981) one–dimensional radiative equilibrium model is not contained in this report. Here we simply outline the basic methodology and document the more important modifications we incorporated in order to use the scheme as a module for climate models.

The radiation model treats solar and thermal radiation independently. The absorber gases are H_2O, CO_2, O_3, and O_2 with the absorption spectrum in Figure 4.2. The CO_2 and O_2 gases are assumed to be uniformly mixed in the atmosphere; O_3 is distributed based on climatology. The vertical mixing ratio profiles of O_3 over different latitudes and seasons are based on the observational data published by Dopplick (1970).

The radiation model interacts with the cloud cover. For thermal radiation calculations, clouds are treated as blackbodies. Clouds are diffuse reflectors–transmitters of solar radiation. The model assumes an infinite, homogeneous plane–parallel atmosphere.

The thermal radiative flux at level j in the atmosphere, after spectral integration, is

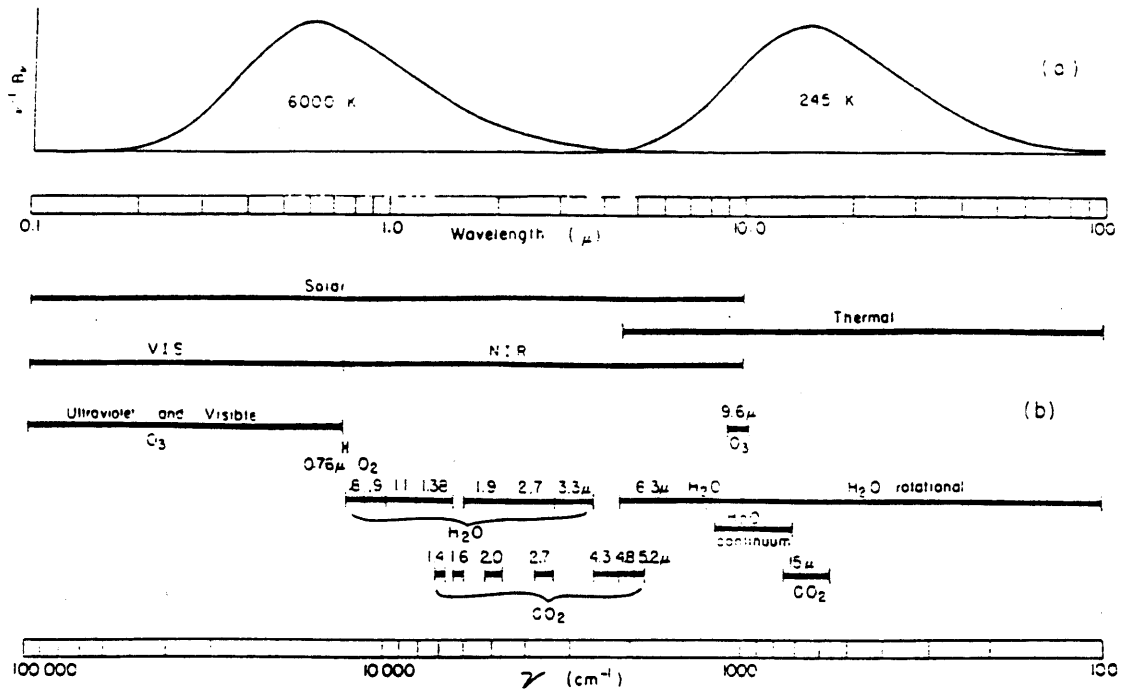

Fig. 4.2 The thermal and solar absorption spectra of the radiation parameterization (from Hoffman, 1981)

$$F_j = B_0 T_{j1} + \sum_{i=1}^{n} B_i C_{ij} - B_{n+1} T_{jn+1} \qquad (4.3)$$

where B is the Planck source function, T_{ij} is the transmission function between levels i and j, and C_{ij} is the Curtis matrix

$$C_{ij} = \begin{cases} T_{j2} - T_{j1} & i=1 \\ T_{ji+1} - T_{ji-1} & i=2, \ldots, n \\ T_{jn+1} - T_{jn} & i=n+1 \end{cases} \qquad (4.4)$$

The first level is the lowest atmospheric box centered at 984 millibars. The n+1 level is an artificial level above the topmost model level (above 27 millibars) and extends up to near zero pressure. The land and ocean surface temperatures (T_g or SST) are directly incorporated in the source function B_0. The thermal transmission function employs the Goody random model for H_2O intervals and the Malkus random band model for the 9.6μ O_3 wavelength.

The Hoffman (1981) radiation model computes daily solar radiation; i.e. the model integrates over the hour angle τ. For climate model applications, it is necessary to add the hour angle to the program in order to simulate the diurnal cycle. We have implemented the necessary modifications and outline them below.

The average flux over a period $\Delta\tau$ (several hours) and at wavelength r is

$$F_r(z) = \frac{1}{\Delta\tau} \int_{\tau_1}^{\tau_2} F_r(z,\tau)\, d\tau \qquad (4.5)$$

where $\Delta\tau = \tau_2 - \tau_1$. Let

$$x = \frac{\tau - \tau_1}{\Delta\tau} \qquad (4.6)$$

and write (4.5) as

$$F_r(z) = \int_0^1 F_r(z,\tau_1 + x\,\Delta\tau)\,d\tau \tag{4.7}$$

Numerical integration by gaussian quadruture gives

$$F_r(z) = \sum_j w_j\ F_r(z,\tau_1 + x_j\,\Delta\tau) \tag{4.8}$$

where

$$0 \le x_j \le x_{j+1} \le 1$$

and

$$\sum_j w_j = 1$$

The hour angle ranges in the interval $[\,0\,,\,\frac{\pi}{2}\,]$ and its is symmetric around noon ($\tau = 0$). The hour angle of sunrise and sunset is

$$H_s = \cos^{-1}\left[\,-\frac{\sin\ \varphi\ \ \sin\ \delta}{\cos\ \varphi\ \ \cos\ \delta}\,\right] \tag{4.9}$$

where φ is the latitude and δ is the seasonal solar angle parameterized as

$$\delta = \frac{23.45\ \pi}{180}\cos\left[\,2\pi\,\frac{172\ -\ D}{365}\,\right] \tag{4.10}$$

The solar angle is a function of the Julian day D. The numerical integration of (4.8) is straightforward unless τ_1 occurs before sunrise or τ_2 falls after sunset. We thus require that

$$\tau_1 = \min (\tau_1 , H_s) \qquad \text{mornings}$$

$$\tau_2 = \min (\tau_2 , H_s) \qquad \text{afternoons} \tag{4.11}$$

The solar flux, integrated over all wavelengths r, is also broken into paths i depending on the abundance of the absorber–reflector gases and clouds. Rewriting the solar flux expression (4.5) in terms of these paths gives

$$F(z) = \sum_i \sum_j \sum_r w_j \cos \psi_j \, \delta_{ijr} \, S_r \, T(u_{ijr}) \tag{4.12}$$

where S_r is the solar constant, δ_{ijr} is the weight for the i–th traced solar ray, and $T(u_{ijr})$ is the solar transmission function. Here the solar zenith angle ψ_j is integrated by gaussian quadrutures. The solar zenith angle is

$$\cos \psi = \sin \varphi \sin \delta + \cos \varphi \cos \delta \cos \tau \tag{4.13}$$

where φ is the local latitude. The transmission function is dependent on the absorber mixing ratios encountered in the path. It is parameterized with a high–order Curtis–Godson approximation. In the near infrared H_2O, CO_2, and O_2 are considered. O_3 is a major contributor in the visible/ultra violet range.

Since the time scale associated with radiative heating is on the order of several hours, it is not necessary to compute the fluxes at the hourly model time step. When the radiation time step Δt_{rad} is large, however, the diurnal cycle of surface fluxes and temperature is seriously misrepresented. This is evident in Figures 4.3 and 4.4 where the averaged diurnal cycle for landsurface latent heat flux

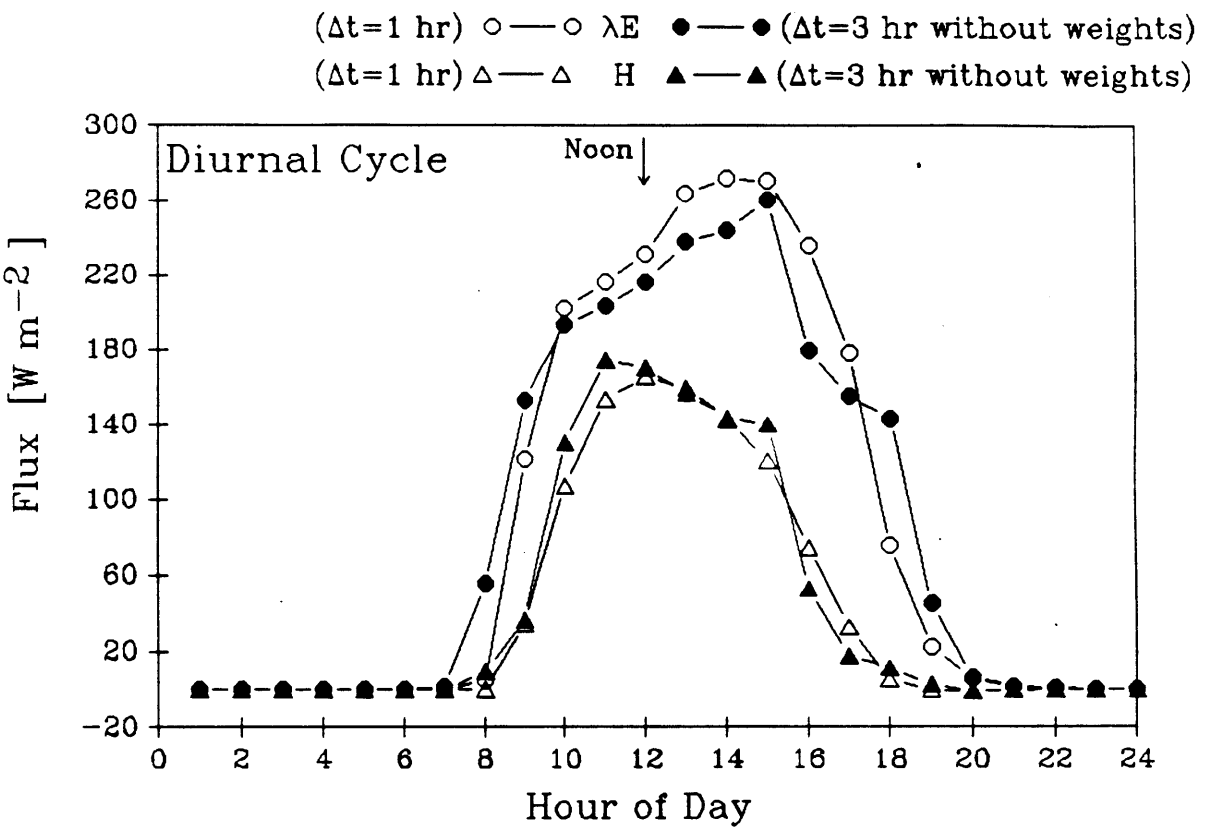

Fig. 4.3 Diurnal cycle of averaged–hourly latent heat (λE) and sensible heat fluxes for Δt_{rad} = 1 hour and Δt_{rad} = 3 hours without the weighting scheme

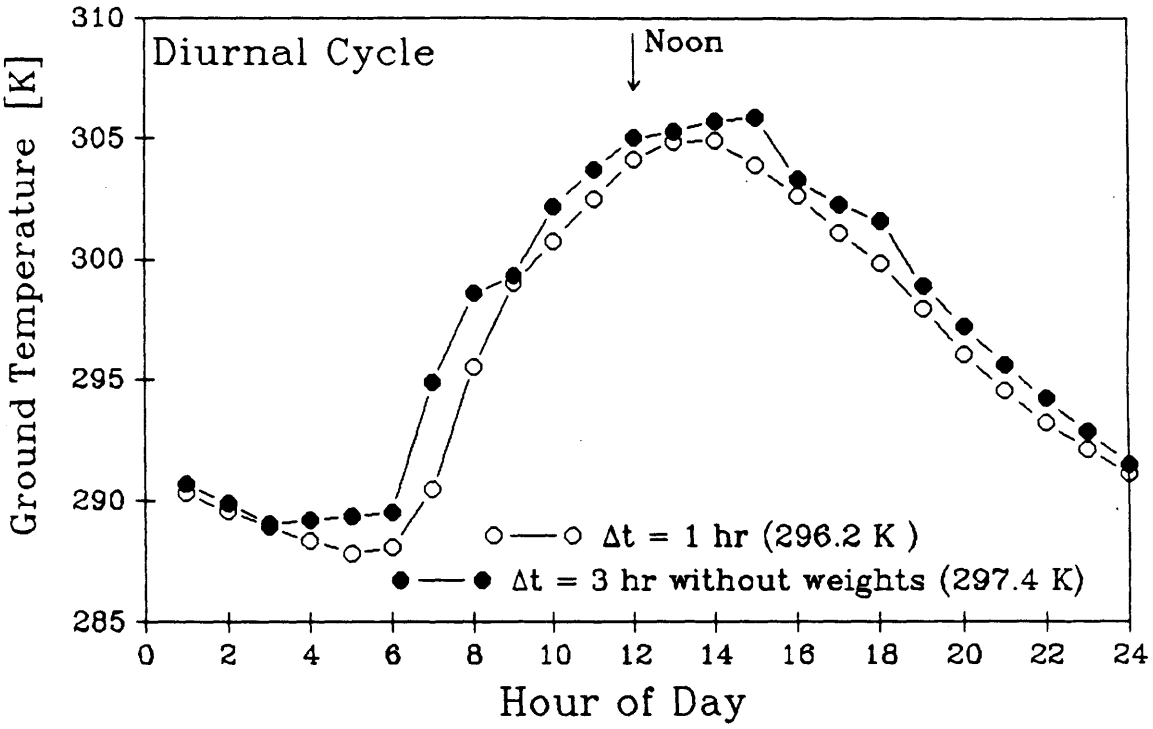

Fig. 4.4 Diurnal cycle of averaged–hourly ground temperatures for Δt_{rad} = 1 hour and Δt_{rad} = 3 hours without the weighting scheme

(λE), sensible heat flux (H), and ground temperature (T_g) are plotted versus time of day. Each graph contains plots for Δt_{rad} = 1 hour and Δt_{rad} = 3 hours computations. The Δt_{rad} = 1 hour plot for λE, H, and T_g are smooth and they furthermore preserve the characteristic secondary early afternoon peak in λE due to the post–noon maximum of T_g. The Δt_{rad} = 3 hours diurnal cycles in λE, H, and T_g are coarse when compared with Δt_{rad} = 1 hour plots. More troubling, though, is the mean bias of the diurnal cycles. In Figure 4.4, for example, the mean daily ground temperature for the Δt_{rad} = 1 hour integration is 296.2 °K. The Δt_{rad} = 3 hours curve is consistently above the shorter Δt_{rad} plot and its daily mean is 1.2 °K higher. The differences in the Δt_{rad} period results in different climates.

This error is considerably reduced by introducing a weighting scheme whose results are illustrated in Figures 4.5 and 4.6. In these graphs the plots for diurnal cycle of λE, H, and T_g with Δt_{rad} = 1 hour are reproduced. Superposed on these curves are the diurnal plots for the same variables with Δt_{rad} = 3 hours with a weighting scheme. The λE and H curves for Δt_{rad} = 1 and Δt_{rad} = 3 hours with weights coincide well. The ground temperature diurnal plots are also overlapping. The mean daily temperature in both cases is 296.2 °K.

The weighting scheme allows Δt_{rad} in the screening model to be larger than the model time step without significant loss in accuracy. The resulting climates with Δt_{rad} = 1 and Δt_{rad} = 3 hours *with weights* are comparable. With Δt_{rad} = 3 hours, however, the model is computationally nearly three times faster than with Δt_{rad} = 1 hour since the radiation module is the major consumer of computer processor time.

The weighting scheme differentiates between solar and longwave radiation. For the longwave radiation, the heating and fluxes estimated when the radiation subroutine is called (time $\tau = \tau_1$) are distributed over the period Δt_{rad} according to

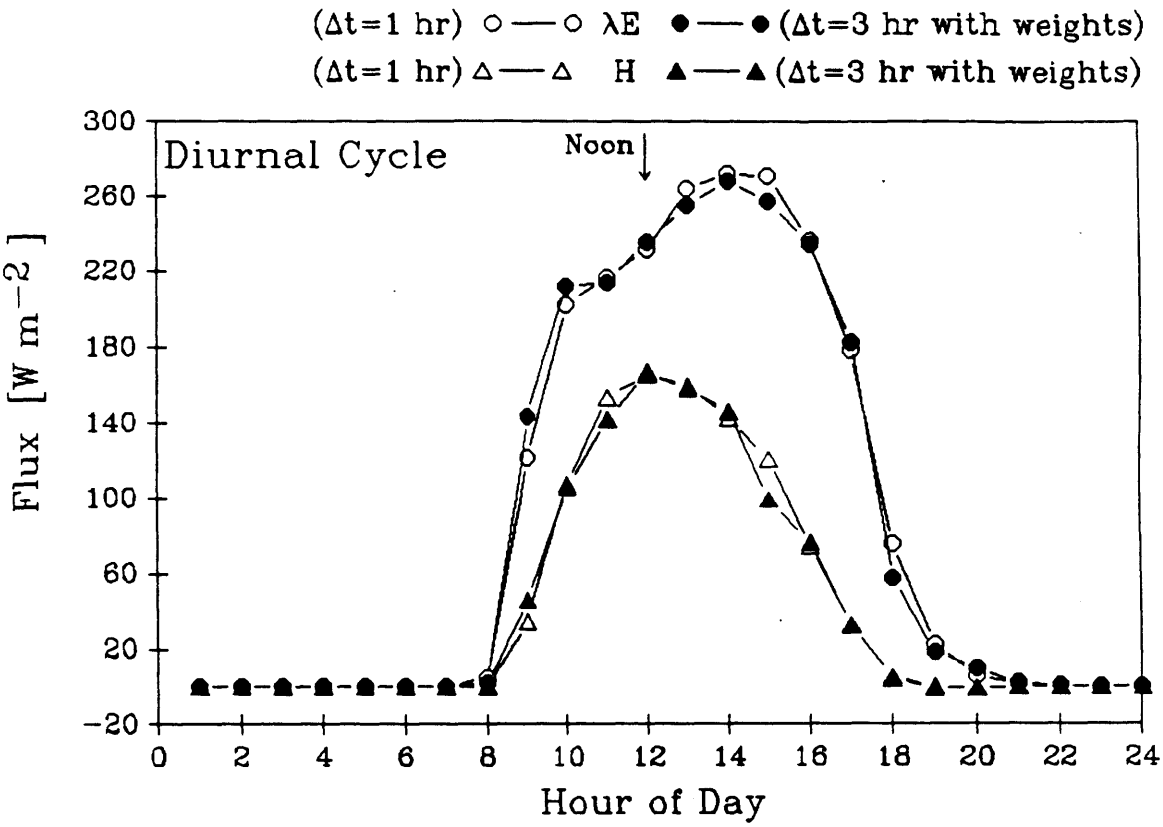

Fig. 4.5 Diurnal cycle of averaged–hourly latent heat (λE) and sensible heat fluxes for Δt_{rad} = 1 hour and Δt_{rad} = 3 hours with the weighting scheme

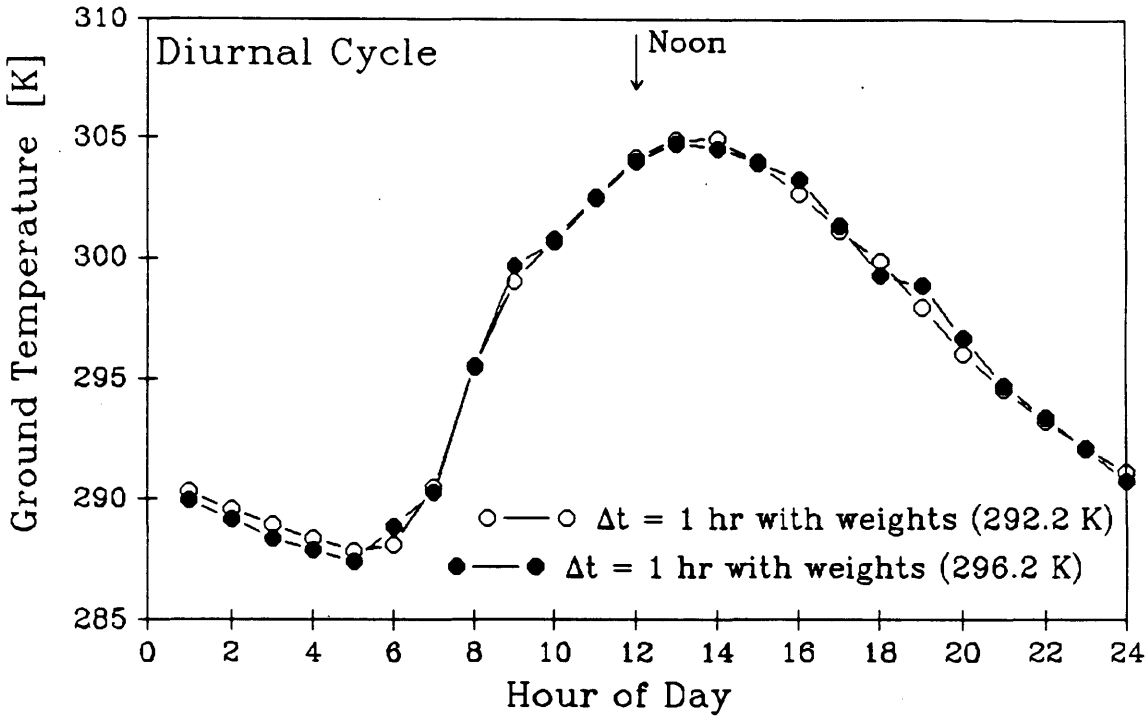

Fig. 4.6 Diurnal cycle of averaged–hourly ground temperature for Δt_{rad} = 1 hour and Δt_{rad} = 3 hours with the weighting scheme

$$\omega_\tau = \Delta t_{rad}^{-1} \qquad \tau \in [\, \tau_1 , \tau_1 + \Delta t_{rad} \,] \tag{4.14}$$

For shortwave radiation, the weights are

$$\omega_\tau = \frac{\cos \tau}{\int_{\tau_1}^{\tau_1 + \Delta t_{rad}} \cos t \, dt} \qquad \tau \in [\, \tau_1 , \tau_1 + \Delta t_{rad} \,] \tag{4.15}$$

The weights are averaged over the discrete model time step $\Delta\tau$ as

$$\omega_j = \int_{\tau_1 + (j-1)\Delta\tau}^{\tau_1 + j\,\Delta\tau} \omega_\tau \, d\tau \tag{4.16}$$

Sunrise and sunset may occur within a $\Delta\tau$ or Δt_{rad} period. Constraints similar to (4.11) are therefore necessary in the practical implementation of this weighting scheme.

d. *Clouds*

Clouds affect the radiative transfer in the atmosphere and may thus have significant influence on the surface energy balance. Neither in this model nor in any operational climate model are clouds treated in a physically–realistic manner. In some GCMs (e.g. GFDL), clouds are simply assigned based on climatology. In several other GCMs, cloud covers are estimated using arbitrary functions that depend on temperature and humidity.

In the screening model assembled here, we also use an arbitrary function; but this function is dependent on temperature and moisture in a manner that greater cloud cover is assigned when the preconditions for saturation are at hand.

We assume that the grid temperature is the areal mean of spatially normally distributed subgrid conditions. The degree of spatial variability is signified by the standard deviation σ_c. Now the fraction of the grid that is characterized by temperatures below a threshold temperature T*, the temperature at which the airmass vapor pressure equals its saturation value, is considered to be the cloud fraction.

With the integrated Clausius–Clapeyron equation

$$e_s(T) = e_{so} \exp \left\{ \frac{\lambda}{R_v} \left(\frac{1}{T_o} - \frac{1}{T} \right) \right\} \tag{4.17}$$

we find the threshold temperature below which saturation occurs by the substitution

$$e = e_s(T^*) = e_{so} \exp \left\{ \frac{\lambda}{R_v} \left(\frac{1}{T_o} - \frac{1}{T^*} \right) \right\} \tag{4.18}$$

Solving for T* gives

$$T^* = \left[\frac{1}{T_o} - \frac{R_v}{\lambda} \log \left\{ \frac{q\ P}{e_{so}\ (\epsilon + q)} \right\} \right]^{-1} \tag{4.19}$$

since $q = \frac{\epsilon\ e}{P - e}$.

Now the fraction of the grid box with $T \leq T^*$ is

$$\Phi\left(\frac{T - T^*}{\sigma_c} \right) \tag{4.20}$$

where $\Phi( )$ is the cumulative density function for the standard normal distribution.

Table 4.1 gives the radiative properties of clouds in the model. They are based on the climatology determined by Dopplick (1970).

The sensitivity of the radiation scheme to σ_c is determined through four simple simulation experiments with the screening model. These experiments vary the value of the parameter σ_c while keeping the remaining aspects of the model constant. A fixed exchange coefficient ($\chi = 1.67$) is used along with subgrid hydrology and $cv = 1$ for a light soil. The simulation is perpetual July at 15^0 North latitude.

Table 4.2 summarizes the simulation results. The parameter σ_c is set at discrete values of 1, 3, and 5 ^{0}C for each simulation. A fourth simulation experiment prescribes an altogether cloud–free atmosphere at all times.

The diurnally–averaged ground temperature in the simulation with $\sigma_c = 1$, 3, and 5^0 C are within 2.6 ^{0}C of one another but no simple pattern is visible between the magnitudes of T_g and σ_c. The range in the mean diurnal temperatures are comparable ($18^0 \pm 0.6$ ^{0}C). The net incoming solar and net outgoing longwaves radiation exhibit similar behavior.

The striking differences are, however, between model simulations with and without cloud cover (compare runs I–41, –42, and –43 with I–44 in Table 4.2). With reduced atmospheric albedo associated with the removal of all cloud cover, the net incoming solar radiation increases in magnitude by nearly 25%. Meanwhile, the net longwave radiative loss at the surface is greatly increased (near 45%). The absence of cloud back–radiation in the longwave directly leads to greater net longwave radiation loss at the surface. Increased longwave cooling at the surface and increased diurnal cycle in solar radiation result in reduced average ground temperature as well as a significantly increased diurnal cycle in T_g. The diurnal amplitude in ground temperature in the absence of cloud cover is 24 ^{0}C versus near 18 ^{0}C when clouds are present.

Table 4.1: Radiative Properties of Clouds

	Level	Reflectance
Visible	300 – 0 mb	0.21
	800 – 300 mb	0.54
	1000 – 800 mb	0.66
NIR	300 – 0 mb	0.19
	800 – 300 mb	0.46
	1000 – 800 mb	0.50

Table 4.2: Screening model sensitivity to cloud parameter σ_c.

Run	σ_c	T_g Mean ^0K	T_g Range ^0K	Net Solar Flux W m^{-2}	Net Longwave Flux W m^{-2}
I–42	1	297.0	18.6	196.3	68.9
I–41	3	296.3	17.4	192.9	64.5
I–43	5	298.9	17.6	223.3	63.1
I–44	(no clouds)	292.5	24.6	250.9	95.6

In summary, no clear trend is present in varying σ_c in the range 1 to 5°C. The model is generally insensitive to σ_c in this range. An operational parameter value of $\sigma_c = 3$ °C is used in all subsequent simulations.

In an qualitative sense, as evident in comparing the model simulations with and without cloud cover, the presence of clouds is necessary for maintaining a realistic diurnal cycle in surface radiation balance.

e. *Landsurface hydrology and ocean surface*

The landsurface module consists of prognostic equations to update the ground soil water content and temperature at every model time step. This component, similar to the GISS Model II (Hansen et al, 1983), also contains a surface air layer between the ground and the first atmospheric level. The heat and moisture fluxes from the ground to the surface layer are constrained to be equal to the same fluxes from the top of the surface layer to the height of the first atmospheric level. A similar structure, though with different surface layer thickness, is assumed over the ocean surface.

The heat and moisture prognostic equations for the soil layer are

$$n \, \Delta z \, \frac{ds}{dt} = P - R \, P - \beta \, e_p \tag{4.21}$$

and

$$(c_g + c_w \, \rho \, n \, s \, \Delta z \,) \, \frac{dT_g}{dt} = R_s - R_o - \lambda \, \beta \, e_p - H \tag{4.22}$$

where

n = soil porosity

Δz = soil depth (10 cm)

s = relative soil saturation

P = precipitation

R = runoff ratio

β = evapotranspiration efficiency

c_g = dry soil heat capacity (1.13×10^6 J m^3 K^{-1})

c_w = liquid water heat capacity

ρ = liquid water density

R_s = net incoming solar radiation

and R_o = net outgoing longwave radiation.

The potential evaporation e_p and sensible heat flux H between the ground and the surface layer are parameterized as

$$H = \rho\, c_p\, C_f\, V_s\, (T_g - T_s) \tag{4.23}$$

and

$$e_p = \rho\, C_f\, V_s\, (q_{sat}(T_g) - q_s) \tag{4.24}$$

where

c_p = heat capacity of dry air at constant pressure

C_f = heat and humidity transfer coefficient

and V_s = wind speed (2 m s^{-1} over land and 4 m s^{-1} over ocean).

The subscript s refers to the top of the surface layer.

Similarly, the fluxes between the surface layer and the first atmospheric level (subscript 1) are

$$H = \rho\, c_p\, K \left[\frac{T_1 - T_s}{z_1 - z_s} \right] \tag{4.25}$$

$$\beta\, e_p = \rho\, K \left[\frac{q_1 - q_s}{z_1 - z_s} \right] \tag{4.26}$$

where K is another transfer coefficient. Here T_l and T_s are the *potential* temperatures at z_l and z_s. The temperature and specific humidity profiles within the surface layer are found through iterating (4.23) and (4.25) until the fluxes from the ground to z_s and from z_s to z_l are equal. The values for C_f and K depend on the stability of the vertical air column near the surface. They are functionally related to the Richardson Number

$$R_i = \frac{z_s \; g \; (T_s - T_g)}{T_g \; V_s^2} \tag{4.27}$$

between the surface and height z_s, and

$$R_i = \frac{(z_l - z_s) \; g \; (T_s - T_g)}{T_l \quad V_l^2} \tag{4.28}$$

between z_s and z_l. Here g is the earth's gravitational acceleration.

Under conditions of neutral stability, the drag coefficient is C_{DN}. Now when $R_i < 0$, then

$$C_f = 1.35 \; C_{DN} \left[\frac{1 - 0.81 \; R_i}{1 - 0.14 \; R_i} \right]^{1/2} \tag{4.29}$$

$$K = \frac{60 - 1.156 \times 10^7 \; \frac{T_l - T_s}{z_l - z_s}}{1 - 1.752 \times 10^4 \; \frac{T_l - T_s}{z_l - z_s}}$$

When $R_i > 0$,

$$C_f = 1.35\, C_{DN} \left[1 + 1.93\, R_i \right]^{-1}$$

$$K = \frac{60}{1 + 50\ R_i} \tag{4.30}$$

Over land

$$C_{DN} = \left[\frac{0.35}{\ln \left(\frac{z_s}{z_0} \right)} \right]^2 \tag{4.31}$$

and over ocean

$$C_{DN} = 10^{-3} \left[0.75 + 0.067\, V_s \right] \tag{4.32}$$

The roughness height z_0 over the landsurface is 0.3 meters. We take $z_s = 30$ meters over land and $z_s = 10$ meters over the ocean. In the Standard Atmosphere, the 984 millibars first atmospheric level is at $z_1 = 500$ meters.

The runoff ratio R and evapotranspiration efficiency β depend on the choice for landsurface hydrologic subgrid parameterization. In GISS (Model II),

$$\beta = s \tag{4.33}$$

and

$$R = \frac{1}{2} s \tag{4.34}$$

For the landsurface hydrologic parameterization including subgrid scale spatial

variability, the functions β and R are defined in Chapters II and III. Over the ocean, of course, $\beta = 1$.

If the time step for landsurface hydrology is made equal to the model time step (one hour), oscillations develop in the surface heat and moisture fluxes due to the dependence of C_f and K on the temperature gradient in the surface layer. We follow the GISS GCM procedure by subdividing the model time step into ten equal shorter time steps within the landsurface module in order to avoid such numerical oscillations.

3. *Basic model simulations*

The screening model is used to determine some of the major sensitivities in the landsurface hydrology parameterizations of GCMs. The model includes the important physical parameterizations (hydrologic cycle, radiation, precipitation processes) which are necessary if the critical landsurface–atmosphere feedbacks are to be represented. It, however, parameterizes the dynamic convergence of heat and moisture for an atmospheric column since GCM dynamics are not explicitly incorporated into the model.

In this section, some basic model simulations are analyzed with special focus on the convergence parameterization. The sensitivities to the exchange parameter χ are investigated in the cases of using; 1) the GISS soil hydrology (Hansen et al., 1983), and 2) the landsurface subgrid hydrology model introduced in Chapter II.

In the process of analyzing these basic model simulations, some of the outstanding differences between the two landsurface hydrology parameterizations will become evident. Thus the scope of this section extends beyond simple sensitivity analysis of the parameter χ; some of the basic characteristics of the landsurface hydrology parameterizations will also be analyzed.

Two sets of model simulations are performed using the screening model

specifications listed in Table 4.3. Simulation runs I–1 through I–8 use the landsurface hydrology parameterization introduced in Chapter II. Simulation runs I–21 through I–28 are based on the soil hydrology of the GISS GCM. In these simulations there is a zero–flux boundary condition at the bottom of the first soil layer; this represents the absence of a seasonal soil moisture reservoir in the perpetual Julian day model. In every case, the model is integrated for 250 days with a diurnal cycle. The diagnostics are collected over the last 200 days. The basic diagnostics collected for the model are mostly related to the hydrologic cycle. They are summarized in Table 4.4.

The only external forcing to the screening model is solar radiation at the top of the atmosphere. This function is deterministic for the perpetual julian day at the particular latitude. The solar radiation has a fixed diurnal period.

The screening model has twenty independent unknowns (temperature and humidity at nine atmospheric levels over both land and ocean; landsurface temperature and relative soil saturation). These variables are functionally related to one–another via the radiation, moist convection, and surface parameterizations. The two basic types of variables (temperature and humidity) are further coupled through the thermodynamics of phase–change. The dependencies are so complex and nonlinear that even though the screening model is forced by a periodic function, the model output is non–deterministic.

Examples of such model behavior is presented in Figures 4.7 and 4.8. These time–series represent the diurnally–averaged relative soil saturation for the model simulation period with specifications outlined in Table 4.3. Figure 4.7 contains the time–series of the soil saturation using GISS GCM hydrology. Figure 4.8 shows similar time–series for simulation with the subgrid hydrology parameterization.

As evident in both figures, there is a considerable amount of nondeterministic variability in the time–series. The variability appears stationary, however, around

Table 4.3: Basic screening model simulations: general specifications

Specification	Value
Radiation time step	3 hours with weights
Cloud parameter σ_c	3 °C
Julian day	182
Latitude	15 °North
Sea–surface temperature	27 °C
First soil layer depth	0.1 meters
Soil porosity (I–series runs only)	0.35
Rainfall fractional wetting (κ)	0.60

Table 4.4: Collected diagnostics

Process	Averaging	Units
Atmospheric column water balance	simulation period	[mm day^{-1}]
Soil column water balance	simulation period	[mm day^{-1}]
Surface energy balance	simulation period	[mm day^{-1}]
Diurnal cycle in landsurface latent and sensible heat flux, ground temperature	Hour of day	[W m^{-2}] and [°K]
Soil saturation and ground temperature time–series	Diurnal	[ ] and [°K]

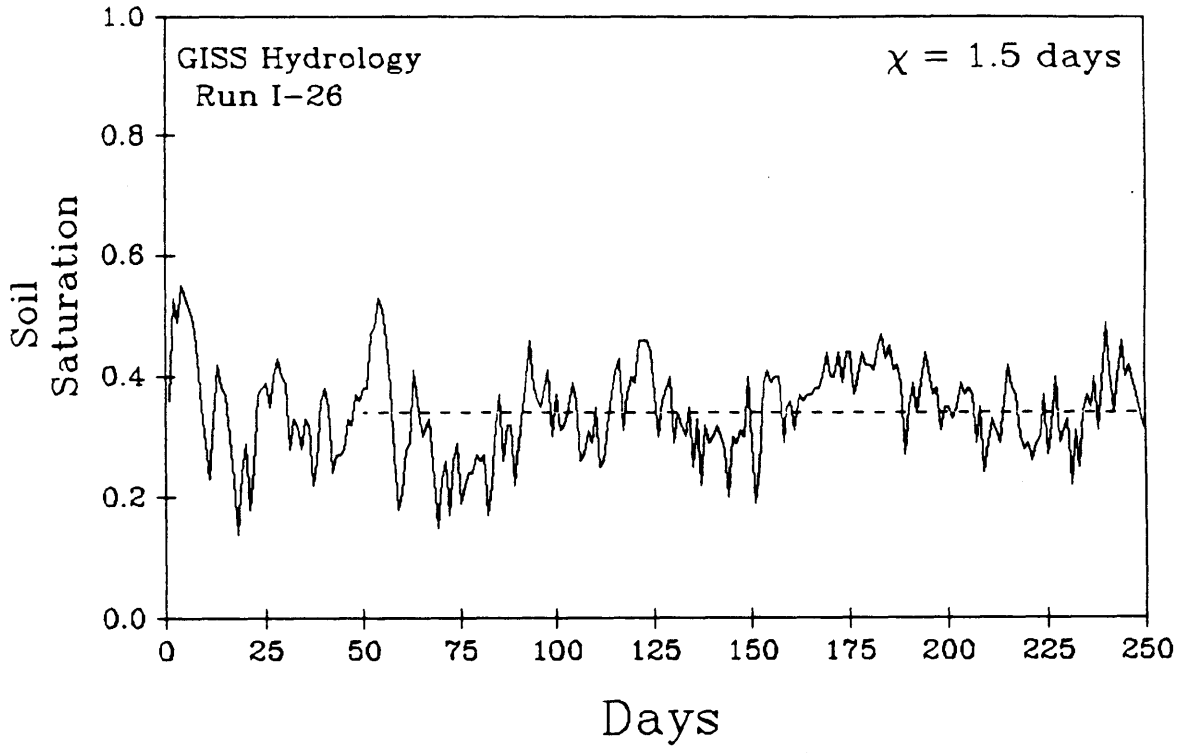

Fig. 4.7 Time series of surface relative soil saturation using the GISS soil hydrology parameterization in the screening model. The dashed line represents the mean value established over the period when diagnostics were collected [Experiment I–26]

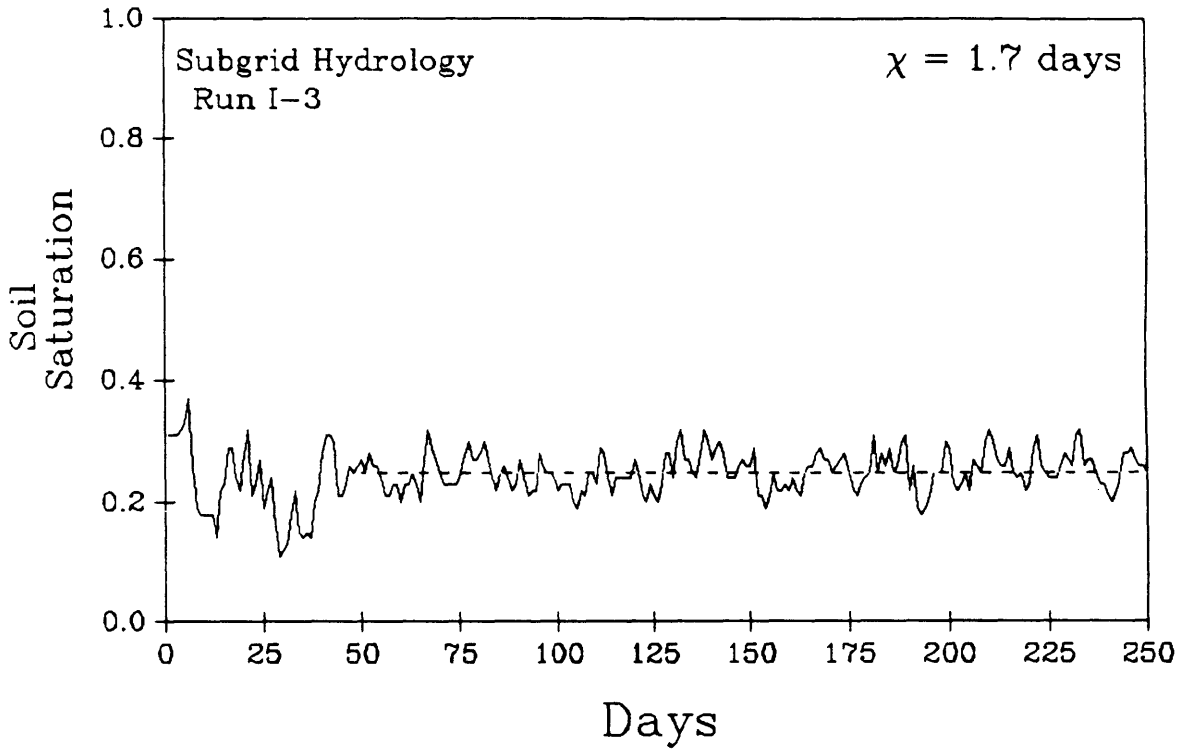

Fig. 4.8 Time series of surface relative soil saturation using the subgrid hydrology parameterization ($cv = 1$) in the screening model. The dashed line represents the mean value established over the period when diagnostics were collected [Experiment I–3]

the mean conditions established over the period when diagnostics were collected (represented by dashed lines).

A further observation, one that is crucial in the comparisons of landsurface hydrology parameterizations, is that the time–series resulting from simulations with the GISS soil hydrology is considerably more variable around its mean than the one resulting from simulations with the subgrid hydrology parameterization. A physical explanation for this behavior will be outlined later.

The basic structure of the parameterization for dynamic heat and moisture convergence consists of; 1) an ocean surface with an infinite supply of heat and moisture, and 2) an exchange of oceanic and continental airmasses. The exchange occurs at a rate controlled by the parameter χ. The rate of the dynamic convergences will determine the climate over the landsurface.

Figure 4.9 illustrates the dependence of the average rainfall rate over the landsurface on the parameter χ. In the screening model, quantitatively almost all of the precipitation is due to moist convection. As χ increases, the airmass exchange between the air columns over land and over ocean diminishes. Accordingly the rainfall rate over the landsurface decreases since, at high values of χ, the oceanic source of moisture is virtually cut off from the landsurface air column. Under these circumstances, the moisture in the earth–atmosphere system in the landsurface half of the screening model is moved through repeated cycles of surface evaporation, moist convection from the lowermost atmospheric level, and precipitation. For both the GISS soil hydrology and the subgrid hydrology, the rainfall rate decreases for high values of χ.

As the parameter χ is lowered, the precipitation over the landsurface is increased since greater moisture exchange may occur with the oceanic moisture source. Finally at χ near 1 day, a transition occurs. For still smaller χ, the mixing between the ocean and landsurface air columns is virtually complete (or at least on

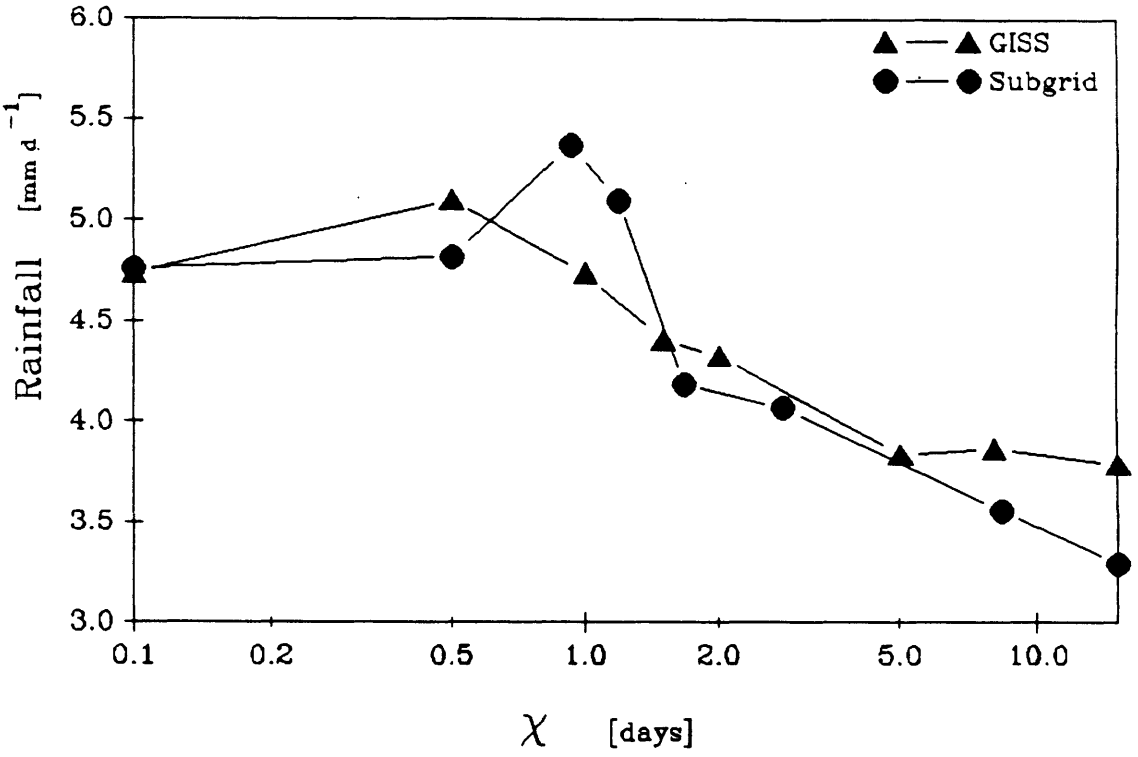

Fig. 4.9 Dependence of the landsurface rainfall rate on the screening model parameter χ for both the GISS soil hydrology and subgrid hydrology ($cv = 1$) parameterizations [Experiments I–1 to I–28]

time scales less than precipitation formation processes). The rainfall rate over the landsurface does not increase appreciably when the airmasses mix so thoroughly at low values of χ.

The rainfall rate dependence on χ is similar using either the GISS soil hydrology or the subgrid hydrology parameterization (Figure 4.9). In the latter case, however, there is a peak in the rainfall rate near the transitional $\chi = 1$ day. A physical explanation for the presence of this anomaly.

In equilibrium, the rate of atmospheric moisture convergence (i.e., – atmospheric runoff) must equal the soil runoff rate. Figure 4.10 illustrates the relationship of the atmospheric or soil runoff to the parameter χ. Again, as in Figure 4.9, there is a transitional value of χ below which both neither rainfall nor runoff rates change due to the virtually complete mixing of oceanic and continental airmasses.

The most striking feature of Figure 4.10, however, is the difference between the simulation series using either the GISS hydrology or the subgrid hydrology parameterization. The latter parameterization consistently produces greater surface runoff when compared with the GISS soil hydrology model. The removal of moisture from the soil system by surface runoff will result in less moisture storage in the earth–atmosphere system; the atmospheric convergence of moisture will increase correspondingly since the atmospheric column over the landsurface and these fractions of it that are lost during dynamic exchange contain less moisture.

Figure 4.11 represents the relationship between equilibrium relative soil saturation and the rainfall rate using, in separate cases, both the GISS soil hydrology and the subgrid hydrology parameterization. As it is clearly evident in the case of the GISS soil hydrology, the relative soil saturation is linearly proportional to the incident rainfall (see Appendix E). A similar, though considerably weaker relation exists in the case of simulations using subgrid

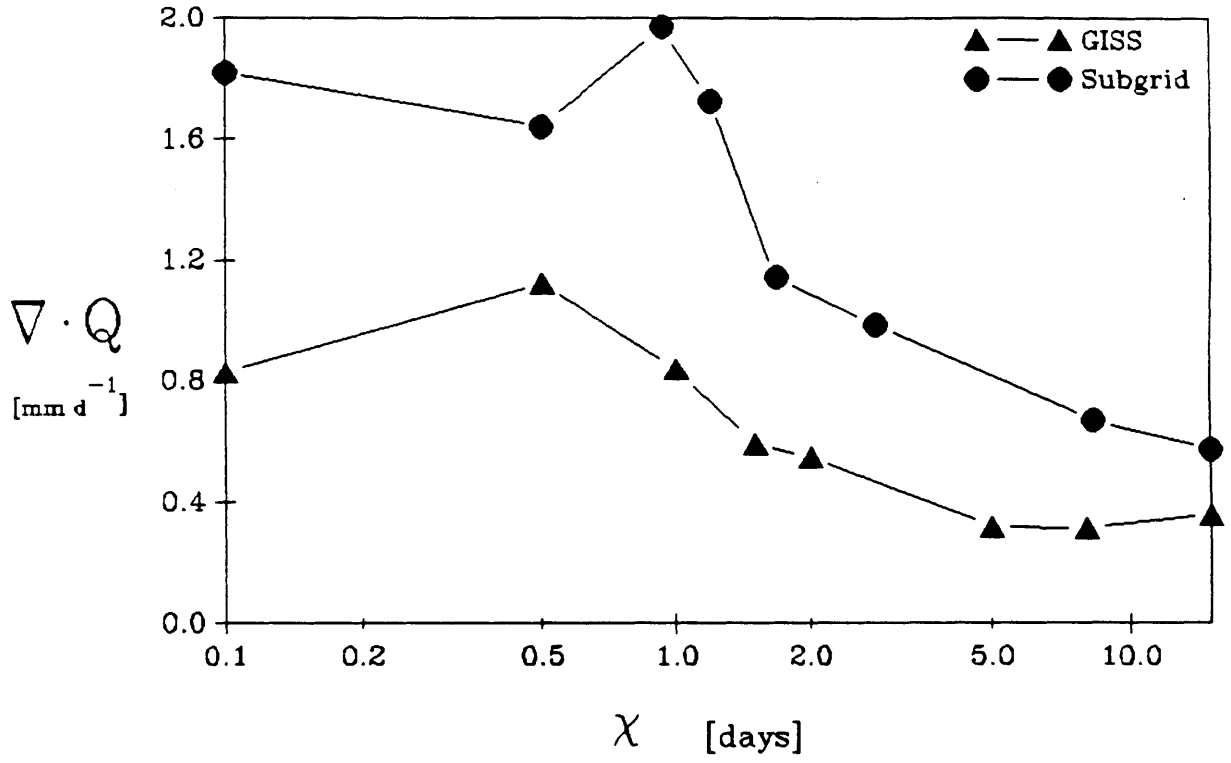

Fig. 4.10 Dependence of the atmospheric moisture exchange over the landsurface (or equivalently the surface runoff) on the screening model parameter χ for both the GISS soil hydrology and subgrid hydrology ($cv = 1$) parameterizations [Experiments I–1 to I–28]

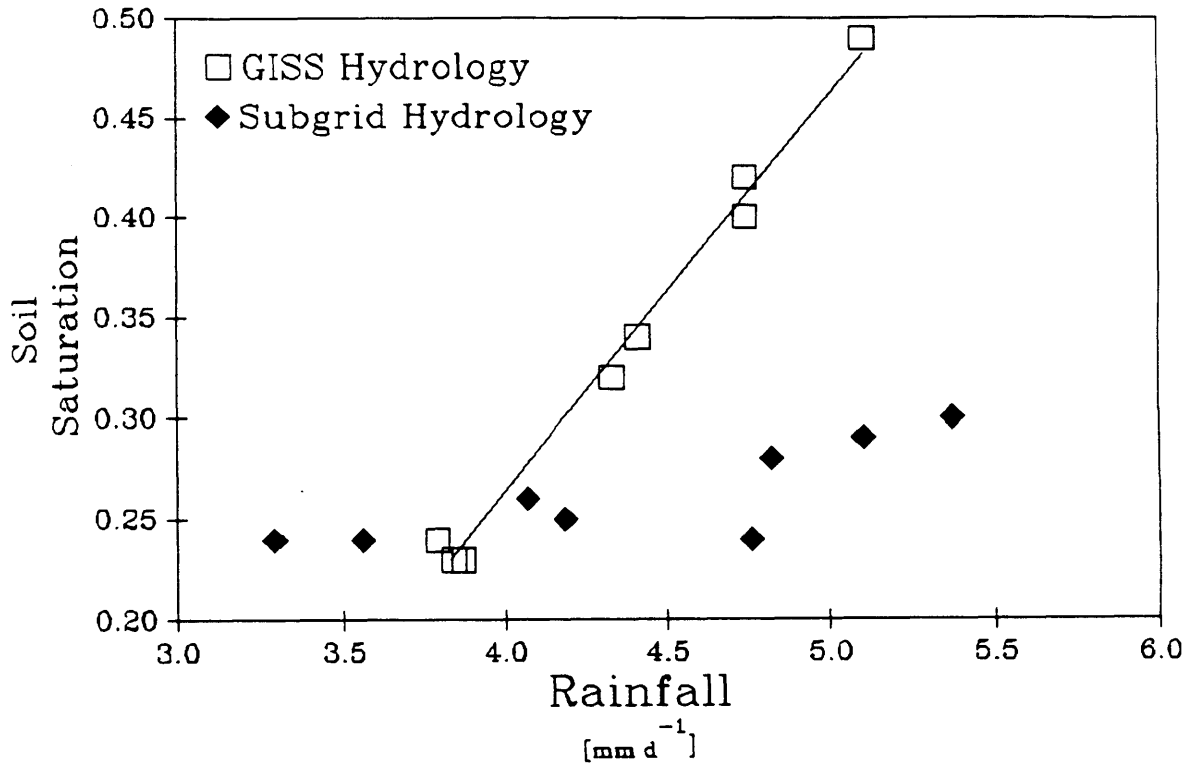

Fig. 4.11 Dependence of the equilibrium surface relative soil saturation on the mean landsurface rainfall rate for both the GISS soil hydrology and subgrid hydrology ($cv = 1$) parameterizations [Experiments I–1 to I–28]

hydrology parameterization. The physical explanation for the behavior is also deferred to later.

Now, however, we will enumerate all the explanations that have been posed but left unanswered in this section. They concern; 1) the significantly lower variance about the mean relative soil saturation in the case of the subgrid hydrology parameterization when compared to the GISS soil hydrology (Figures 4.7 and 4.8) , 2) the peak in the rainfall rate versus χ plot (Figure 4.9) when using the subgrid hydrology paramertization, and finally 3) the weaker dependence of soil saturation on the relative rainfall rate when using subgrid hydrology parameterization as opposed to GISS soil hydrology (Figure 4.11).

Table 4.5 is set up to address these issues. Some diagnostics from the eight experiments using the subgrid hydrology parameterization (Run I–1 through I–8) are tabulated under columns headed by the value of χ used in the simulation.

With lower values of χ, the net moisture convergence ($\nabla \cdot Q$) and mean rainfall rate increase until their peak near χ = 1 day. These diagnostics steadily decrease for χ values below this threshold and reach a plateau for still lower χ values (indicating thorough atmospheric mixing). In the fourth and fifth row of Table 4.5 we also notice that the rainfall variability in time (daily data) is significantly increased for lower values of χ. The rainfall variance increases nearly five–fold over this range of χ. At low values of χ, however, the mean rainfall rate is rising as well; the dimensionless coefficient of variation is thus the statistic that truly measures the increased variability in rainfall at lower values of χ.

There is greater moisture convergence and mean rainfall for lower values of χ down to the limit below which the sensitivity to χ vanishes due to virtually complete air mass mixing. At the transitional χ level, however, there is a local peak in the mean rainfall rate–χ relationship.

The physical explanation for the presence of such an anomaly becomes evident

Table 4.5: Screening model with subgrid hydrology: Role of parameter χ

	Simulation Runs							
	I–6	I–7	I–5	I–4	I–3	I–2	I–1	I–8
χ [days]	0.1	0.5	0.9	1.2	1.7	2.8	8.3	15.0
Moisture Exch. [mm d^{-1}]	1.82	1.64	1.97	1.73	1.14	0.99	0.67	0.58
Mean Rainfall [mm d^{-1}]	4.76	4.82	5.37	5.10	4.19	4.07	3.56	3.29
Rainfall Var. [mm^2 d^{-2}]	24.6	21.0	22.3	19.0	13.6	10.8	7.1	4.6
Rainfall Temporal CV	1.04	0.95	0.88	0.85	0.88	0.81	0.75	0.65
Dry Heat Exch. [W m^{-2}]	–13.8	–9.5	–6.7	–1.6	5.1	8.5	14.1	16.8
Total Heat Exch. [W m^{-2}]	38.9	38.0	50.3	48.3	38.1	37.1	33.5	33.5
Mean soil Saturation	0.24	0.28	0.30	0.29	0.25	0.26	0.24	0.24
Horton Runoff Ratio	0.36	0.32	0.34	0.32	0.26	0.23	0.18	0.17

when we compare the heat convergences for various χ values. The atmospheric dry heat convergence over the landsurface monotonically decreases for lower values of χ. It even reverses sign between χ = 1.2 to 1.7 days. But much of the total heat convergence (dry heat + latent heat) is due to the latent heat associated with the moisture convergence.

We had mentioned that the atmospheric moisture convergence must be equal to the surface runoff when the model is in equilibrium. The atmospheric convergence is in terms of water vapor but the surface runoff is liquid water. The latent heat of phase change in converting the atmospheric convergence of water vapor to surface runoff of liquid water is thus a major heat input to the atmospheric column.

When we account for this source of heat convergence and add it to the dry heat convergence, we notice that there is a direct correspondence between this total heat convergence and both the rainfall mean and variance. (Table 4.5). They increase with lower values of χ; peak at χ near 1 day, and plateau for even lower χ.

The total heat exchange drives the entire moist convective process. With greater total heat input, stronger convection is possible resulting in both larger mean rainfall rates and especially greater rainfall temporal variability.

The monotonic decrease of the dry heat convergence with lower χ values, combined with the particular moisture convergence–χ relationship results in a strong peak in the total heat convergence around χ = 1 day. The moist convection is strongest at this point and both the rainfall mean and variability, correspondingly, increase locally. There is, of course, a feedback and a circular chain of events. Greater rainfall intensity produces more runoff; more runoff indicates greater moisture convergence, and this in turn causes more latent heat convergence and greater rainfall intensity.

A general observation at this point is that the surface runoff produced in

climate models is *not* a residual of model simulation. The surface runoff parameterization has a significant impact on all branches of the hydrologic cycle and ultimately the moist thermodynamics of the atmosphere.

This has been the physical explanation for the rainfall–χ relationship exhibited in Figure 4.9. We have yet to explain; 1) the relatively lower temporal variability in mean soil saturation , and 2) the relatively weak soil saturation–rainfall rate relationship when using the subgrid hydrology parameterization as opposed to the GISS soil hydrology. The two issues are, however, linked; they are further related to the rainfall variability at lower values of χ.

A peculiar (and desirable) characteristic of the landsurface subgrid parameterization introduced in Chapter II is the sensitivity of the runoff ratio and evapotranspiration efficiency functions to their forcing parameter (rainfall intensity and potential evaporation ; see Appendix E). In the case of surface runoff, for example, as the rainfall intensity increases, a greater fraction of the incident rainfall becomes runoff since Horton runoff is the excess of the rainfall intensity over the local infiltration rate (See Figures 2.2 and 2.3). This sensitivity is totally lacking in simple GCM soil hydrology parameterizations where the runoff ratio is simply a linear function of the relative soil saturation.

The runoff volume is thus a linear function of the rainfall volume in the GISS soil hydrology (Equation E.7). The same relationship is highly nonlinear in the case of the subgrid hydrology parameterization in Chapter II (Equation 2.15).

In Figure 4.11 the soil saturation, when using the GISS soil hydrology, is strongly dependent on the rainfall rate. When simulating with the subgrid hydrology parameterization, however, the relationship is weak and the relative soil saturation does not increase as appreciably with higher mean rainfall rates. This may be explained by taking into account the shifts in the variability of rainfall as

the mean rainfall is increased in the screening model . Increased rainfall variability at lower χ values results in a greater fraction of the increased mean rainfall becoming Horton runoff (see Table 4.5 ; last row). Only 17% of the rainfall becomes Horton runoff when $\chi = 15$ days while up to 36% is lost to this mechanism when $\chi = 0.1$ days. The disproportionate increase in surface runoff with higher mean rainfall rates results in the slower response of the mean relative soil saturation for those model climates characterized by greater mean and more variable rainfall. For smaller values of fractional wetting (κ), there will be even larger rates of local rainfall intensity and thus more surface runoff (see Figure 2.3).

This explanation addresses the behavior of the curves in Figure 4.11. The disparate amounts of temporal variability in the model simulations using GISS soil hydrology and subgrid hydrology parameterization (Figures 4.7 and 4.8) may be explained using the same reasoning.

For any rainfall event, the GISS hydrology parameterization partitions the incident rainfall into runoff and storage based simply on the governing relative soil saturation. The partitioning is totally independent of the rainfall intensity. Now when a particularly intense rainfall event occurs, the GISS hydrology parameterization would add a large volume of water to soil storage in response to the event. The relative soil saturation will thus sharply rise above its longterm mean. The soil moisture then, on the average, undergoes depletion to below the mean value until the next rainfall event occurs. The net result is a highly variable soil saturation time–series.

The subgrid hydrology parameterization would, however, partition a larger fraction of the more intense rainfall events into surface runoff. It would, moreover, add greater fractions of the less intense events to soil storage. The net result is a less marked deviations away from the equilibrium relative soil saturation. Statistically, this translates to smaller variability in the soil saturation time–series.

This is, of course, a desirable behavior for climate models that need better physical realism in their soil hydrology formulations and furthermore require that the parameterization guide the model to an equilibrium with less transience.

In the next section, we narrow our focus to simulation experiments with the screening model using the landsurface hydrology parameterization introduced in Chapter II. The basic sensitivities of this model to the vegetative cover, soil type, spatial variability, energy–balance feedbacks, and multiple soil layering will be analyzed (see Table 4.6). In these experiments we will generally stay with the specifications outlined in Table 4.3; the parameter χ will be fixed at $1\frac{2}{3}$ days. We will, however, begin all simulation with complete soil saturation in order to observe the time scales associated with the soil moisture depletion process. Accordingly, we give the model 100 days (instead of 50 days) to reach the equilibrium when diagnostics collection begins.

4. *Sensitivity of landsurface hydrology parameterization including subgrid scale spatial variability*

a. Bare soil

The J1 simulation experiment soil hydrology is characterized by light soil and cv=1. This experiment serves as the base–line for comparison when the soil hydrology conditions are altered in other simulations. The time–series of the daily–averaged relative soil saturations for the simulation period is plotted in Figure 4.12. Over the last 150 days when diagnostics are collected, the mean soil saturation averages 0.23 (specified by dashed–line on the figure). The soil is initially saturated and it decays to its equilibrium value in about 20 to 40 diurnal cycles. Figure 4.13
illustrates the vertically–integrated atmospheric water balance for the land and ocean halves of the screening model. The values of the fluxes are in mm day^{-1}

Table 4.6 **List of sensitivity experiments with the hydrologic parameterization including subgrid scale spatial variability**

Run	Cover Type	Soil Type	cv	Number of Soil Layers
J1	Bare Soil	Light	1	1
J3	Bare Soil	Medium	1	1
J8	Bare Soil	Heavy	1	1
J2	Vegetation	Light	1	1
J5	Bare Soil	Light	1/2	1
J9	Bare Soil	Heavy	1/2	1
J4	Bare Soil	Light	1/4	1
J7	Bare Soil	Heavy	1/4	1
J6	Bare Soil with Energy–Correction	Light	1	1
M1	Bare Soil	Light	1	3
M2	Bare Soil	Light	1	5
M4	Bare Soil	Heavy	1	5

Definitions:

	% Sand	% Silt	% Clay
Light Soil	75	20	5
Medium Soil	30	35	35
Heavy Soil	15	15	70

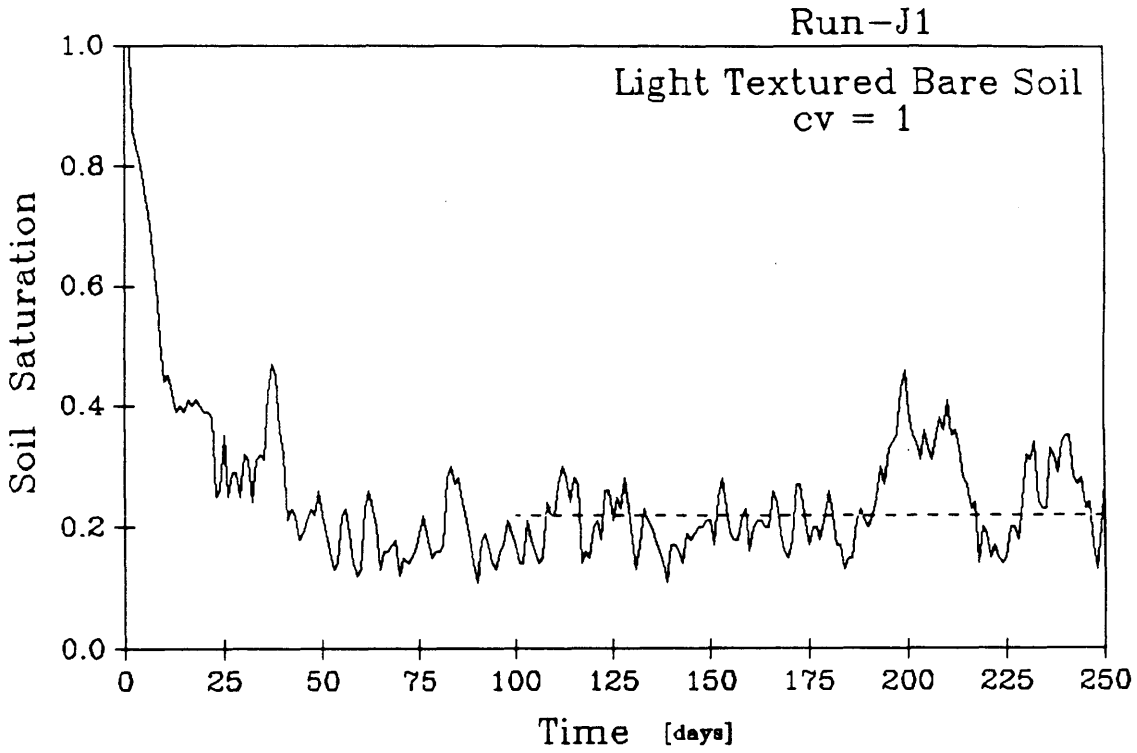

Fig. 4.12 Time series of the relative soil saturation for the screening model with subgrid hydrology parameterization ($cv = 1$). Initially the soil is saturated. The dashed line represents the mean value established over the period when diagnostics were collected [Experiment J–1]

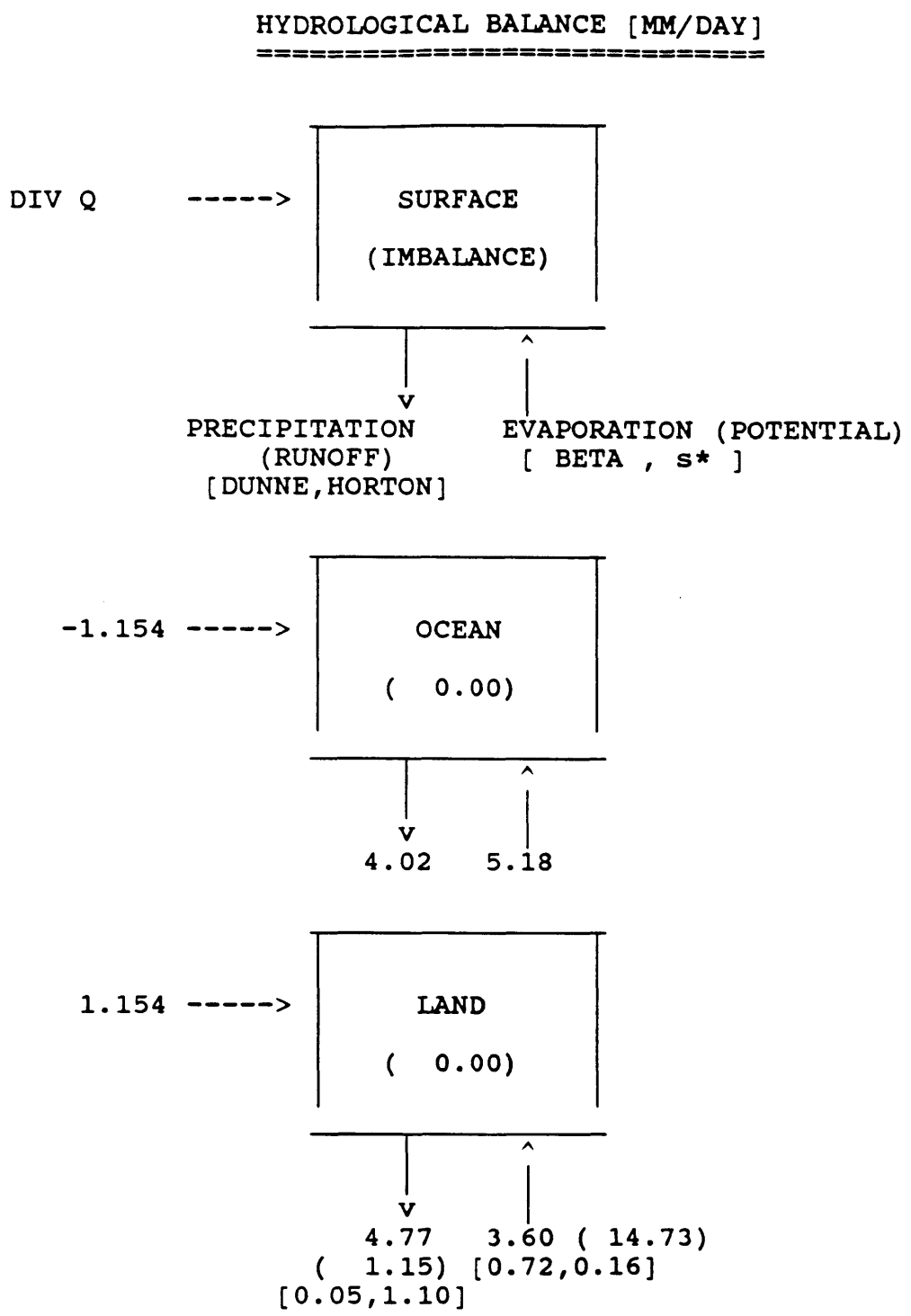

Fig. 4.13 The averaged water balance components (in mm day^{-1}) for the atmospheric air columns over land and ocean [Experiment J–1]

averaged over the last 150 days of simulation. There is a net convergence of moisture over the landsurface atmospheric column (at a rate of 1.15 mm day^{-1}). The ocean surface is a net supplier of moisture for the enclosed system ($P - E = 5.18 - 4.02$). The precipitation rate over the landsurface is 4.77 mm day^{-1}. About 24% of the incident precipitation becomes surface runoff (4.3% by the Dunne mechanism and 95.7% by the Horton mechanism). The potential evaporation over the landsurface is over one centimeter per day (14.73 mm day^{-1}). The average evaporation efficiency ("BETA" in Figure 4.13) is about 0.72; the transitional relative soil saturation s* is estimated as 0.16 on the average for this soil type and e_P forcing.

Figure 4.14 represents the longterm and diurnally–averaged surface energy balance over the land and ocean halves of the screening model. Over land the net incoming radiation is about 132 W m^{-2} ($214.6 - 82.6 = 131.8$ Wm^{-2}). The average latent heat flux is 104 W m^{-2}. The sensible heat flux is nearly a quarter of the latent heat flux in magnitude. The net ground heat flux is nearly zero (0.3 W m^{-2}) since the model is in a perpetual julian day and this diagnostic is averaged over the diurnal cycle. Over the ocean, the net radiation at the surface is about 132 W m^{-2}. The latent heat flux is rather large, averaging near 150 W m^{-2}. The sensible heat flux, in this case, is only about 5.5% of the latent heat flux; Q_h=8.2 W m^{-2}. With the sea surface temperature (SST) specified as constant, there is an implied oceanic heat flux and storage in the ocean surface energy balance. In this case, for SST=27 ^{0}C, the implied energy balance term $S_o+\nabla F_o$ is nearly 26.1 W m^{-2} on the average. Between the ocean and land halves of the screening model, there is also a dry atmospheric heat flux due to the exchange process. In this case, 6.1 W m^{-2} of energy is supplied by the ocean half of the model to the atmospheric column overlying the landsurface.

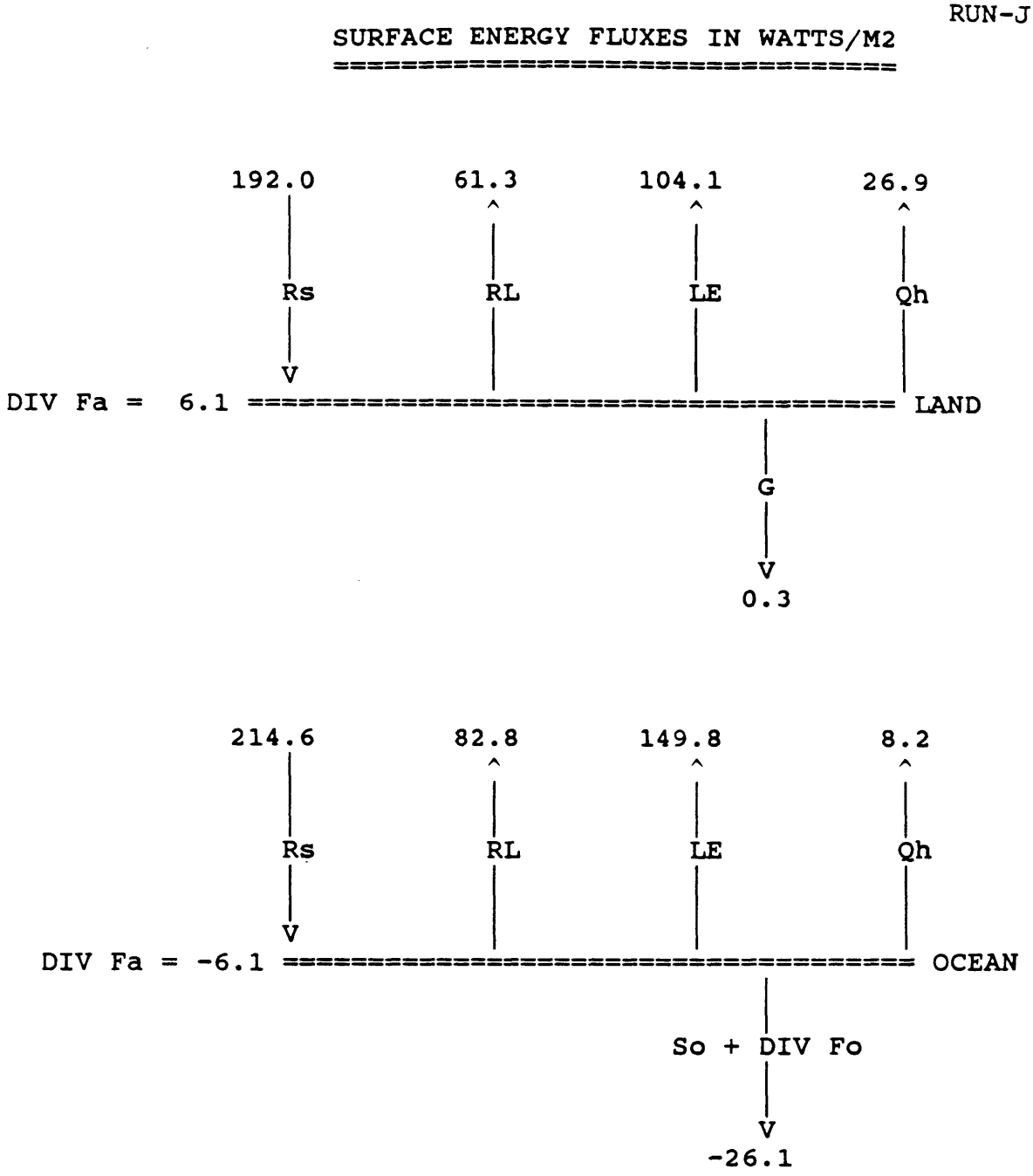

Fig. 4.14 The averaged energy balance components (in W m^{-2}) for the atmospheric air columns over land and ocean [Experiment J–1]

b. Vegetated surface

As evident in the plots of the evaporation and transpiration efficiency functions (β_s and β_v) versus the soil–climate parameter δ in Chapter II, plants are capable of removing soil water storage more efficiently than bare soil desorption. In simulation experiment J2, a complete vegetation cover is prescribed to the landsurface. The wilting matric suction is set at Ψ_w=–15 bars.

Figure 4.15 contains the relative soil saturation time–series for the vegetated landsurface simulation experiment. Since the transpiration rate is higher when compared with the bare soil desorption rate, the soil moisture decay from complete saturation to its equilibrium value takes only 10 to 20 days (as opposed to 20 to 40 days in experiment J1). Furthermore, the equilibrium relative soil saturation is 0.19; a value lower than the bare soil case.

c. Effects of soil type

Simulations J1, J3, and J8 are all bare soil experiments with identical *cv*'s, soil depths, and other parameters. They are, however, characterized by different soil types (light, medium, and heavy respectively; definitions in Table 4.6). The soil type seriously affects the Horton component of the surface runoff since both the soil infiltrability and soil capillarity are functions of soil texture. More importantly, however, the soil type strongly influences the desorption rate. Furthermore, the transitional relative soil saturation s* depends on soil type and thus the evapotranspiration efficiency is modified given different soil textures.

Figure 4.16 and 4.17 contain the time–series for the relative soil saturation with medium and heavy soils respectively. These time–series are to be compared with that in Figure 4.12 where a light soil is prescribed.

The time scale associated with the decay of soil moisture from its initial saturation value to the final equilibrium value is dependent on soil type. The

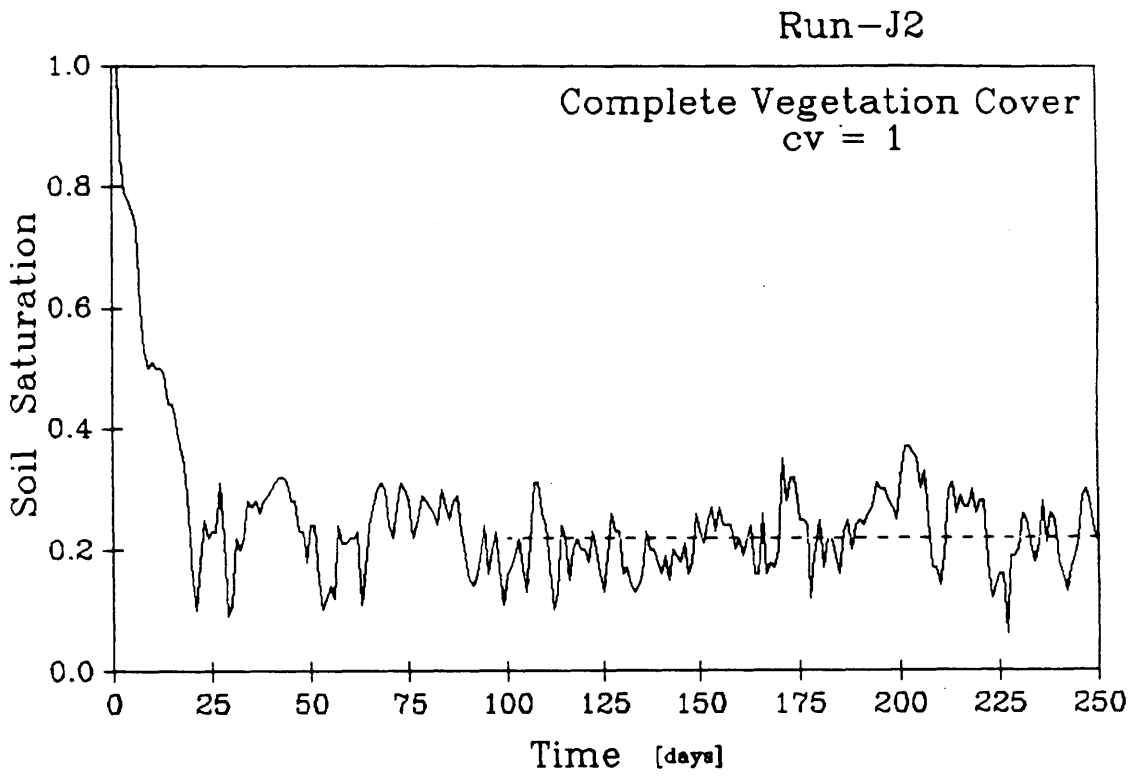

Fig. 4.15 Time series of surface relative soil saturation with subgrid hydrology parameterization, $cv = 1$, light textured soil, and vegetal transpiration ($\Psi_w = -15$ bars).The dashed line represents the mean value established over the period when diagnostics were collected [Experiment J–2]

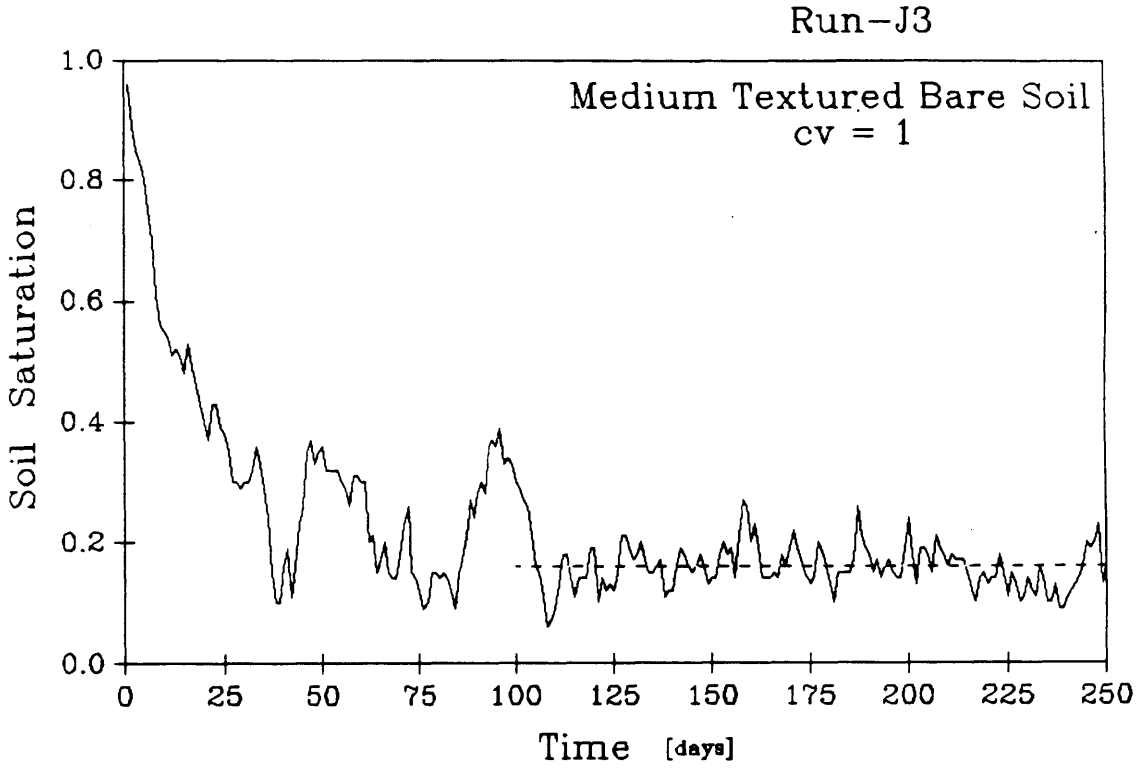

Fig. 4.16 Time series of surface relative soil saturation with subgrid hydrology parameterization, $cv = 1$, and medium textured bare soil. The dashed line represents the mean value established over the period when diagnostics were collected [Experiment J–3]

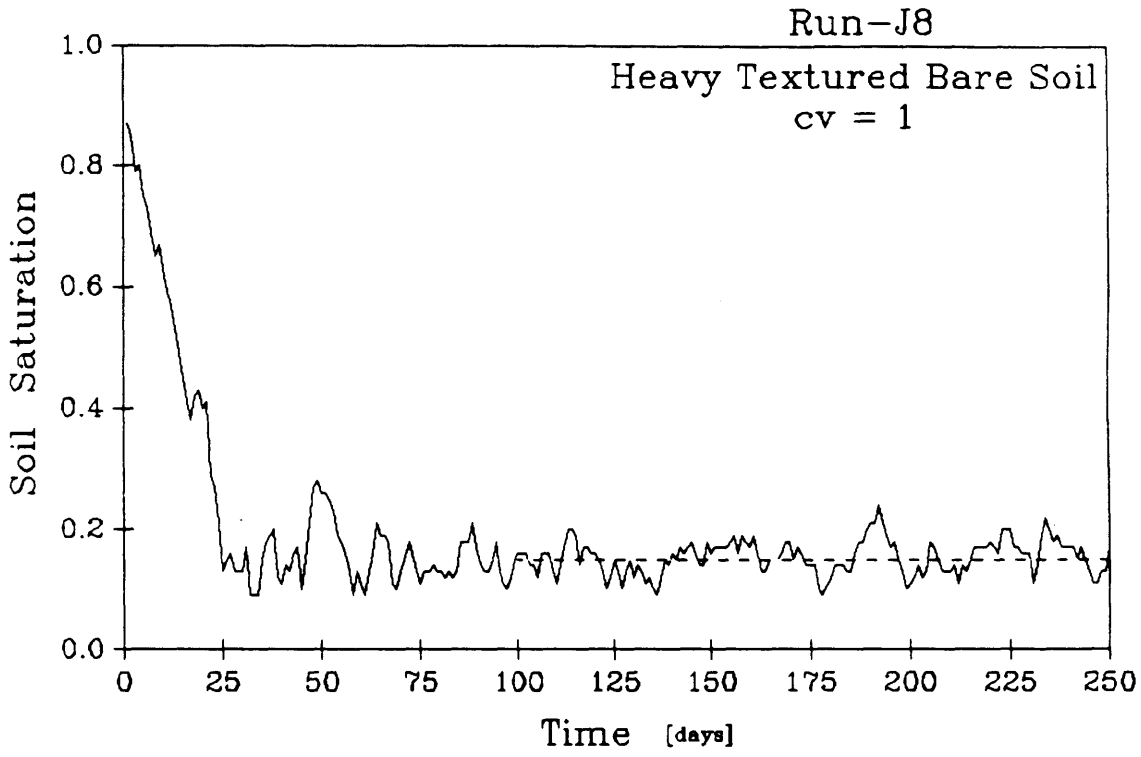

Fig. 4.17 Time series of surface relative soil saturation with subgrid hydrology parameterization, $cv = 1$, and heavy textured bare soil. The dashed line represents the mean value established over the period when diagnostics were collected [Experiment J–8]

lighter soil (Figure 4.12) has a 20–40 days time scale associated with this decay. The heavier soils (Figures 4.16 and 4.17) have generally shorter time scales; the heavy soil case decays from initial saturation to the final equilibrium value in less than 20 days (Figure 4.17). The equilibrium relative soil saturations for the light, medium, and heavy soil textures are 0.23, 0.16, and 0.15 respectively. The shorter decay time scales and lower equilibrium soil moisture contents associated with heavier soils is mostly related to the greater (de)sorptivity associated with soils of finer texture.

d. Effects of degree of spatial variability

The coefficient of variation (cv) for the point distribution of surface relative soil saturation over the grid area is of central significance to the hydrology parameterization including subgrid scale spatial variability. Its value depends on estimates of mean topography and the dimensions of GCM grids. In this section, the sensitivity of the screening model hydrology to the magnitude of cv is determined by simulation.

The time series of diurnally–averaged surface relative soil saturation for the case cv=1 is presented in Figure 4.12. Similar time series but with cv=$\frac{1}{2}$ and =$\frac{1}{4}$ are plotted in Figures 4.18 and 4.19. For these three cases, the soil storage is characterized by light soil and bare surface. As evident in these time series, the temporal variability and the equilibrium relative soil saturations are not significantly different for the various values of cv. In the top panel of Table 4.7 various water balance characteristics for these three experiments (different cv's and light soil) are presented. For this soil type, regardless of cv, the relative soil saturation is around 0.22. The runoff rate is consistently near 25% of the incident precipitation. The evaporation rate and its limiting potential value are also similar

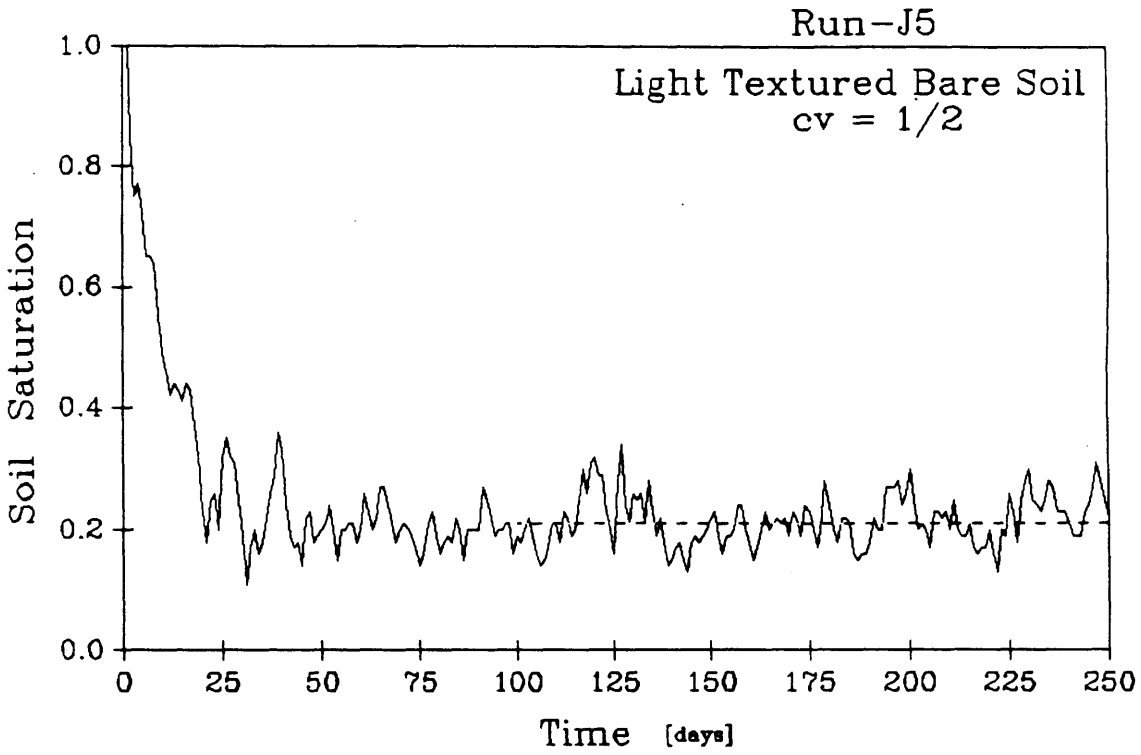

Fig. 4.18 Time series of surface relative soil saturation with subgrid hydrology parameterization, $cv = 1/2$, and light textured bare soil. The dashed line represents the mean value established over the period when diagnostics were collected [Experiment J–5]

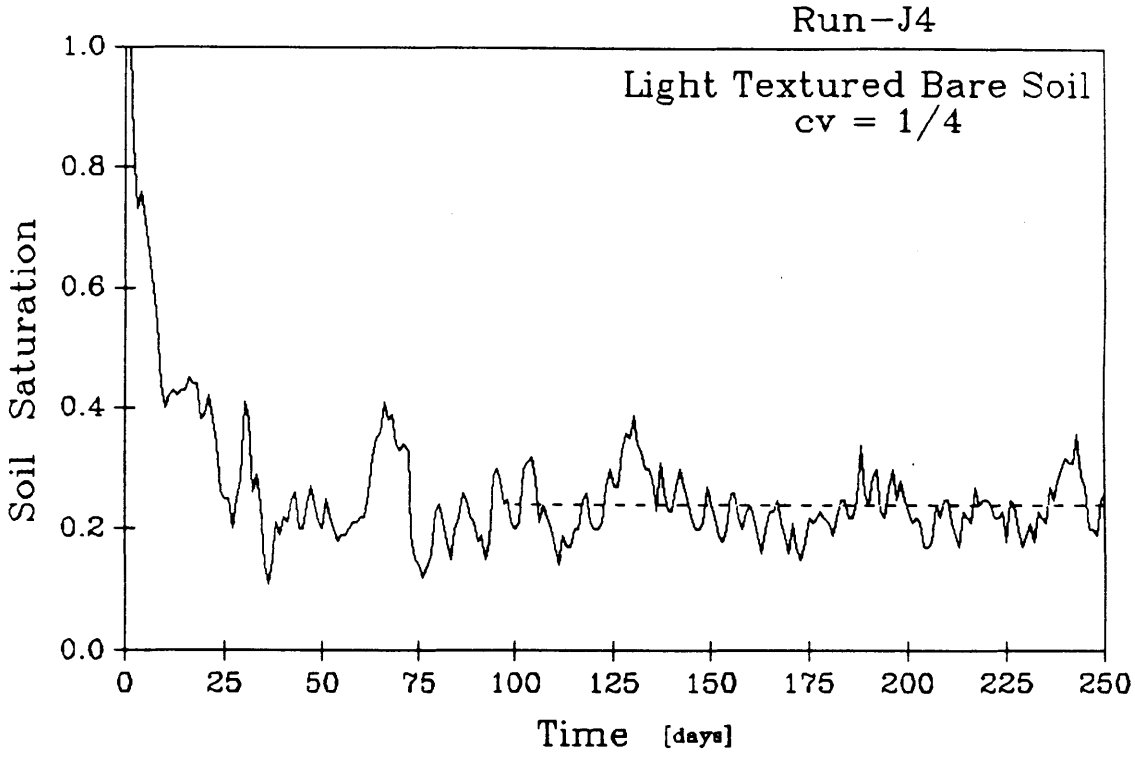

Fig. 4.19 Time series of surface relative soil saturation with subgrid hydrology parameterization, $cv = 1/4$, and light textured bare soil. The dashed line represents the mean value established over the period when diagnostics were collected [Experiment J–4]

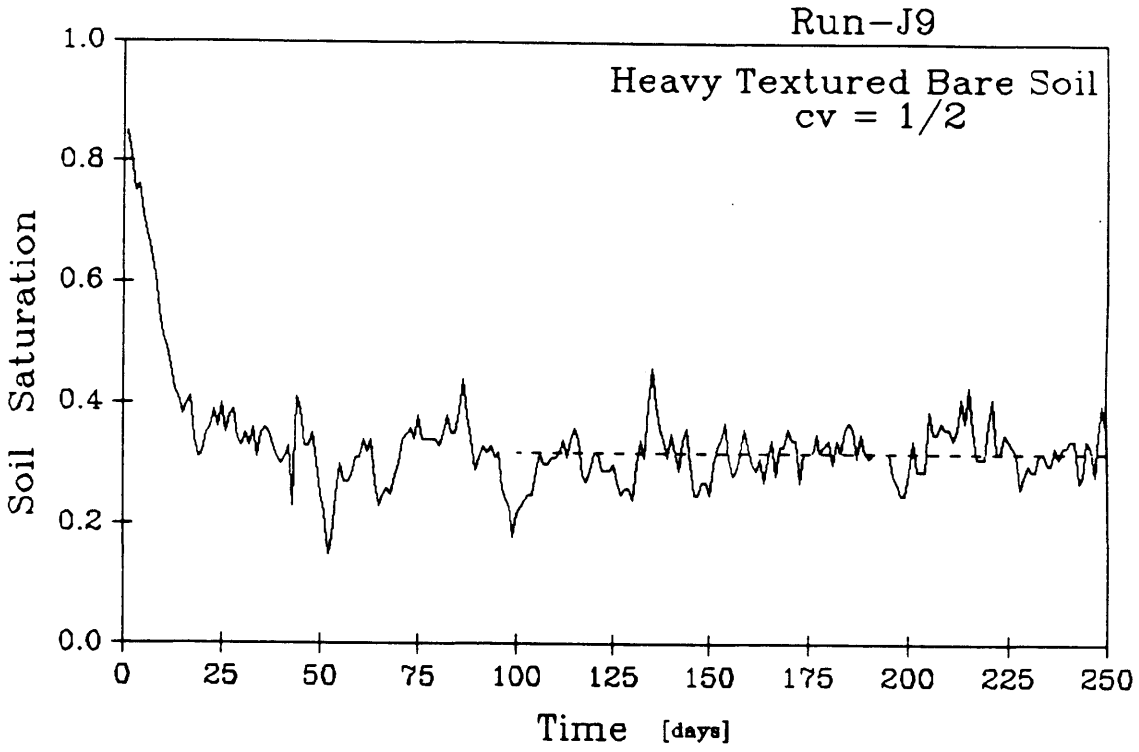

Fig. 4.20 Time series of surface relative soil saturation with subgrid hydrology parameterization, $cv = 1/2$, and heavy textured bare soil. The dashed line represents the mean value established over the period when diagnostics were collected [Experiment J–9]

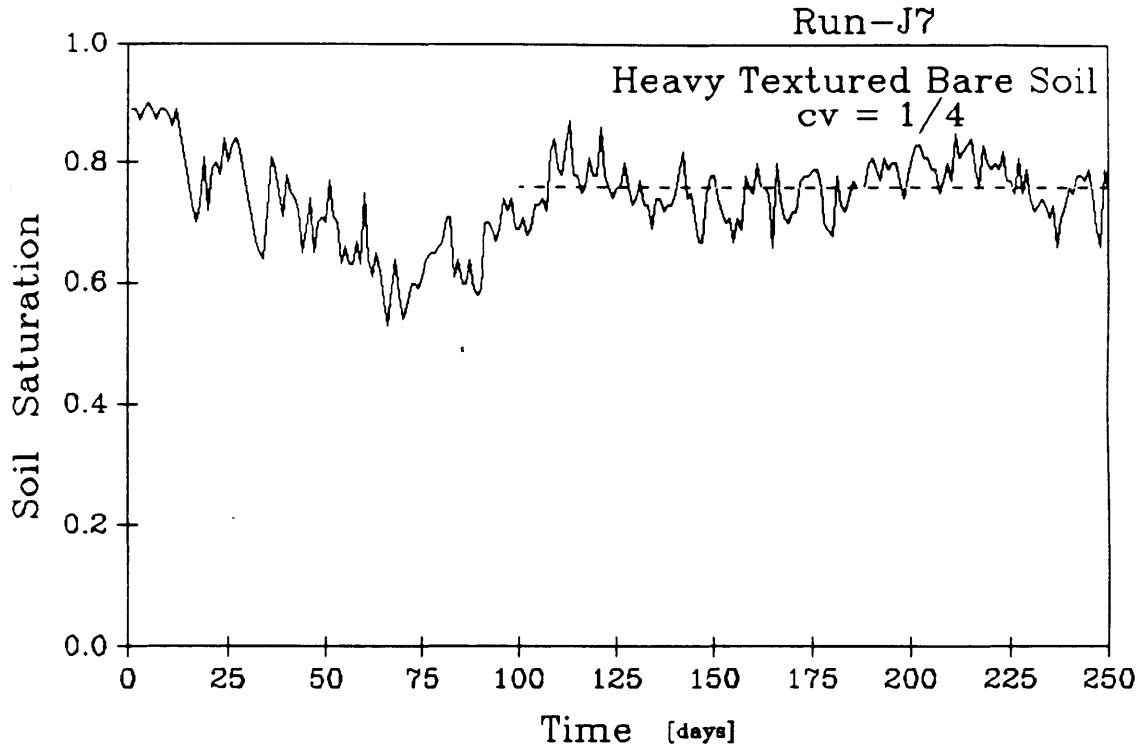

Fig. 4.21 Time series of surface relative soil saturation with subgrid hydrology parameterization, $cv = 1/4$, and heavy textured bare soil. The dashed line represents the mean value established over the period when diagnostics were collected [Experiment J–7]

in all three cases.

For a different soil type, however, the sensitivity to cv is radically different. Time series of surface relative soil saturation for cv=1, =$\frac{1}{2}$, and =$\frac{1}{4}$ with heavy soil composition are illustrated in Figures 4.17, 4.20, and 4.21. The equilibrium relative soil saturation is highly sensitive to cv for this soil type. As evident in the bottom panel of Table 4.7, the equilibrium relative soil saturation for heavy soil and cv=1 is 0.15. For cv=$\frac{1}{2}$ and cv=$\frac{1}{4}$, the same diagnostics take values of 0.32 and 0.76. The result is a fundamental shift in the hydroclimatology established in the screening model.

When cv=1 for this soil type, the surface runoff rate is 1.03 mm day^{-1} or 23.3% of the incident precipitation. Reading from Table 4.7, the surface runoff rate decreases to 0.53 mm day^{-1} (or 11.3%) and 0.47 mm day^{-1} (or 10.0%) for cv=$\frac{1}{2}$ and =$\frac{1}{4}$. The evaporation rate is also affected by the changes in cv and the corresponding shifts in the equilibrium relative soil saturation. For cv=1, $\frac{1}{2}$, and $\frac{1}{4}$ the surface evaporation rate increases from 3.37, to 4.14 and 4.17 mm day^{-1}. The lower relative soil saturations associated with higher cv's, however, have the effect of reducing the evaporation efficiency (evaporation normalized by its limiting potential value). The drier surfaces thus lead to considerably higher potential evaporation rates. In Table 4.7, the potential evaporation rate for cv=1 and heavy soil is 18.34 mm day^{-1}; only 18.4% of this evaporative demand is met by bare soil evaporation. When the value of cv=$\frac{1}{4}$ and the relative soil saturation is as high as 0.76, then the potential evaporation rate is only 4.17 mm day^{-1}. The bare soil under these conditions completely meets the evaporative demand and thus the actual evaporation rate is 100% of its potential value.

Infiltration and exfiltration processes are functions of the surface relative soil saturation. This sensitivity is, however, strongly dependent on soil type. Heavier soils, for example, experience considerably higher changes in matric suction and

Table 4.7: **Water balance components for various values of *cv* and soil type** [mm day^{-1}]

Soil Type	*cv*	E[s]	Rainfall rate	Runoff rate	Runoff % of rainfall	Evap. rate	Potential Evapor.
Light	1	0.23	4.77	1.15	24.1	3.60	14.73
	$\frac{1}{2}$	0.22	4.70	1.16	24.7	3.55	14.49
	$\frac{1}{4}$	0.24	4.77	1.28	26.8	3.48	15.94
Heavy	1	0.15	4.43	1.03	23.3	3.37	18.34
	$\frac{1}{2}$	0.32	4.70	0.53	11.3	4.14	5.61
	$\frac{1}{4}$	0.76	4.69	0.47	10.0	4.17	4.17

diffusivity for similar shifts in relative soil saturation when compared with lighter soils. Thus the prescribed spatial variability in relative soil saturation has a different impact on the surface water balance components depending on the soil type.

e. Effects of subgrid energy balance correction

In Chapter III it was postulated that the deficit of the actual surface evaporation with respect to its limiting potential value may result in an excess amount of energy that goes towards increasing the atmospheric evaporative demand. This feedback was incorporated into the hydrology parameterization via a simple procedure.

For the case of cv=1, the screening model resultant time–series of relative soil saturation with energy–correction is presented in Figure 4.23. Compared with Figure 4.12, which does not contain the energy–correction procedure, it is evident that the equilibrium relative soil saturation is affected. The long–term mean relative soil saturation is 0.17 and 0.23 in the case of bare soil evaporation functions with and without the energy–correction.

The applicability of this correction depends on a thorough examination of how exactly e_p (potential evaporation) is computed in particular GCMs. For the screening model used here, the surface moisture and energy fluxes are dynamically estimated every 0.1 hours. For this reason, the temporal energy feedback in the surface hydro–thermal balance is already included. Important spatial heterogeneities in the surface conditions are, however, not incorporated in estimating e_p. The energy–correction proposed in Chapter III is applicable thus in this context in order to account for the subgrid spatial variations in the evaporative regime.

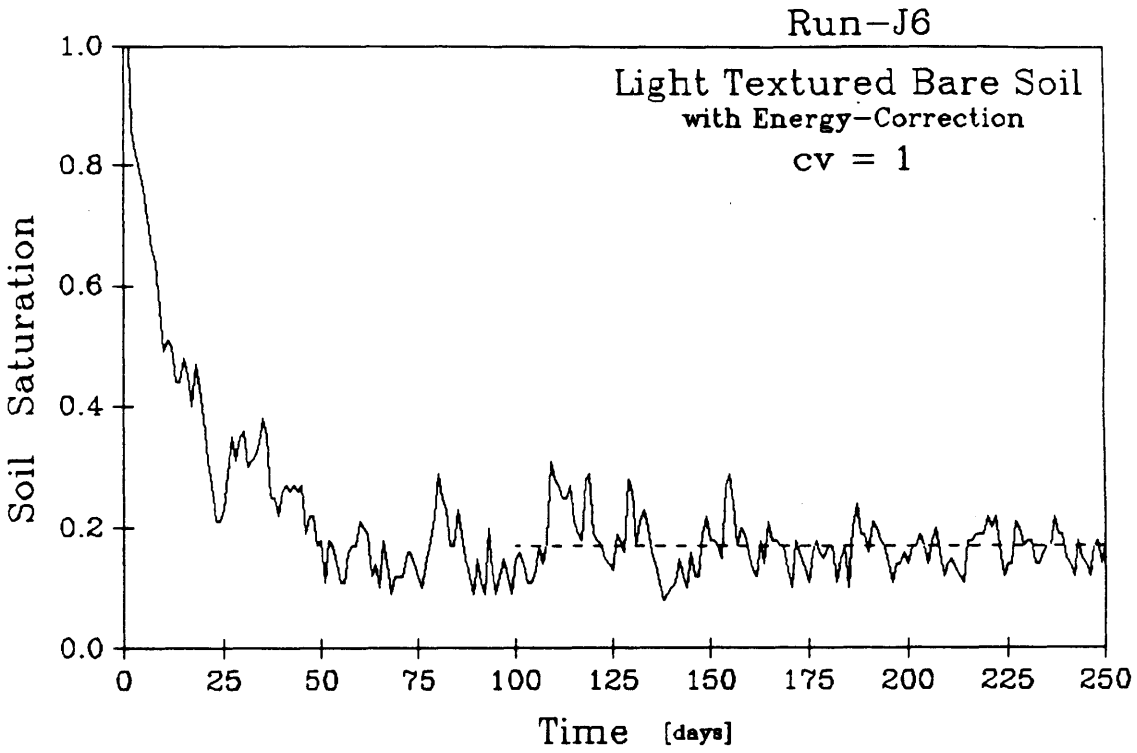

Fig. 4.22 Time series of surface relative soil saturation with subgrid hydrology parameterization, $cv = 1$, and light textured bare soil. The bare soil evaporation efficiency with energy–correction is used in this simulation. The dashed line represents the mean value established over the period when diagnostics were collected [Experiment J–6]

f. Multiple soil layers

So far, all simulations with the screening model have considered a single 10 cm soil layer at the landsurface boundary. Most operational GCMs today also contain a single (or at most two) soil layer as well. The inclusion of deeper soil storage has been suggested recently for some GCMs in order to improve the seasonal cycle of continental climates. Historically, some GCM model climates have been suffering from excessive summer drying and continental aridity.

In the winter months, presumably, the deeper soil layers will store the excess moisture. During the warm and dry summer months, in turn, the upward diffusion of deep soil water to the surface will provide for the required latent cooling that maintains the summertime continental climates in a reasonable state.

Multiple soil layers reaching greater depths are incorporated in the screening model. Figure 4.23 illustrates the two scenarios explored here; 3 and 5 layer systems are investigated. In the latter case, the surface soil layer thickness is reduced to 5 cm. Moisture is redistributed over the entire soil column according to physical principles of unsaturated flow through porous media. Heating affects only the surface layer since, in a perpetual–season simulation, there is no requirement for deeper thermal storage.

The numerical scheme used for updating the soil moisture contents at the various discrete soil layers is based on the model of Abramopoulos, Rosenzweig, and Choudhury (1988). In this model, each soil layer with depth Δz, porosity n, and relative soil saturation s, is characterized by the stored water depth

$$w = n\, s\, \Delta z \tag{4.35}$$

The change in storage at every level i (i=1,2,...,N) within the time step Δt is

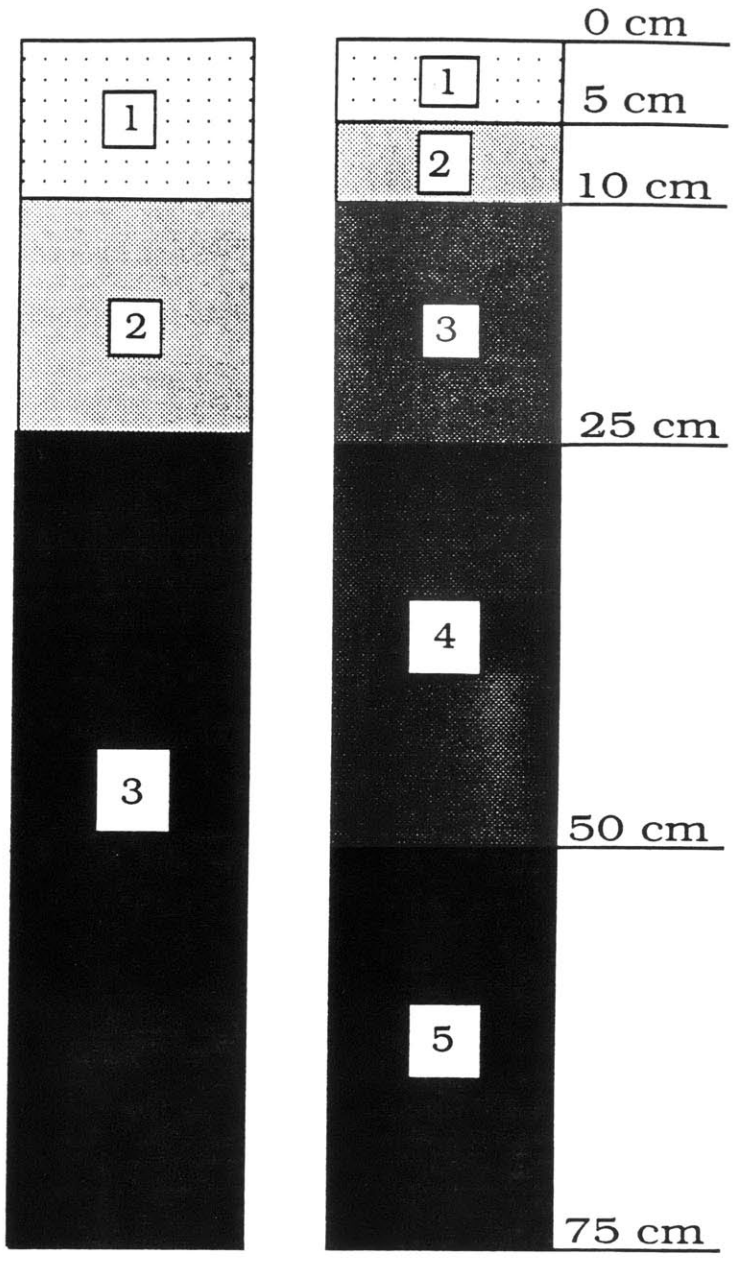

Fig. 4.23 The discretization for the soil profile into three and five layers

$$\frac{\Delta w_{i-1}}{\Delta t} = F_i - F_{i-1} \tag{4.36}$$

The flux F is based on the Darcy equation

$$F_i = K_i \frac{H_i - H_{i-1}}{z_i - z_{i-1}} \tag{4.37}$$

where H is the total hydraulic head and K is the hydraulic conductivity. Both H and K are parameterized in the manner presented in Appendix A. An implicit time scheme is used to estimate the flux between soil layers

$$F_i^{\alpha} = F_i + \alpha \left(\frac{\partial F_i}{\partial w_i} \Delta w_i + \frac{\partial F_i}{\partial w_{i-1}} \Delta w_{i-1} \right) \tag{4.38}$$

Substituting (4.38) in (4.36) and rearranging the terms results in the following algebraic set of linear update equations

$$\mathbf{A}\,\Delta\mathbf{w} = \mathbf{b} \tag{4.39}$$

where

$$A_{k,i-1} = \frac{\partial F_i}{\partial w_{i-1}} \Delta t \tag{4.40a}$$

$$A_{k,i} = \alpha \left(\frac{\partial F_{i+1}}{\partial w_i} - \frac{\partial F_i}{\partial w_i} \right) \Delta t - 1 \tag{4.40b}$$

$$A_{k,i+1} = \alpha \frac{\partial F_{i+1}}{\partial w_{i+1}} \Delta t \tag{4.40c}$$

$$b_i = (F_i - F_{i+1}) \Delta t \tag{4.40d}$$

The boundary condition at the landsurface is matching the flux into the first soil layer and the net infiltration–exfiltration. Below the lowermost soil level, there is a zero flux boundary condition.

Figure 4.24 contains the time–series of the relative soil saturations for the three soil layer system with light soil texture (Experiment M1). The entire soil column is initialized as saturated. The first soil layer (topmost) dries gradually but at a rate considerably lower than in the single soil layer experiment (Figure 4.12). The slower decay rate is due to the upward diffusion contribution of the second soil layer. In fact in Figure 4.24 we notice a discontinuity in the rate of soil moisture depletion in the first soil layer; so long as the second soil layer remains saturated in the simulation (first ~ 20 days) the first soil layer dries similar to Experiment J1 with a single soil store. When the second soil layer begins to lose moisture to upward diffusion, the rate of soil water depletion in the surface layer decreases significantly.

As evident in Figure 4.24, the middle soil column provides some of the moisture lost to evaporative flux from the surface. The temporal variability in the middle soil layer relative saturation is lower than the surface layer since it is not directly affected by atmospheric forcing. The lowermost soil layer (layer 3) remains saturated and does not lose moisture to upward diffusion and surface evaporation. With the inclusion of deeper soil layers, the size of the moisture reservoir at the landsurface is increased. This results in longer time periods required for the system to transition from the initial condition to its equilibrium state.

Once the model has reached equilibrium in the perpetual Julian day (~ 100 days), however, the mean relative soil saturation is only 0.20. Without deeper soil storage, the equilibrium relative soil saturation is higher, at 0.23 (Figure 4.12). This behavior is expected in light soils. For these soils, the surface layer will gravitationally lose the surface infiltration supply of moisture to deeper soil layers

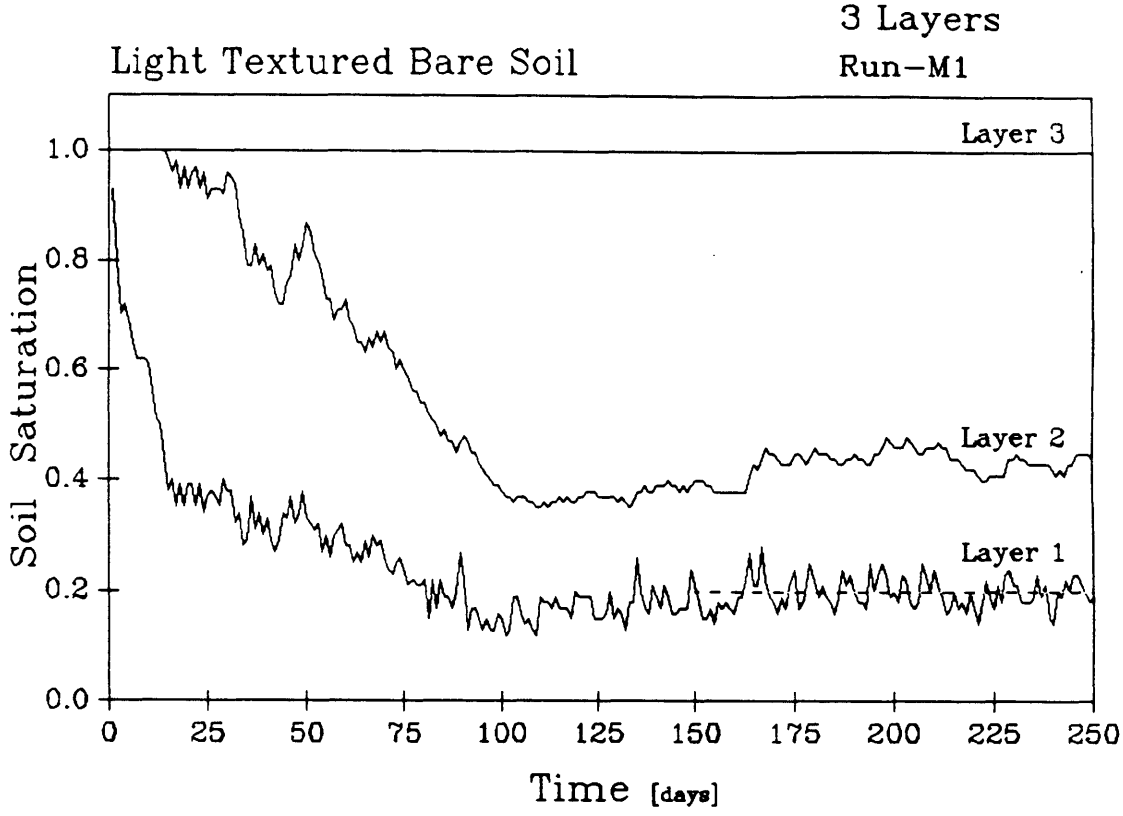

Fig. 4.24 Time series of relative soil saturations with subgrid hydrology parameterization, $cv = 1$, and light textured bare soil. The soil profile contains three discrete layers. The dashed line represents the mean value established over the period when diagnostics were collected for the surface soil layer. [Experiment M–1]

while, at the same time, they are not capable of maintaining strong matric suctions that cause significant upward diffusion of deeper soil water storage.

The capillary rise of moisture against gravity in discretized model soil columns may be enhanced by increasing the vertical resolution. In Experiment M2, the same soil column as in Experiment M1 is discretized into five layers; the topmost surface layer being only 5 cm thick. Figure 4.25 represents the time–series of the five soil layers' relative saturations, diurnally–averaged, during the simulation period.

Due to the smaller moisture reservoir at the landsurface, the temporal variance of the relative soil saturation in the first soil layer is increased. Variability in the second soil layer (depth 5 to 10 cm) variability closely follows the topmost layer. The third soil layer gradually loses its moisture store to upward diffusion but it also receives percolating water from the overlying soil layers. The lowermost levels (layers 4 and 5) remain saturated throughout the simulation period. The equilibrium relative soil saturation in the surface layer is 0.25 which is higher than that established for the three–layer system and only marginally higher than the single soil layer value of 0.23 (Experiments M4, J1, and M1). Given the degree of temporal variance in the model, the equilibrium soil saturation in the three experiments with light soil are not really distinguishable. Furthermore, as evident in Figure 4.25, there is a persistent anomaly in the model between 160 to 190 days into the simulation. This marked deviation in model behavior over 30 days is possibly due to model feedbacks that are triggered by unusual magnitude events. The equilibrium is therefore difficult to distinguish statistically. Multiple soil layering and the inclusion of deep soil water storage does not significantly modify the climate when the soil has weak capillary characteristics.

Soils with heavier textures (clayey soils) are capable of diffusing moisture against gravity (upward diffusion) rather effectively. They can also store water under tension, thus reducing the percolation loss of moisture from the surface to

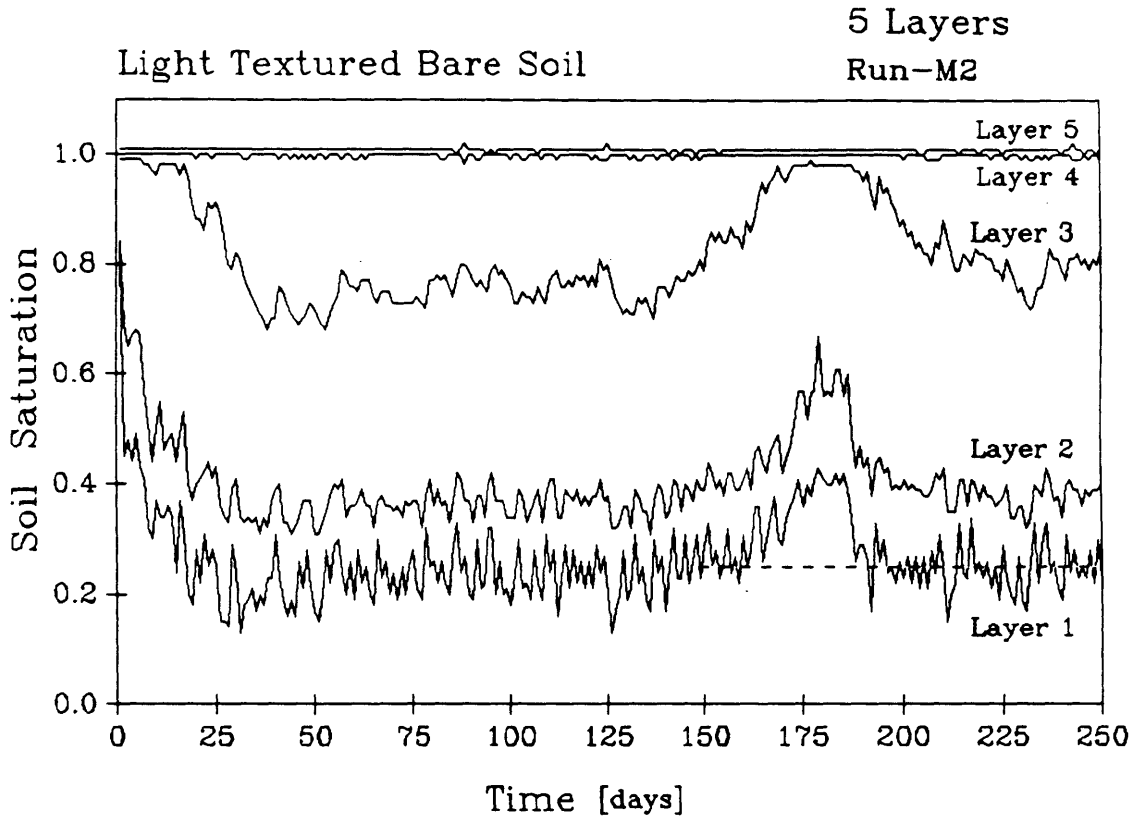

Fig. 4.25 Time series of relative soil saturations with subgrid hydrology parameterization, $cv = 1$, and light textured bare soil. The soil profile contains five discrete layers. The dashed line represents the mean value established over the period when diagnostics were collected for the surface soil layer [Experiment M–2]

deeper soil layers. As illustration, Experiment M2 is repeated but with the heavy soil composition. Figure 4.26 represents the soil saturation time–series for the five soil layers. In this case, the deeper soil water stores all lose moisture to upward diffusion under the strong matric suctions characteristic of heavy soils. Since simulation experiments with larger active soil reservoirs require longer periods to reach equilibrium, this run is extended over 400 diurnal cycles instead of the usual 250.

The equilibrium soil saturation for the five layer soil system characterized by heavy soil texture is 0.38 for the surface layer (established over the last 100 diurnal cycles). For this same soil type, the equilibrium relative soil saturation in a single 10 cm soil layer is only 0.15 (Figure 4.17). The inclusion of multiple soil layers, in this case, results in a considerably more moist soil surface when compared to when only one single soil layer is allowed.

Deep soil water storage is a measure designed to provide additional moisture during periods when excessive drying and aridity prevail in model climates. The soil texture, however, has a significant influence on the effectiveness of multiple soil layering.

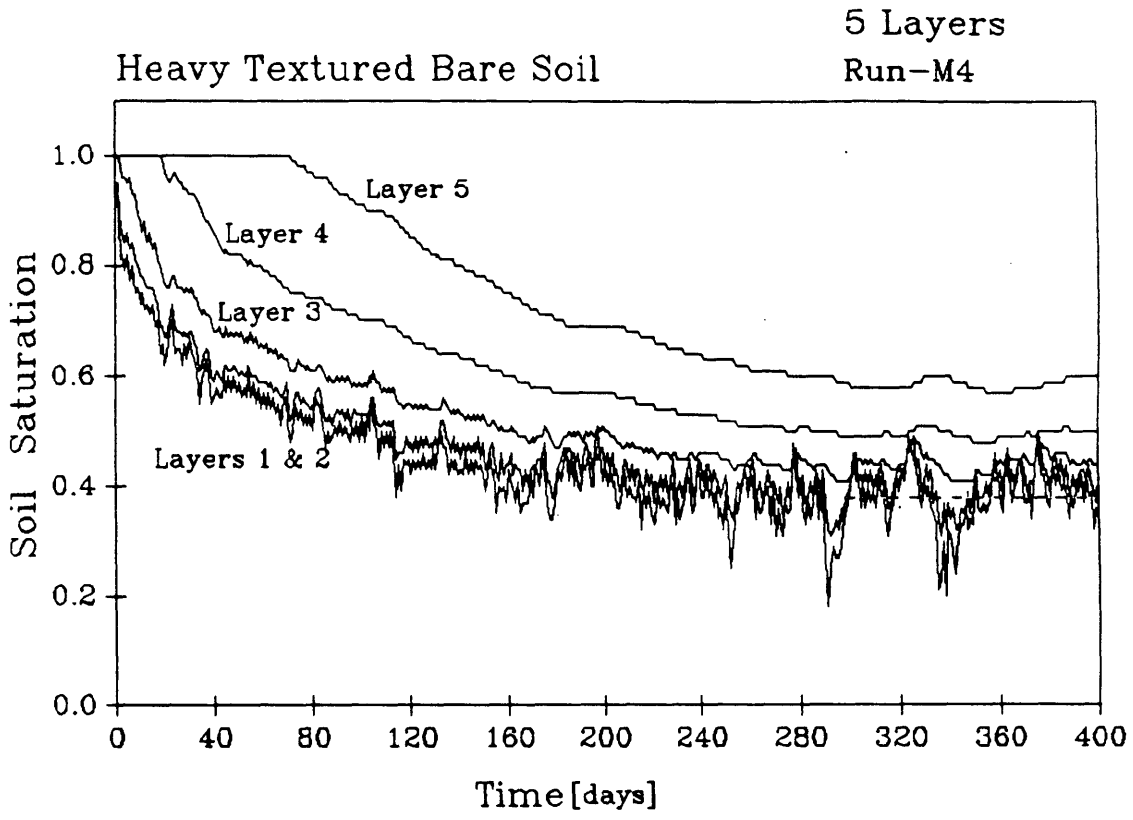

Fig. 4.26 Time series of relative soil saturations with subgrid hydrology parameterization, $cv = 1$, and heavy textured bare soil. The soil profile contains five discrete layers. The dashed line represents the mean value established over the period when diagnostics were collectedfor the surface soil layer [Experiment M–4]

V. Final remarks

1. Summary

More machine resources will lead to finer mesh numerical models, yet never on the finest scales actually present in the real physical processes. A number of processes in the climatic system must therefore be parameterized. Such subgrid parameterization within GCMs will always remain the Achilles' heel of numerical climate simulation. Unresolved spatial heterogeneity in hydrologic processes result in behavioral variabilities that are not captured when the large grid area is assumed to be a uniform hydrologic unit. The statistical–dynamical approach to hydroclimatological modelling promises to be a practical method of developing grid–average hydrologic flux expressions under conditions of smaller scale subgrid heterogeneity in parameters.

In Chapter II expressions have been derived to describe the runoff ratio, bare soil evaporation efficiency, and transpiration efficiency from a GCM grid area including subgrid scale spatial variability. The soil moisture conditions and the precipitation intensity are assumed to be spatially distributed over the grid area according to known statistical distributions whose parameters correspond to the areal mean values that are propagated in GCM integrations. The derivations have been based largely on dynamic hydrological relationships characterizing these processes.

The runoff ratio function is based on both the point–excess of rainfall intensity with respect to the local infiltrability, and the precipitation over the saturated area in near–channel zones and depressions. The essentials of soil moisture physics are retained in producing the runoff ratio which is a function of the point soil relative saturation, unsaturated soil hydraulic properties, and the precipitation intensity.

The bare soil evaporation efficiency is based on desorption physics for drying porous media. Soil capillarity and the strength of the atmospheric evaporative

demand are incorporated into the model such that the transition from a water–limited to a climate–controlled evaporation regime is modeled. The derived distribution of bare soil evaporation efficiency over a grid area with subgrid variance in soil moisture is necessary since the moisture loss from the soil is a nonlinear function of moisture content. Such dependence implies that the evaporation for the average soil moisture condition is not necessarily the same as the average of the evaporative flux for the distributed soil moisture conditions. A similar expression is derived for the transpiration efficiency using a simplified root soil moisture extraction model.

GCM computations may be subdivided generally into dynamical and physical parameterizations. The latter often require the consideration of processes on scales smaller than those sufficient for dynamical computations. The landsurface hydrology, as it has been presented here, appears to contain processes that warrant subgrid parameterization. However, such a parameterization should be incorporated in GCMs only if it promises to improve the model climate or to increase the model capability in capturing the consequences of environmental perturbations. The appropriate sensitivity tests and verification of the hydrologic parameterizations are performed both on an offline basis and online within a simplified climate model. The results of the online analyses within a GCM–type environment are presented after the following presentation of some offline comparisons.

In Chapter II, the sensitivity of the runoff ratio function to fractional wetting, precipitation intensity, and soil type are determined. Depending on the degree of grid–average soil saturation and its spatial variability, a fraction of the surface becomes impermeable to further infiltration. The incident rainfall over this fraction becomes runoff by the Dunne mechanism. Outside of this fraction, the runoff rate is critically dependent on the intensity of rainfall and soil type. In more intense events or within storms wetting a smaller fraction of the GCM grid, considerable

amounts of runoff may be produced by the Horton mechanism whereby the incident rainfall intensity exceeds the local infiltration capacity. This runoff term is generally low over light sandy soils since the porous soil has a rather large infiltration capacity. Over heavier soils with larger clay and loam content, however, Horton runoff is prevalent due to the relatively lower soil permeability. This condition is less effective when the soil is dry since heavy soils are characterized by strong matric tension at low moisture content. The incident rainfall, in this case, is infiltrated under the high capillary suction.

The bare soil evaporation efficiency function is parameterized using the soil desorption expression. Depending on soil conditions and the strength of potential evaporation (atmospheric evaporative demand), however, the evaporation rate from the surface may proceed at its potential limit. The relative saturation at which this transition from water–limited to climate–controlled evaporation regime takes place is denoted by s^*. At points within the grid where the surface soil saturation is below s^*, the evaporation rate is governed by soil desorption. At locations outside these areas, the soil evaporation rate is limited by the atmospheric evaporative demand. The transitional relative soil saturation s^* is a combined soil–climate parameter. Its value is sensitive to both soil type and the effective potential evaporation rate.

Clearly both water–limited and climate–controlled regimes may affect the grid surface when subgrid heterogeneity in surface soil saturation is allowed. Where the evaporation rate is limited to below the potential value, the amount of energy equal to their differences becomes surplus. This energy now becomes available to increase the local evaporative demand. In Chapter III, a simple parameterization of this effect is incorporated into the bare soil evaporation efficiency function. The magnitude of the necessary correction is clearly dependent on the size of the GCM grid fraction that is water–limited. There will be no such energy feedback when the

grid surface is mostly climate–controlled.

Soil type and the degree of spatial variability in soil saturation also affect the evaporation rate from bare surfaces. When there is little subgrid variability about the grid–average relative soil saturation then, depending on whether the water–limited or climate–controlled evaporative regime dominates, the bare soil evaporation rate will be determined mostly either by desorption or potential evaporation. In the climate–controlled case, the evaporation efficiency will be considerably lower if desorption alone is allowed.

The bare soil evaporation sensitivity to soil type is dependent on the degree of local soil saturation since the soil matric suction is a complex function of both soil texture and moisture content. The effect of soil type on the relative importance of gravity and capillary terms in the desorption equation is more straightforward, however. In heavy soils with high clay and loam contents, the matric suction is generally high and therefore gravity force is negligible in comparison with capillary force. In light sandy soils, however, gravity may significantly reduce moisture flux directed towards the opposite direction. This phenomenon is especially effective when the soil is close to saturation and the matric suction is rather small.

Soil moisture storage may also be depleted by extraction through vegetation roots. There is a soil saturation (s_w) below which the soil matric suction exceeds the plant's wilting point or the negative pressure limiting plant function. There is also the soil saturation s* above which the potential evaporation limits soil water extraction under tension gradients. The transpiration efficiency function is developed using these two basic transition levels in soil saturation; the transpiration rate is zero below the wilting level and it proceeds only at the potential rate when the local region is under the climate–controlled evaporative regime. Between s_w and s*, the root soil water extraction efficiency is said to be linear in either soil saturation or matric suction. In Chapters II the transpiration

efficiency function for the former case is derived under conditions of subgrid spatial variability in surface soil saturation. In Chapter III, the alternate root soil water extraction efficiency is used in a different derivation. Also in Chapter III, the effects of energy feedback when both water–limited and energy–controlled evaporative regimes are present over the large GCM grid are incorporated into this efficiency expression.

The transpiration rate sensitivity to vegetation type is realized through the wilting matric suction. Plants with lower wilting points (higher negative pressure) extract soil moisture over a wider fraction of the GCM grid. The transpiration efficiency function sensitivity to soil texture is due to the dependence of s* on soil type.

In Appendix E, a comparison is made between the landsurface hydrology parameterization including subgrid scale spatial variability and the soil hydrology model in the GISS GCM. Depending on the longterm average rainfall and potential evaporation rates (in terms of their dimensionless ratio $\mathcal{P}$), the resulting equilibrium relative soil saturation is determined. Their comparison is conditional on the soil type, degree of space–time concentration of rainfall, and the amount of subgrid spatial variability in surface soil saturation. In moist climates, the equilibrium relative soil saturation is higher in the case of the subgrid hydrology parameterization. In more arid climates, the GISS soil hydrology has a higher equilibrium relative soil saturation especially when the rainfall occurs in infrequent and small bursts. In this case, a considerable fraction of the rainfall is lost to runoff by the Horton mechanism which is implicit in the subgrid hydrology parameterization but wholly absent in the GISS soil hydrology.

There are numerous feedbacks in the landsurface–atmosphere system that are not captured in the sensitivity analyses performed on the offline basis. For a better understanding of all the sensitivities, the landsurface hydrologic parameterization

ought to be implemented in a full three–dimensional GCM. However, in order to perform numerous and lengthy simulations and furthermore work in a more controlled environment, a simplified climate model is used to screen various sensitivity analyses before designing experiments for the complete three–dimensional GCM.

The screening model is basically the solution to the GCM physical parameterizations over a grid area. The vertical discretization and time step in the model are identical to that of a GCM.

The moist convection scheme for the screening model is based on the GISS GCM parameterization. The radiation subroutines are derived from a one–dimensional radiative–equilibrium model. The landsurface module combines the GISS surface air layer scheme with the choice of soil hydrology model.

Since the model is one–dimensional and contains no dynamics, the convergence of heat and moisture must be parameterized within the screening model. For this purpose, the surface boundary of the screening model is divided between land and ocean with the sea surface temperature characteristic of the prescribed latitude. Adjacent airmasses in the columns overlying each surface type are exchanged according to a simple scheme. Heat and moisture derived from the ocean surface thus become available to the atmospheric column overlying the landsurface.

The heat and moisture exchange between the ocean and air columns is dependent on the scalar parameter χ. Higher values of χ imply less efficient mixing of airmasses. The surface incident rainfall over the landsurface is quite sensitive to χ. The rainfall rate decreases for higher values of χ due to the cutoff of oceanic moisture source. Below a certain limit for χ, the rainfall rate becomes insensitive to this parameter since mixing of oceanic and continental airmasses is virtually complete. Both subgrid hydrology parameterization and the GISS soil hydrology

result in a similar rainfall and χ relationship.

The landsurface runoff rate, however, exhibits significant differences depending on whether the subgrid hydrology parameterization or the GISS soil hydrology are used. The former landsurface hydrology parameterization produces nearly twice the runoff of the latter model at similar values of χ. This behavior is related to the fact that the rainfall in the screening model is due to moist convection; such rainfall is usually intense and runoff by Horton mechanism is prevalent when using the subgrid hydrology parameterization. The GISS soil hydrology, on the other hand, does not base its estimate of the runoff ratio on the rainfall intensity.

For these same reasons, the time–series resulting from the subgrid hydrology parameterization are significantly less variable about the longterm mean established by the perpetual Julian day simulation with the screening model. A larger fraction of more intense rainfall events becomes (Horton) runoff when using the subgrid hydrology. In the GISS soil hydrology model, however, such intense events rapidly fill the soil storage and thus generate large excursions above the longterm mean. Soil moisture depletion processes then return the storage toward equilibrium.

The characteristic time scale of soil moisture storage is on the order of tens of days and months. The reduction in variance about the longterm mean is therefore a desirable characteristic in numerical experiments that require the model climate to reach equilibrium as rapidly as possible. The inclusion of an annual cycle, of course, further complicates the efficient reduction of the initial transience in climate models.

In a series of screening model simulations with the subgrid hydrology parameterization, the model sensitivity to several parameters and conditions are investigated. Changing the soil texture, for example, resulted in different hydrologic responses. With heavier soils, the model is characterized by more rapid soil moisture decay from its initial saturated value. Also in this case, the longterm

mean soil moisture is low since greater Horton runoff occurs. Both of these behaviors in heavier clay and loam soils is due to the strong soil capillary and low permeability properties. The model sensitivity to the degree of subgrid spatial variability (*cv*) in surface soil saturation is found to be strictly dependent on soil type. There is strong sensitivity to *cv* only in the case of heavier soils. Both the inclusion of a vegetation cover and the incorporation of the energy–correction results in the reduction of the equilibrium surface soil saturation due to greater efficiency in evaporative moisture loss inherent to these parameterizations.

In an additional set of screening model simulation experiments, the climate model sensitivity to the increase in soil water capacity and multiple soil layering is investigated. Again the effectiveness of this parameterization is dependent on soil type. For light soils, the surface relative soil saturation is lower when more soil layers are allowed below the surface layer. In these sandy soils, water may percolate to deeper unsaturated layers. Meanwhile the soil is not characterized by enough matric tension to overcome gravity force and extract moisture from deeper storage. In heavier soils with greater clay and loam content, the soil capillary forces are strong enough to diffuse moisture vertically, against gravity, over the entire soil profile.

2. Conclusions

The development of the subgrid hydrology parameterization for atmospheric general circulation models and the subsequent offline sensitivity analyses resulted in some insight into the hydrology of large scale land areas. The effects of soil type, the degree of spatial heterogeneity in surface moisture conditions, and the magnitude of rainfall and potential evaporation forcing are clearly evident in the sensitivity tests. Listed below are some of the major findings;

1) In order to model surface runoff in a physically realistic manner and over large land areas, it is necessary to consider the statistical distribution of rainfall and soil moisture conditions on finer scales.

2) Surface runoff dependence on soil type is governed by the soil saturated hydraulic conductivity and capillarity as follows; On light–textured soils, the saturated hydraulic conductivity is high enough such that even the most intense rainfall events do not results in infiltration excess. On clayey soils, there may be considerable surface runoff by the Horton mechanism but the inclusion of soil capillarity results in a significant reduction in infiltration excess in these fine textured soils.

3) Bare soil evaporation as a desorption process is affected by gravity and capillarity forces in different degrees depending on soil type. The inclusion of gravity in the formulation has significant effects only in sandy soils that are nearly saturated.

4) The equilibrium relative soil saturation resulting from the subgrid hydrology model compares with that from the GISS soil hydrology; When the rainfall is delivered in brief and intense events, greater surface runoff by the Horton mechanism occurs in the subgrid hydrology model and thus the equilibrium surface soil saturation is reduced below that of the GISS model.

Offline sensitivity analyses cannot fully capture the impact of the landsurface hydrology parameterizations on the model climate. For more detail sensitivity analyses, a screening climate model is developed. This one–dimensional model is essentially a zonal radiative–convective equilibrium model with an active soil hydrology. The dynamic transport of heat and moisture is parameterized in this model. The results of sensitivity analyses with this model also provided some insights into the hydroclimatology of large land areas. They are listed as follows;

1) Surface runoff in climate models is coupled to the convergence of latent heat in the atmospheric column. This component of the landsurface hydrology is far from a 'residual' since it actively modifies the heat and moisture balance in the overlying atmospheric column.

2) The subgrid hydrology parameterization, as opposed to simple GCM soil hydrology models, results in significantly less variability around the climate in the numerical model since it is nonlinearly dependent on the rainfall intensity and potential evaporation rate forcing.

3) The parameterized lateral convergence of heat and moisture considers a simple linear reservoir scheme for exchanging properties of adjacent land and ocean air. The linear reservoir parameter signifies the efficiency of this mixing such at a certain value and beyond complete airmass mixing results in an upper limit to moisture convergence and rainfall over continental regions.

4) The effectiveness of including multiple soil layers at the landsurface boundary of GCMs is critically dependent on the governing soil type and soil properties. Heavy textures soils can use deep seasonal storage effectively while lighter textured soils are incapable of retrieving moisture from lower soil layers during periods of water deficit. The inclusion of larger soil moisture storage at the surface results in longer time periods necessary to reach model climate equilibrium.

3. Future research

The landsurface hydrology parameterization including subgrid scale spatial variability developed in Chapters II and III is a demonstration of the statistical–dynamical approach. In order to assemble a complete landsurface module for a GCM, a number of other processes must be modelled. Furthermore, some topics in model calibration ought to be investigated. These issues are enumerated below as suggestions for future research in landsurface parameterization;

1) similar statistical–dynamical derivation of expressions for canopy retention volume,

2) modelling of snow and ice processes,

3) improved estimation of potential evaporation and ground heat storage,

4) subgrid modelling of surface air layer and its stability,

5) test the assumptions of the energy–correction using numerical atmospheric boundary layer models,

6) develop more efficient numerical schemes to integrate the surface prognostics,

and

7) parameterize *cv* as a function of landsurface physiography and hydrology.

The motivation for using the simplified screening climate model has been to develop the necessary information base for designing effective and meaningful experiments for the full three–dimensional GCM. The implementation of the subgrid hydrology parameterization in a GCM and the verification of its diagnostics with observations are, therefore, the primary avenues of future research.

Nevertheless, the one–dimensional screening model is still an excellent apparatus to study important landsurface–atmosphere feedbacks in the numerical climate model environment. In an integrated system like the global climate, where the constituitive processes interact with enormous complexity, a simplified analog such as the screening model provides a controlled environment for posing and answering questions. Such a model is educational rather than operational. No climate forecast may be made using the screening model; yet important lessons about the climate may be learned.

There is virtually no limit to the possible ways to modifying and improving

such one–dimensional climate model. Listed below are a few topics for further work on the screening model as it stands today;

1) use an active sea–surface temperature boundary condition,

2) parameterize χ based on observations of zonally averaged moisture convergence over land areas,

3) string additional air columns adjacent to one another to study the effects of continentality,

4) test alternate moist convection and cloud schemes,

and

5) study the dynamical properties of the model transience with special reference to chaotic behavior and multiple attractors.

Considering the myriad of ways the general circulation of the atmosphere and the hydrologic cycle affect one another, atmospheric modelers should recruit the experience of hydrologists. In turn, hydrologists should actively participate in improving GCMs, adding to their arsenal of tools for analyzing the variabilities in the hydrologic cycle. As with all complex models having numerous interacting components, meaningful GCM simulations can only be designed if the experimenter is sufficiently familiar with all the facets of the model. Hydrologists concerned with GCMs and global hydrology must therefore train in atmospheric science and re–educate the field in the interdisciplinary character of its science; hydrology among the earth sciences.

References

Abramopoulos, F., C. Rosenzweig, and B. Choudhury, 1988: Improved ground hydrology calculations for GCMs—Soil water movement and evapotranspiration, *Journal of Climate, 1(9)*, 921–941.

Bell, K.R., B.J. Blanchard, T.J. Schmugge, and M.W. Witczk, 1980: Analysis of surface moisture variations within large–field sites, *Water Resour.* Res., *16(4)*, 796–810.

Brooks, R.H. and A.T. Corey, 1966: Properties of porous media affecting fluid flow, *Journal Irrig. Drain. American Soc. Civil Eng., IR2*, 61–88.

Brutsaert, W., and H. Stricker, 1979: An advection–aridity approach to estimate actual regional evaporation, *Water Resour. Res.*, 15(2), 443–450.

Carslaw, H. S. and J. C. Jaeger, *Conduction of heat in solids*, Second Edition, Oxford University press, New York, 1959.

Carson, D. J., 1982: Current parameterizations of landsurface processes in atmospheric general circulation models, in *Landsurface Processes in Atmospheric General Circulation Models*, P. S. Eagleson (Ed.), Cambridge University Press, London, 67–108.

Dickinson, R. E., J. Jager, W. M. Washington, and R. Wolski, 1981: *Boundary Subroutine for NCAR Global Climate Model*, NCAR Technical Note 173TIA.

Dopplick, T. G., 1970: Global radiative heating of the earth's atmosphere, *Planetary Circulations Project Report No. 24,* Department of Meteorology and Physical Oceanography, Massachusetts Institute of Technology

Dunne, T., and R. D. Black, 1970: Partial area contributions to storm runoff in a small New England watershed, *Water Resour. Res.*, *6*(5), 1296–1311.

Eagleson, P. S., 1978–a: Climate, soil, and vegetation 1. Introduction to water balance dynamics, *Water Resour. Res.*, *14*(5), 705–712.

Eagleson, P. S., 1978–b: Climate, soil, and vegetation 3. A simplified model of soil moisture movement in the liquid phase, *Water Resour. Res.*, *14*(5), 722–730.

Eagleson, P. S., 1978–c: Climate, soil, and vegetation 4. The expected value of annual evapotranspiration, *Water Resour. Res.*, *14*(5), 731–739.

Eagleson, P. S., 1984: The distribution of catchment coverage by stationary rainstorms, *Water Resour. Res.*, *20*(5), 581–590.

Eagleson, P. S., N. M. Fennessey, Q. Wang, and I. Rodriguez–Iturbe, 1987: Application of spatial Poisson models to air mass thunderstorm rainfall, *J. Geophysical Research*, *92*(D8), 9661–9678.

Eagleson, P. S. and Q. Wang, 1985: Moments of catchment storm area, *Water Resour. Res.*, *21*(8), 1185–1194.

Entekhabi, D., and P. S. Eagleson, 1989: Landsurface hydrology parameterization for atmospheric general circulation models including subgrid scale spatial variability, *J. of Climate,* 2(8), 816–831.

Feddes, R. A., P. J. Kowalik, and H. Zaradny, 1978: *Simulation of field water use and crop yield*, John Wiley and Sons, New York, 188 pages

Freeze, R. A., 1974: Streamflow generation, *Water Resour. Res., 12(4),* 627–647.

Gradshteyn, I. S. and I. M. Ryzhik, 1980: *Table of Integrals, Series, and Products*, Academic Press, New York, page 925.

Hansen, J., G. Russel, D. Rind, P. Stone, A. Lacis, S. Lebedeff, R. Ruedy, and L. Travis, 1983: Efficient three–dimensional global models for climate studies: Models I and II, *Mon. Wea. Rev.,* 111(4), 609–662.

Hewlett, J. D., 1961: Watershed Management, Report for 1961 *Southeastern Forest Experiment Station*, Ashville, NC, 61–66, available from author.

Hewlett, J. D. and R. A. Hibbert, 1965: Factors affecting the response of small watersheds to precipitation in humid areas, paper presented at the International Symposium on Forest Hydrology, Pennsylvania State University, University Park, available from author.

Hoffman, R. N., 1981: A computer program which calculates radiative fluxes and heating rates in model atmospheres, *Scientific Report No. 4, Project for the Study of Climatic Fluctuations, Volcanic Aerosols, and Carbon Dioxide Changes,* Department of Meteorology and Physical Oceanography, Massachusetts Institute of Technology, 124 pages.

Koster, R. D., P. S. Eagleson, and W. S. Broecker, 1988: Tracer water transport and subgrid precipitation variation within atmospheric general circulation models, R*alph M. Parsons Laboratory Report # 317*, Department of Civil Engineering, Massachusetts Institute of Technology, 364 pages.

Milly, P. C. D., and P. S. Eagleson, 1988: Effects of storm scale on surface runoff volume, *Water Resour. Res., 24*(4), 620–624.

Molz, F. J., 1981: Models of water transport in the soil–plant system: A review, *Water Resour. Res., 17*(5), 1245–1260.

Morton, F. I., 1965: Potential evaporation and river basin evaporation, *Proc. American Soc. Civil Eng.,* Hydraulics Div., HY6, 67–97.

Mualem, Y., 1976: A catalogue of hydraulic properties of unsaturated soils, *Hydrodynamics and Hydraulics Laboratory, Israel Institute of Technology*, 100 pages, available from U.S. Department of Agriculture, Beltsville, Maryland.

Mualem, Y., 1978: Hydraulic conductivity of unsaturated porous media: Generalized macroscopic approach, *Water Resour. Res., 14(2)*, 325–334.

Owe, M., E. B. Jones, and T. J. Schmugge, 1982: Soil moisture variation patterns observed in Hand County, South Dakota, *Water Resour. Bull.*, *18*(6), 949–954.

Parlange, J–Y., M. Vauclin, R. Haverkamp, and I. Lisle, 1985: Note: The relation between desorptivity and soil–water diffusivity, *Soil Science*, *139*, 458–461.

Philip, J. R., 1957a: The theory of infiltration: 1. The infiltration equation and its solution, *Soil Science*, *83*, 345–357.

Philip, J. R., 1957b: The theory of infiltration: 4. Sorptivity and algebraic infiltration equations, *Soil Science*, *84*, 257–264.

Richardson, L. F., 1922: *Weather prediction by numerical process,* Cambridge University Press, Cambridge, U.K.

Sellers, P. J., Y. Mintz, Y. C. Sud, and A. Delcher, 1986: A simple biosphere model (SiB) for use within General Circulation Models, *J. Atmos. Sci.*, 43(6), 505–531.

Sud, Y. C., and M. S. Fennessy, 1982: An observational–data–based evapotranspiration function for General Circulation Models, *Atmosphere–Ocean*, 20, 301–316.

Warrilow, D. A., 1986: Indications of sensitivity of European climate to land use variations using a one–dimensional model, Proceedings of conference on parameterization of landsurface characteristics, use of satellite data in climate models, and first results of ISLSCP, Rome.

Warrilow, D. A., A. B. Sangster, and A. Slingo, 1986: Modelling of land surface processes and their influence on European climate, *U.K. Meteorological Office, DCTN 38*, 94 pages, available from the UK Meteorological Office.

Wetzel, P. J., and J.–T. Chang, 1987: Concerning the relationship between evapotranspiration and soil moisture, *J. of Climate and Appl. Meteo.*, 26(1), 18–27.

Wetzel, P. J., and J.–T. Chang, 1988: Evapotranspiration from nonuniform surfaces: A first approach for short–term numerical weather prediction, *Mon. Wea. Rev.*, 116(3), 600–621.

Appendix A. Desorptivity function

Sorptivity is a soil capillary property and is independent of gravity. In defining the desorptivity S_e, we thus begin with the horizontal (x–direction) soil moisture diffusion equation

$$\frac{\partial \theta}{\partial t} = \frac{\partial}{\partial x}\left[D(\theta) \frac{\partial \theta}{\partial x} \right] \tag{A.1}$$

For desorption boundary and initial conditions ($\theta(0,t)=0$; $\theta(x,0)=\theta_0$; $x,t \geq 0$), one may define a weighted *effective* diffusivity D_e such that (A.1) becomes

$$\frac{\partial \theta}{\partial t} = D_e \frac{\partial^2 \theta}{\partial x^2} \tag{A.2}$$

with the solution (Carslaw and Jaeger, 1959)

$$\theta(x,t) = \theta_0 \ \mathrm{erf}\left[\frac{x}{2\sqrt{D_e t}}\right] \tag{A.3}$$

The flux across the plane x = 0, differentiating (A.3), is

$$\text{flux} = D_e \frac{\partial \theta}{\partial x}\bigg|_{x=0} = \theta_0 \left[\frac{D_e}{t\,\pi}\right]^{1/2} \tag{A.4}$$

Eliminating $t^{-1/2}$ between Eqs. (A.4) and (2.22) without the gravity terms ($\delta = 0$; horizontal desorption) results in

$$S_e = 2\,\theta_0 \left[\frac{D_e}{\pi}\right]^{1/2} \tag{A.5}$$

We parameterize effective diffusivity D_e similar to Eagleson (1978b)

$$D_e = \varphi_e \, D(\theta) \tag{A.6}$$

where φ_e is the coefficient by which the soil water diffusivity is scaled in order to yield the *effective* diffusivity for the prescribed boundary and initial conditions. Combining (A.5) and (A.6) yields

$$S_e = 2 \, \theta_0 \left[\frac{\varphi_e \; D(\theta_0)}{\pi} \right]^{1/2} \tag{A.7}$$

Once the functional forms of φ_e and soil water diffusivity $D(\theta)$ are defined, the expression for S_e dependent on the initial moisture content θ_0 is complete.

The soil hydraulic properties are parameterized analogous to Brooks and Corey (1966) as

$$\Psi(s) = \Psi(1) \, s^{-\frac{1}{m}} \tag{A.8}$$

and

$$K(s) = K(1) \, s^{\frac{2}{m} + 3} \tag{A.9}$$

where m is the soil pore–size distribution index. From the definition of soil water diffusivity [Eq. (2.19)],

$$D(s) = K(s) \frac{d\Psi}{d\theta}$$

$$= \frac{K(1) \;\; \Psi(1)}{nm} \, s^{\frac{1}{m} + 2} \tag{A.10}$$

where n is the effective porosity.

Recently Parlange et al. (1985) note that for desorption

$$S_e^2 = \frac{8}{3}\,\theta_0^2 \int_0^1 (1-\frac{\theta}{\theta_0})\, D(\frac{\theta}{\theta_0})\, d\frac{\theta}{\theta_0} \qquad (A.11)$$

which upon integration with (A.10) yields

$$S_e^2 = \frac{8\ \ \theta_0^2}{3(\frac{1}{m}+3)(\frac{1}{m}+4)} \left[\frac{K(1)\ \ \Psi(1)}{nm}\, s_0^{\frac{1}{m}+2} \right]$$

$$= \frac{8\ \ \theta_0^2}{3(\frac{1}{m}+3)(\frac{1}{m}+4)}\, D(s_0) \qquad (A.12)$$

where $s_0 = \theta_0 / \theta_{sat} = \theta_0 / n$.

Combining (A.7) and (A.12) results in the definition

$$\varphi_e = \frac{2\,\pi m^2}{3(1+3m)\,(1+4m)} \qquad (A.13)$$

A comparison plot of this definition for φ_e and the one derived by Eagleson (1978b) is presented as Figure A.1.

To complete the definition of the desorptivity function, we back–substitute (A.13) into (A.7),

$$S_e = \left[\frac{8n\ K(1)\ \Psi(1)}{3(1+3m)(1+4m)} \right]^{1/2} s_0^{\frac{1}{2m}+2} \qquad (A.14)$$

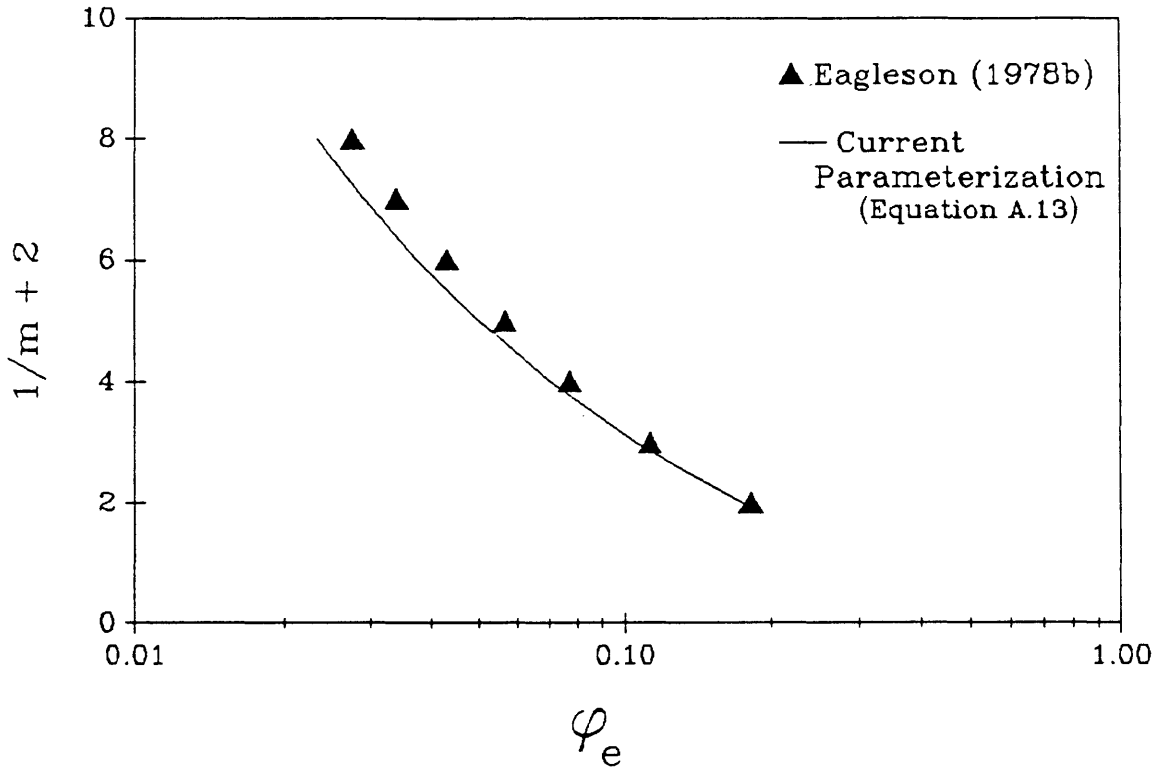

Fig. A.1 The effective diffusivity factor dependence on the soil pore–size distribution index

Appendix B: Soil hydraulic properties

The soil hydraulic properties cited in Table 2.1 are based on our reinterpretation of the data presented by Mualem (1978). The saturated moisture content θ_{sat} is regarded as the independent variable identifying soil types and textures. We assign

$$\begin{array}{ll} \text{Sand} & \theta_{sat} = 0.25 \\ \text{Silt} & \theta_{sat} = 0.35 \\ \text{Clay} & \theta_{sat} = 0.45 \end{array} \qquad \text{(B.1)}$$

after the retention volume θ_r has been removed.

Table 2 in Mualem (1978) catalogs fifty values for θ_{sat}, θ_r, and m (pore disconnectedness index) as well as Ψ at θ_r for different soils. Using the Brooks and Corey (1966) model for soil water retention, we back calculate the fitted parameter $\Psi(1)$.

Plots of $\Psi(1)$ and m versus the independent variable θ_{sat} appear in Figures B.1 and B.2. The outlier data below $\theta_{sat} = 0.20$ are sandstone values. They are excluded from the fitted curves

$$m = 40 \exp \{ -10\ \theta_{sat} \} \qquad \text{(B.2)}$$

and

$$\Psi(1) = 4 \exp \{ 7\ \theta_{sat} \} \qquad \text{(B.3)}$$

The parameters in Table 2.1 are based on; 1) Saturated hydraulic conductivity K(1) values from Eagleson (1978b), and 2) expressions (B.1) to (B.3).

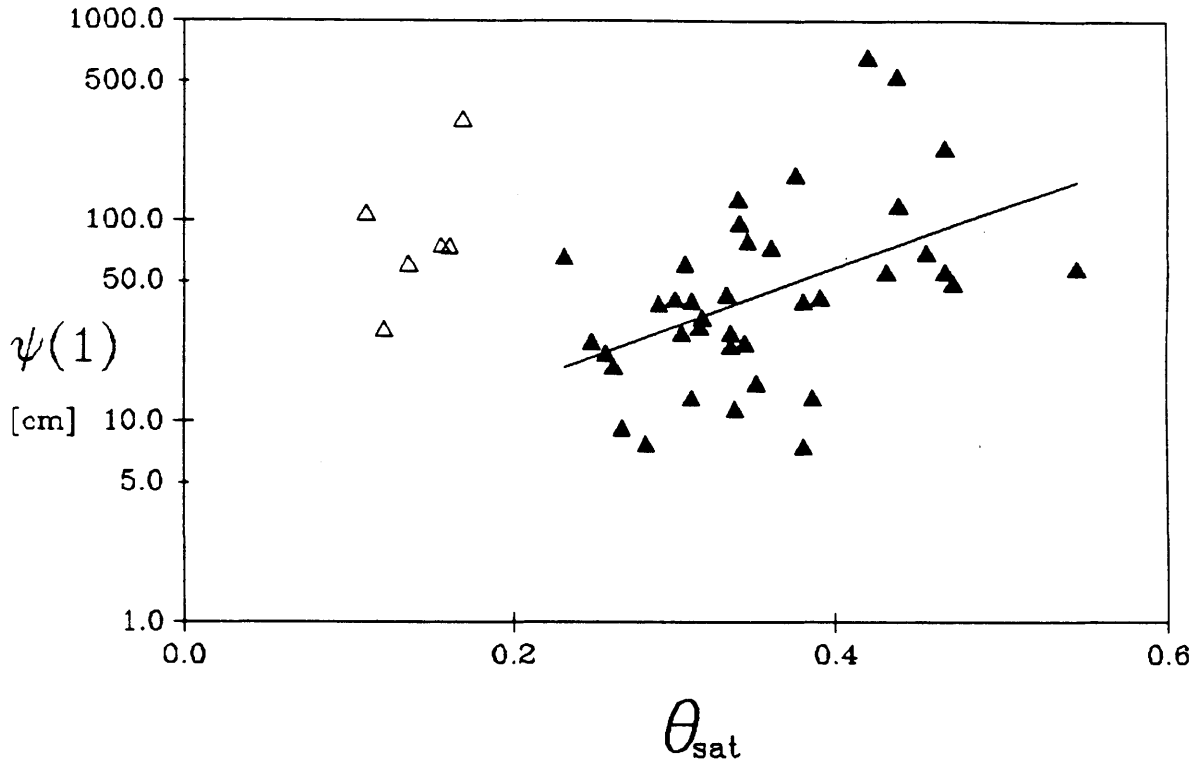

Fig. B.1 Dependence of the $\Psi(1)$ parameter on the soil saturated water content

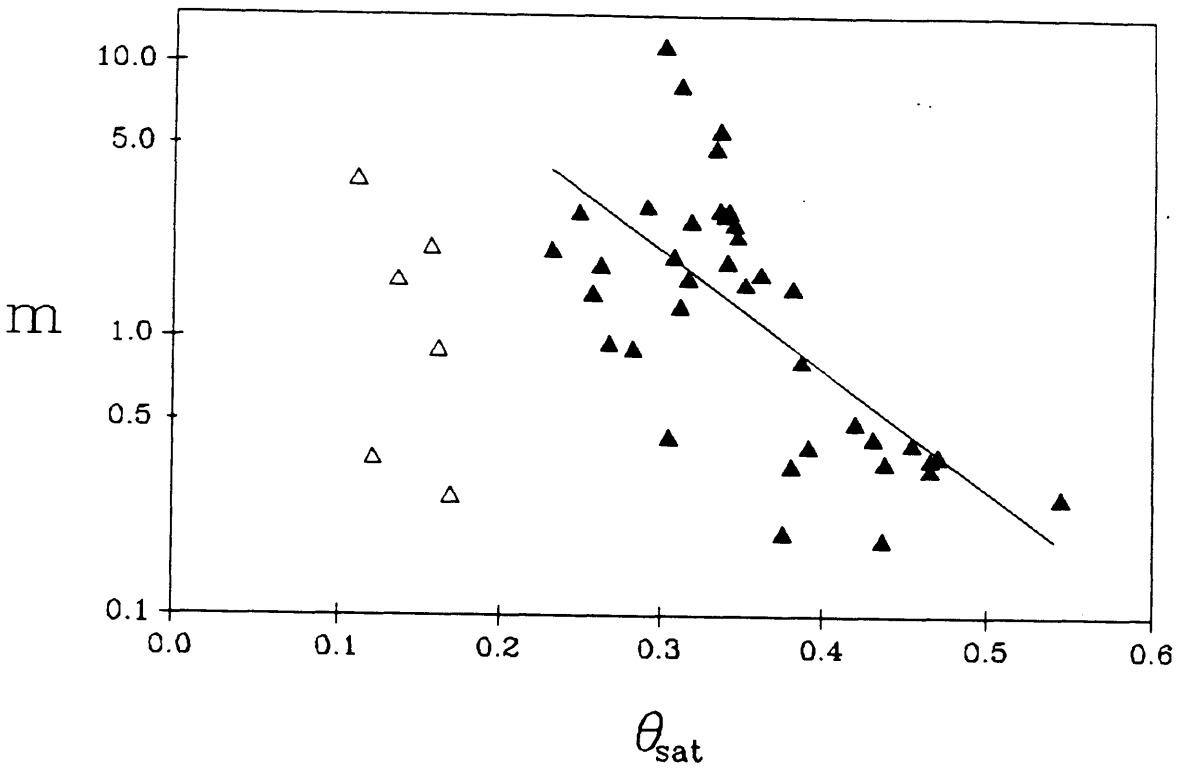

Fig. B.2 Dependence of the pore–size distribution index (m) on the soil saturated water content

Appendix C: The numerical evaluation of transcendental functions in the expressions

The runoff ratio function is

$$R = 1 - \frac{\gamma(\alpha, \frac{\alpha}{E[s]})}{\Gamma(\alpha)} + \frac{e^{-\kappa I(1-v)} \quad \gamma(\alpha, \kappa Iv + \frac{\alpha}{E[s]})}{(\frac{\kappa IvE[s]}{\alpha}+1)^{\alpha} \quad \Gamma(\alpha)} \tag{C.1}$$

where $\gamma(\alpha,x)$ is the incomplete gamma function and $\Gamma(\ )$ is the complete gamma function. The variable v

$$v = -\frac{|\Psi(1)|}{m\ \Delta z} \tag{C.2}$$

may be a potentially large negative number and depending on the realization of κI and $\frac{\alpha}{E[s]}$, x may turn out to be a negative number as well. Evaluating $\gamma(\ ,\ )$ using standard mathematical library subroutines is not always possible since the argument of the function

$$\gamma(\alpha,x) \tag{C.3}$$

where

$$x = \kappa Iv + \frac{\alpha}{E[s]}$$

may turn out to be less than zero [both parameters α and x must be non–negative in $\gamma(\alpha,x)$]. Moreover, when $x < 0$, the evaluation of $\left[\frac{\alpha\, x}{E[s]}\right]^{\alpha}$ in the denominator

of (C.1) is also problematic by itself.

A simple transformation of (C.1) gives

$$R = 1 - \frac{\gamma(\alpha, \frac{\alpha}{E[s]})}{\Gamma(\alpha)} +$$

$$e^{-\kappa I(1-v)} \left[\frac{\alpha}{E[s]} \right]^{\alpha} \gamma^*(\alpha, \kappa I v + \frac{\alpha}{E[s]}) \qquad (C.4)$$

where

$$\gamma^*(\alpha,x) = \frac{x^{-\alpha}}{\Gamma(\alpha)} \gamma(\alpha,x) \qquad (C.5)$$

For this definition of the incomplete gamma function we only require that

$$|\alpha| \ , \ |x| < +\infty \qquad (C.6)$$

We approximate (C.5) as

$$\gamma^*(\alpha,x) = e^{-x} \sum_{n=0}^{\infty} \frac{x^n}{\Gamma(\alpha+n+1)} \qquad (C.7)$$

which converges rapidly for $\alpha > 0$ and $|x|$ small.

When $|x|$ is large, the second term in (C.4) is close to zero. For $x \to +\infty$, e^{-x} diminishes more rapidly than the remainder terms, thus $\gamma^*(\alpha,x)$ is asymptotically zero. For $x \to -\infty$, the $e^{-\kappa I(1-v)}$ term in (C.4) diminishes in magnitude, and again, the second term in (C4) approaches zero. The $|x|$ large case, basically, denotes the absence of surface runoff by the Horton mechanism.

Appendix D: Approximation to integral in the transpiration efficiency function with energy–balance correction

We need to evaluate the integral

$$J = \int_0^u \frac{x\,(x + c)^{\alpha - 1}}{x + u}\, e^{-x}\, dx \tag{D.1}$$

where

$$c = \alpha \text{ [illegible]}^{-1}$$

$$u = \alpha \text{ [illegible]}^{-1} - \alpha \text{ [illegible]}^{-1} \tag{D.2}$$

With $\alpha = cv^{-2}$ on the order of $O(1)$ to $O(10)$, approximate

$$(x + c)^{\alpha-1} = \sum_{k=0}^{\alpha-1} \binom{\alpha-1}{k} x^k\, c^{\alpha-k-1} \tag{D.3}$$

Substitute (D.3) in (D.2) and write

$$J = \int_0^u \frac{x\, e^{-x}}{x + u} \sum_{k=0}^{\alpha-1} \binom{\alpha-1}{k} x^k\, c^{\alpha-k-1}\, dx \tag{D.4}$$

Let $z = \frac{x}{u}$; rearrange (D.4) to obtain

$$J = \sum_{k=0}^{\alpha-1} \binom{\alpha-1}{k} u^{k+1}\, c^{\alpha-k-1} \int_0^1 z^{k+1}\, e^{-uz}\, (z + 1)^{-1}\, dz \tag{D.5}$$

There is still no analytical closed–form evaluation of the integral in (D.5).

Since $0 \leq z \leq 1$, we may write $(z + 1)^{-1}$ as the Taylor Series expansion around 1/2,

$$f(z) = (z + 1)^{-1} \tag{D.6}$$

$$= f(\tfrac{1}{2}) + (z - \tfrac{1}{2})\, f'(\tfrac{1}{2}) + \tfrac{1}{2}\,(z - \tfrac{1}{2})^2\, f''(\tfrac{1}{2}) + \tfrac{1}{6}\,(z - \tfrac{1}{2})^3\, f'''(\tfrac{1}{2}) + \ldots$$

Noting that

$$\begin{aligned} f(z) &= (z + 1)^{-1} \\ f'(z) &= -(z + 1)^{-2} \\ f''(z) &= 2\,(z + 1)^{-3} \\ f'''(z) &= -6\,(z + 1)^{-4} \end{aligned} \tag{D.7}$$

we find

$$f(z) = a_1 z^3 + a_2 z^2 + a_3 z + a_4 \tag{D.8}$$

where

$$\mathbf{a} = \begin{bmatrix} -16/81 \\ 16/27 \\ -24/27 \\ 80/81 \end{bmatrix} \tag{D.9}$$

Substituting (D.8) and (D.9) in (D.5) and integrating results in

$$J = \sum_{k=0}^{\alpha-1} \binom{\alpha-1}{k} c^{\alpha-k-1} \tag{D.10}$$

$$\{a_1 u^{-4} \gamma(k+5,u) + a_2 u^{-3} \gamma(k+4,u) + a_3 u^{-2} \gamma(k+3,u) + a_4 u^{-1} \gamma(k+2,u)$$

Tables D.1 and D.2 demonstrate the applicability of the approximation in (D.10). The tables contain the ratios of this expression to the numerical integration of (D1). The set of $\mathscr{E}$, $\mathscr{W}$, and α expected in climate simulations are tested. In this range, the error is always less than 0.1%.

Table D.1: Ratio of analytical approximation to numerical integration ($\mathscr{W} = 10\ \mathscr{E}$)

$\mathscr{E}^{-1}$	$\alpha = 1$	$\alpha = 5$	$\alpha = 10$	$\alpha = 25$
0.1	0.998	0.996	0.994	0.991
0.2	0.998	0.996	0.994	0.991
0.3	0.998	0.996	0.994	0.992
0.4	0.998	0.996	0.995	0.992
0.5	0.998	0.997	0.995	0.993
0.6	0.998	0.997	0.995	0.993
0.7	0.998	0.997	0.996	0.995
0.8	0.998	0.997	0.996	0.994
0.9	0.998	0.997	0.997	0.995
1.0	0.998	0.998	0.997	0.996
2.0	0.998	0.999	1.000	1.000
3.0	0.998	0.999	0.999	0.999
4.0	0.998	0.998	0.998	0.998
5.0	0.998	0.997	0.996	0.996
6.0	0.998	0.996	0.995	0.994
7.0	0.998	0.995	0.994	0.993
8.0	0.997	0.994	0.993	0.992
9.0	0.997	0.994	0.992	0.991
10.0	0.997	0.993	0.992	0.990

Table D.2: Ratio of analytical approximation to numerical integration ($\mathscr{W} = 100\ \mathscr{E}$)

$\mathscr{E}^{-1}$	$\alpha = 1$	$\alpha = 5$	$\alpha = 10$	$\alpha = 25$
0.1	0.998	0.995	0.993	0.991
0.2	0.998	0.996	0.994	0.991
0.3	0.998	0.996	0.994	0.991
0.4	0.998	0.996	0.994	0.992
0.5	0.998	0.996	0.995	0.992
0.6	0.998	0.997	0.995	0.993
0.7	0.998	0.997	0.996	0.993
0.8	0.998	0.997	0.996	0.994
0.9	0.998	0.997	0.996	0.995
1.0	0.998	0.998	0.997	0.995
2.0	0.998	0.999	1.000	1.000
3.0	0.998	0.999	1.000	1.000
4.0	0.998	0.999	0.999	0.999
5.0	0.998	0.998	0.998	0.998
6.0	0.998	0.997	0.997	0.997
7.0	0.998	0.997	0.997	0.997
8.0	0.997	0.996	0.996	0.996
9.0	0.997	0.996	0.995	0.995
10.0	0.997	0.995	0.995	0.995

Appendix E: Equilibrium Value and Sensitivity of Soil Moisture in GCM Parameterizations

The water balance at the surface is

$$\frac{\partial w}{\partial t} + Q = P - e \tag{E.1}$$

where

w = vertically integrated soil moisture content,

Q = surface runoff loss,

P = precipitation reaching the surface,

and e = evaporation from the surface.

Climatically, we may write

$$Q = P - e \tag{E.2}$$

The atmospheric component (including the surface boundary layer) in GCMs provide estimates of precipitation P and effective potential evaporation e_p. The landsurface hydrology parameterization then partitions these values into runoff, actual evaporation, and storage change. For GCM models, the empirical expressions used in the partitioning are

$$Q = R\,P \tag{E.3}$$

and

$$e = \beta\, e_p \tag{E.4}$$

where R and β are the runoff and evaporation efficiency functions, with $0 \leq \beta \leq 1$ and $0 \leq R \leq 1$. These efficiency functions depend on the relative soil saturation s, itself $0 \leq s \leq 1$.

Upon the substitution of (E.3) and (E.4) in (E.2),

$$R\,P = P - \beta\, e_p \tag{E.5}$$

Define $\mathcal{P} = \frac{P}{e_p}$ to write

$$\mathcal{P} = \frac{\beta}{1 - R} \tag{E.6}$$

In the GISS soil hydrology parameterization, the functions β and R have simple dependencies on the relative soil saturation s (Hansen et al., 1983). The runoff ratio is

$$R = \frac{1}{2}\, s \tag{E.7}$$

and the evaporation efficiency is parameterized as

$$\beta = s \tag{E.8}$$

Substituting (E.7) and (E.8) in (E.6) and solving for the equilibrium value of s given climate,

$$s = \frac{2\,\mathcal{P}}{\mathcal{P} + 2} \tag{E.9}$$

For comparison, we would like to derive a similar expression for the equilibrium relative soil saturation in the system defined by the landsurface subgrid hydrology parameterization introduced in Chapter II. The problem is, however, that the expressions for R and β in this case are highly nonlinear in s and are furthermore dependent on the variance of rainfall and soil type. For the same mean climatic conditions, if the rainfall variance is increased, more Horton runoff will occur.

Here we will introduce a parameterization for the space–time variability of the mean climate conditions in order to define the expression for the equilibrium soil moisture. The landsurface subgrid hydrology parameterization already contains the fractional wetting parameter κ which represents the fraction of the area actually experiencing rainfall in storms. In time, similarly, we define a fractional wetting. For a given (mean) climatic rainfall rate, we assume that precipitation occurs only a fraction λ of the time. The rainfall intensity during storms is thus equal to the climatic rainfall rate divided by λ. This results in the temporal coefficient of variation

$$cv_P = \sqrt{\lambda^{-1} - 1} \tag{E.10}$$

for rainfall.

Figure E.1 graphically depicts the parameterization of space–time variability in rainfall when the climatic rate is known. The space–time variability affects the runoff parameterization only. There, the storm rainfall intensity is represented through the dimensionless measure

$$I = \frac{K(1)}{E[P]} \tag{E.11}$$

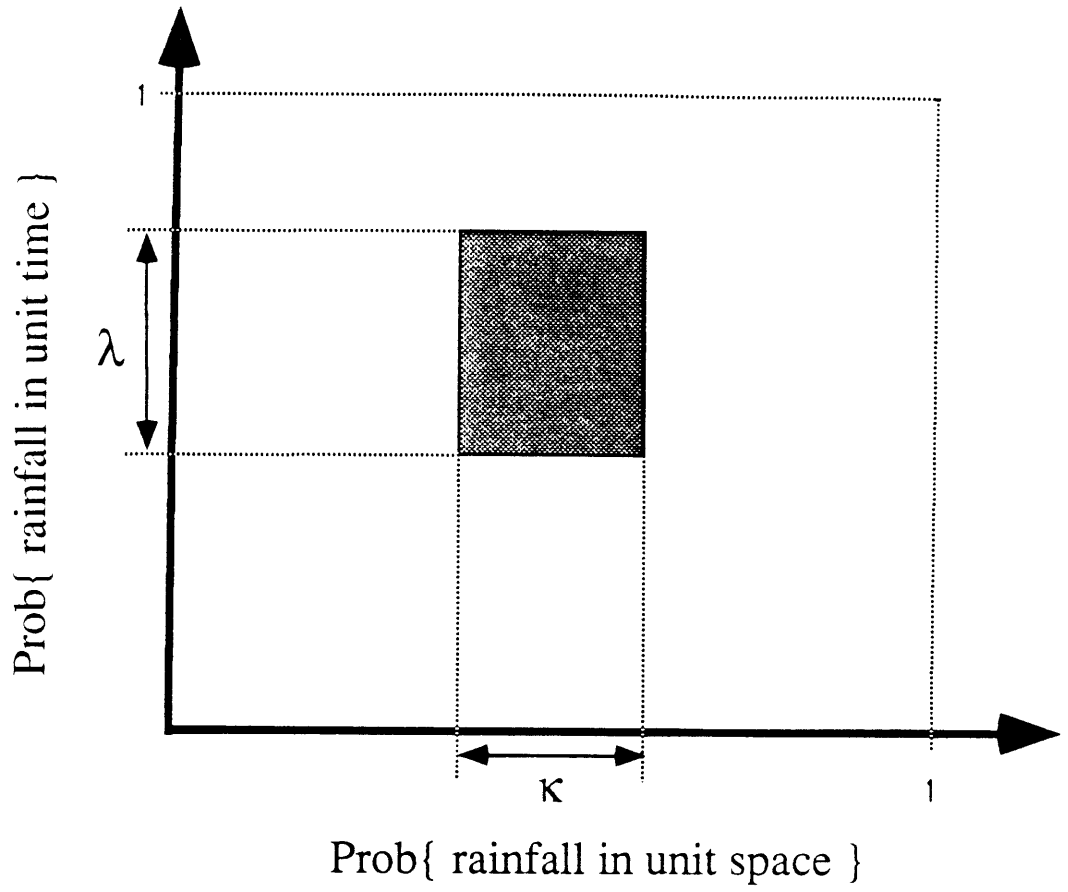

Fig. E.1 Schematic of procedure for scaling mean rainfall value to its event intensity level

where K(1) is the saturated soil hydraulic conductivity and E[P] is the mean storm rainfall rate. In the expression for the runoff ratio R, I is accompanied by κ, i.e. κI everywhere. For the application here, we now simply have $\lambda\kappa$I in the expression for runoff ratio. The denominator of (E.11) now represents the climatic rainfall rate.

The runoff ratio is functionally

$$R = R\ (\ \lambda\kappa I\ ,\ E[s]\ ,\ cv\ ;\ \text{soil type}\ ) \tag{E.12}$$

where E[s] and cv are the spatial mean and coefficient of variation associated with the surface soil relative saturation.

The bare soil evaporation efficiency (β_s) is dependent on E[s], e_p, and soil type. The dependency on e_p appears through the dimensionless soil–climate parameter

$$\mathscr{E} = E[s] \left[\frac{K(1)}{e_p}\,\Omega \right]^{\frac{2m}{1+4m}} \tag{E.13}$$

where Ω and m are soil parameters. We may write (E.13) as

$$\mathscr{E} = (\ \mathscr{P}\ I\ \Omega\ )^{\frac{2m}{1+4m}} \tag{E.14}$$

which results in the functional expression

$$\beta_s = \beta_s\ (\ I\ ,\ \mathscr{P},\ E[s]\ ,\ cv\ ;\ \text{soil type}\ ) \tag{E.15}$$

With (E.6), (E.12), and (E.14) we have the following expression for the equilibrium

relative soil saturation

$$\mathscr{P} = \frac{\beta_s(\mathrm{I}\,,\,\mathscr{P},\mathrm{E[s]}\,,cv;\text{soil type})}{1 - \mathrm{R}(\lambda\kappa\mathrm{I},\mathrm{E[s]},cv;\text{soil type})} \tag{E.16}$$

which is highly nonlinear in both E[s] and $\mathscr{P}$.

For a sandy soil and $\lambda\kappa = 0.25$, we plot the equilibrium relative soil saturation versus $\mathscr{P}$ for various values of I (Figures E.2 and E.3). Superposed on these figures is the equilibrium relative soil saturation defined by the GISS soil hydrology (Equation (E.9)). Figures E.2 and E.3 represent $cv = 1$ and $cv = \frac{1}{2}$ respectively.

As evident in Figure E.2, higher relative soil saturations are characteristic of climates with large $\mathscr{P}$, i.e. humid climates. Increasing values of I reflect less mean precipitation and thus lower soil moisture. In Figure E.3, there is a sharp shift in the equilibrium relative soil saturation behavior with respect to $\mathscr{P}$ and I at $\mathscr{P} = 1$. With less spatial variability in surface soil moisture (low cv), the climatic transition from a water–limited to a climate–controlled evaporative regime is abrupt. This is evident in Figure 2.10. There, at low values of cv, β_s is virtually a unit delta function at $\mathscr{E} = 1$. In Figure 3 here, near $\mathscr{P} = 1$ the evaporative regime transitions from a water limited to a climate–controlled behavior. Above $\mathscr{P} = 1$, the climate–controlled evaporation efficiency is unity. For these values of $\mathscr{P}$, the equilibrium relative surface soil saturation is simply proportional to $\mathscr{P}$.

As evident in Figures E.2 and E.3, the rainstorm intensity has a significant influence on the equilibrium relative soil saturation. Depending on the actual realization of I and $\mathscr{P}$, the equilibrium relative soil saturation resulting from the GISS hydrology and the landsurface subgrid hydrology parameterization can differ substantially.

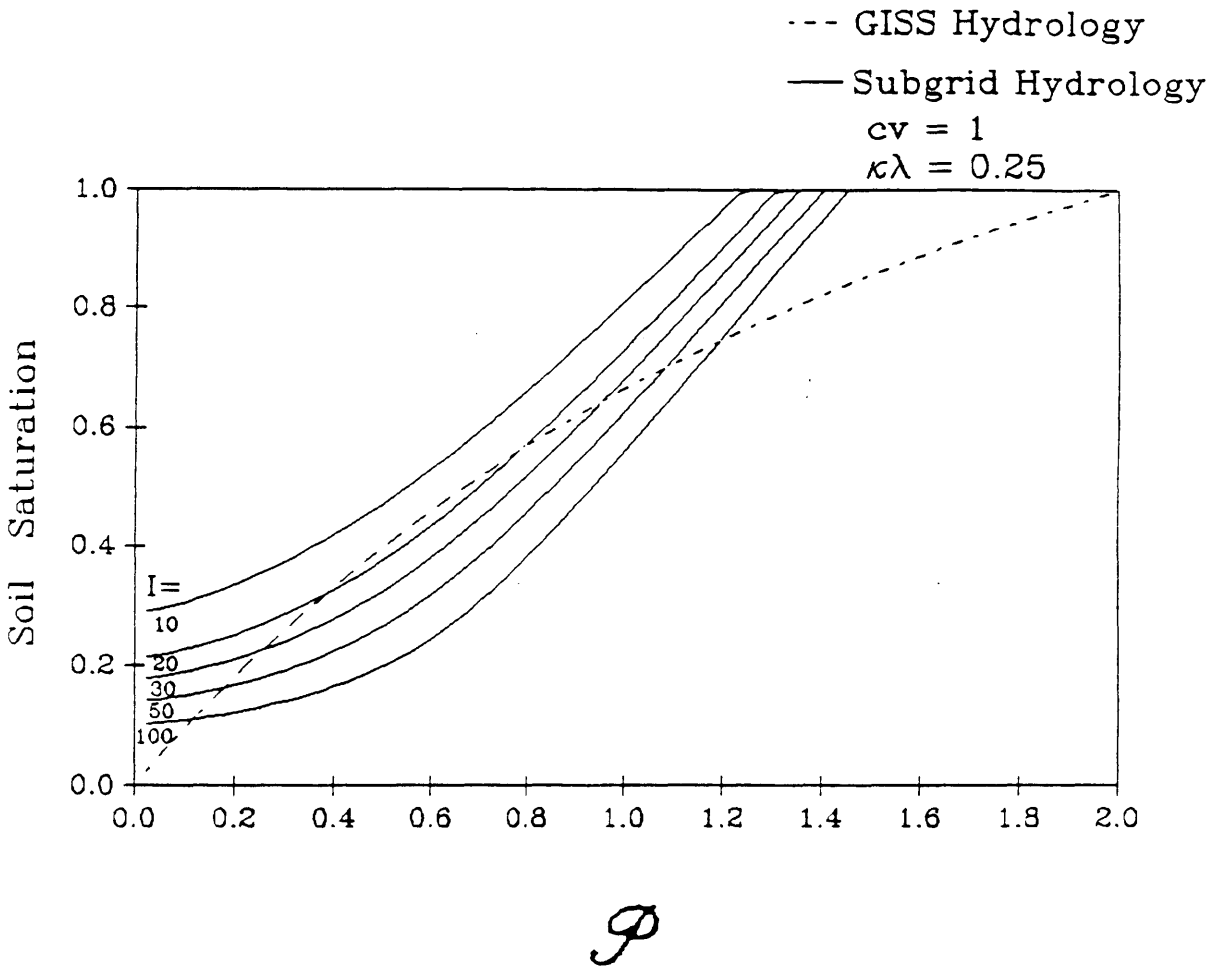

Fig. E.2 Equilibrium relative soil saturation dependence on the climatic parameter $\mathcal{P}$ for both the GISS soil hydrology and the subgrid hydrology parameterization with $cv = 1$ and a light textured bare soil

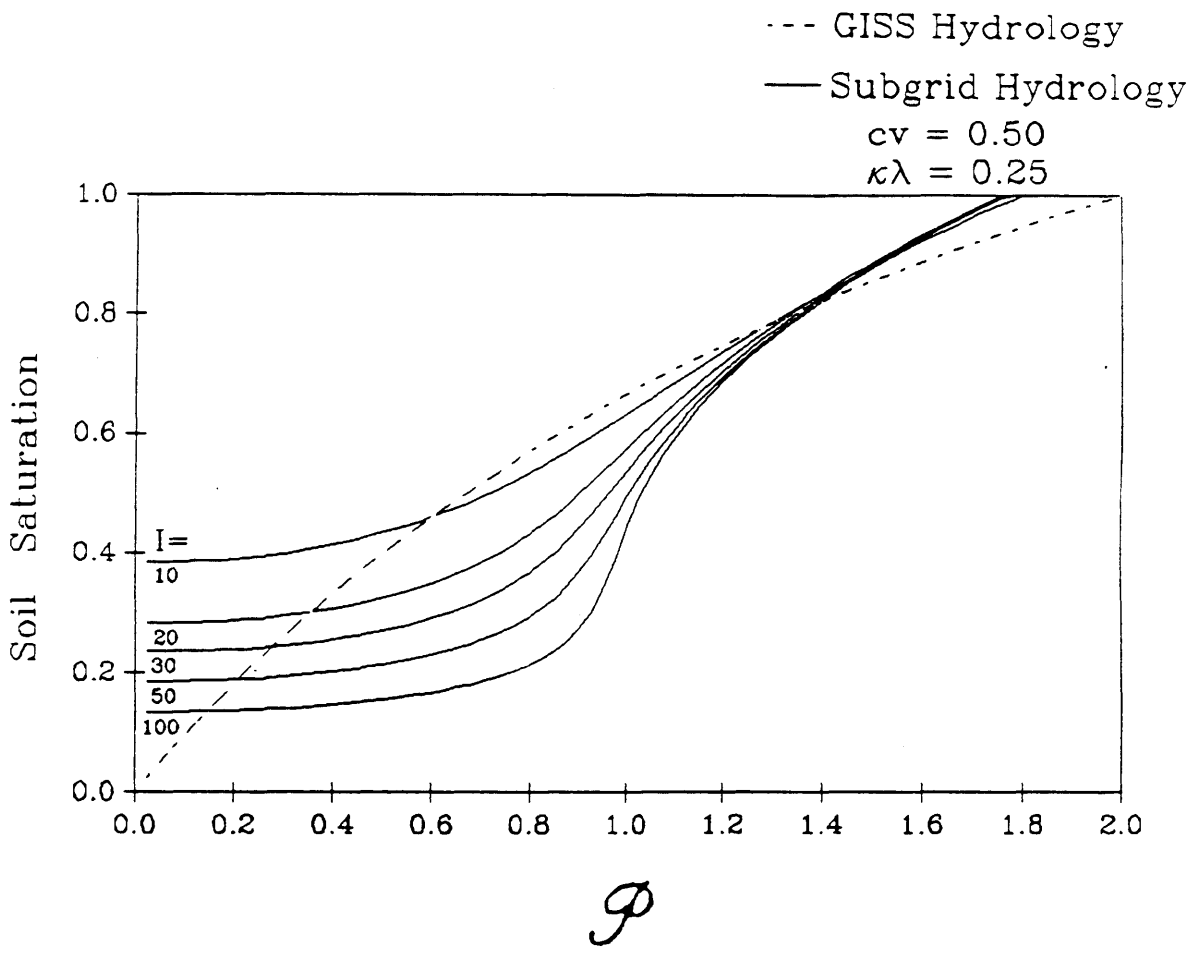

Fig. E.3 Equilibrium relative soil saturation dependence on the climatic parameter $\mathscr{P}$ for both the GISS soil hydrology and the subgrid hydrology parameterization with $cv = 1/2$ and a light textured bare soil

There are, of course, numerous landsurface–atmosphere feedbacks that are not represented in this analysis. These processes are critical in establishing the equilibrium relative soil saturation. The simulation studies with the simple screening climate model address some of these issues.

One of the major feedbacks in the landsurface–atmosphere system is the potential evaporation feedback. As the landsurface dries, the latent heat flux due to surface evaporation diminishes. The excess energy goes towards greater sensible heat flux and raised surface temperatures. The effective potential evaporation rate will thus increase.

Below, we will provide a first–order approximation to this process and derive the analytic expression for the equilibrium relative soil saturation for the GISS soil hydrology in this context. When we normalize the precipitation rate P by the potential evaporation rate resulting from including the basic feedbacks, the new dimensionless variable $\mathcal{P}$ will be a climatic property and virtually independent of s. In this manner we can examine the sensitivity of the GISS soil hydrology to climate change.

The dependence of e_p on s may be removed by defining the climatic potential evaporation ($\bar{e}_p$) which is the evaporation rate if the entire landsurface is under the climate–controlled evaporative regime and water is nowhere limiting. When water is limiting over a portion of the surface and evaporation occurs below the potential, an amount of energy

$$q = \lambda \bar{e}_p - \lambda e \qquad \text{(E.17)}$$

becomes available to increase the evaporative demand. This amount of energy goes towards increasing the effective potential evaporation (e_p) at the surface, i.e.

$$\lambda e_p = \lambda \bar{e}_p + q$$
$$= 2\,\lambda \bar{e}_p - \lambda e$$

or

$$e_p + e = \bar{e}_p \tag{E.18}$$

Again substitute (E.4) in (E.18),

$$e_p\,(\,1 + \beta\,) = 2\,\bar{e}_p$$

or

$$e_p = \frac{2}{1\,+\,\beta}\,\bar{e}_p \tag{E.19}$$

Substitute (E.19) in (E.6) to obtain

$$\mathscr{P} = \frac{2\beta}{(1+\beta)\,(1-R)} \tag{E.20}$$

Now the l.h.s. is a climatic parameter truly independent of s. The climatic potential evaporation rate $\bar{e}_p$ is mostly a function of temperature now.

With the GISS soil hydrology (Equations (E.7) and (E.8)) we find

$$\mathscr{P} = \frac{2\,s}{(\;1\,+\,s\;)\;(\;1\,-\,\frac{1}{2}\,s\;)} \tag{E.21}$$

This is also the quadratic

$$(-\tfrac{1}{2}\mathcal{P})\,s^2 + (\tfrac{\mathcal{P}}{2} - 2)\,s + \mathcal{P} = 0 \qquad \text{(E.22)}$$

with the solution

$$s = (\tfrac{1}{2} - \tfrac{2}{\mathcal{P}}) \pm \sqrt{(\tfrac{1}{2} - \tfrac{2}{\mathcal{P}})^2 + 2} \qquad \text{(E.23)}$$

Regions of solution will be analyzed in terms of subsets of $\mathcal{P}$.

All $\mathcal{P} \leq 0$ is infeasible since both P and $\bar{e}_p$ are non–negative.

When $0 \leq \mathcal{P} \leq 2$, $(\tfrac{1}{2} - \tfrac{2}{\mathcal{P}}) \leq -\tfrac{1}{2}$ and for s to remain non–negative, only the + of ± is feasible.

When $2 \leq \mathcal{P} \leq 4$, the – of the ± solution is feasible since here $-\tfrac{1}{2} \leq (\tfrac{1}{2} - \tfrac{2}{\mathcal{P}}) \leq 0$ and $s \geq 0$. The taking the + of the ± solution, evaluate $s = 1$ at $\mathcal{P} = 2$. Also $s = \sqrt{2}$ at $\mathcal{P} = 4$. Requiring that $s \leq 1$ thus eliminates the possibility of feasible solutions in this subset of $\mathcal{P}$.

When $\mathcal{P} \geq 4$, $0 \leq (\tfrac{1}{2} - \tfrac{2}{\mathcal{P}}) \leq \tfrac{1}{2}$ and $\sqrt{2} \leq \sqrt{(\tfrac{1}{2} - \tfrac{2}{\mathcal{P}})^2 + 2} \leq \tfrac{3}{2}$. Clearly the + of the ± solution is infeasible when $s \leq 1$. Also with $0 \leq s$ and $\tfrac{1}{2} < \sqrt{2}$, the – of the ± solution pair is also infeasible with $\mathcal{P} \geq 4$.

In summary, the GISS GCM landsurface hydrology parameterization has an inherent climatic solution for soil moisture that uniquely depends on the climatic parameter $\mathcal{P}$. The solution is

$$s = (\tfrac{1}{2} - \tfrac{2}{\mathcal{P}}) + \sqrt{(\tfrac{1}{2} - \tfrac{2}{\mathcal{P}})^2 + 2} \qquad \text{(E.24)}$$

with

$$0 \leq \mathcal{P} \leq 2$$

Sensitivity of the relative soil saturation to climatic shifts in $\mathcal{P}$ may now be analyzed through the dimensionless elasticity measure $\mathcal{L}$

$$\mathcal{L} = \frac{\mathcal{P}}{s} \frac{\partial s}{\partial \mathcal{P}} \tag{E.25}$$

which gives the percent change in soil moisture due to the percent change in $\mathcal{P}$. Using (E.24) in (E.25) we write

$$\frac{\partial s}{\partial \mathcal{P}} = \frac{2}{\mathcal{P}^2} \left[1 + \frac{\left(\frac{1}{2} - \frac{2}{\mathcal{P}} \right)}{\sqrt{\left(\frac{1}{2} - \frac{2}{\mathcal{P}} \right) + 2}} \right] \tag{E.26}$$

The elasticity measure $\mathcal{L}$ is plotted versus the climatic variable $\mathcal{P}$ in Figure E.4.

The elasticity measure defines the percent change in soil saturation due to percent change in $\mathcal{P}$. At low values of $\mathcal{P}$(more arid climates), there is a nearly one–to–one sensitivity of s to $\mathcal{P}$. This sensitivity is significantly reduced for higher values of $\mathcal{P}$characteristic of more humid climates.

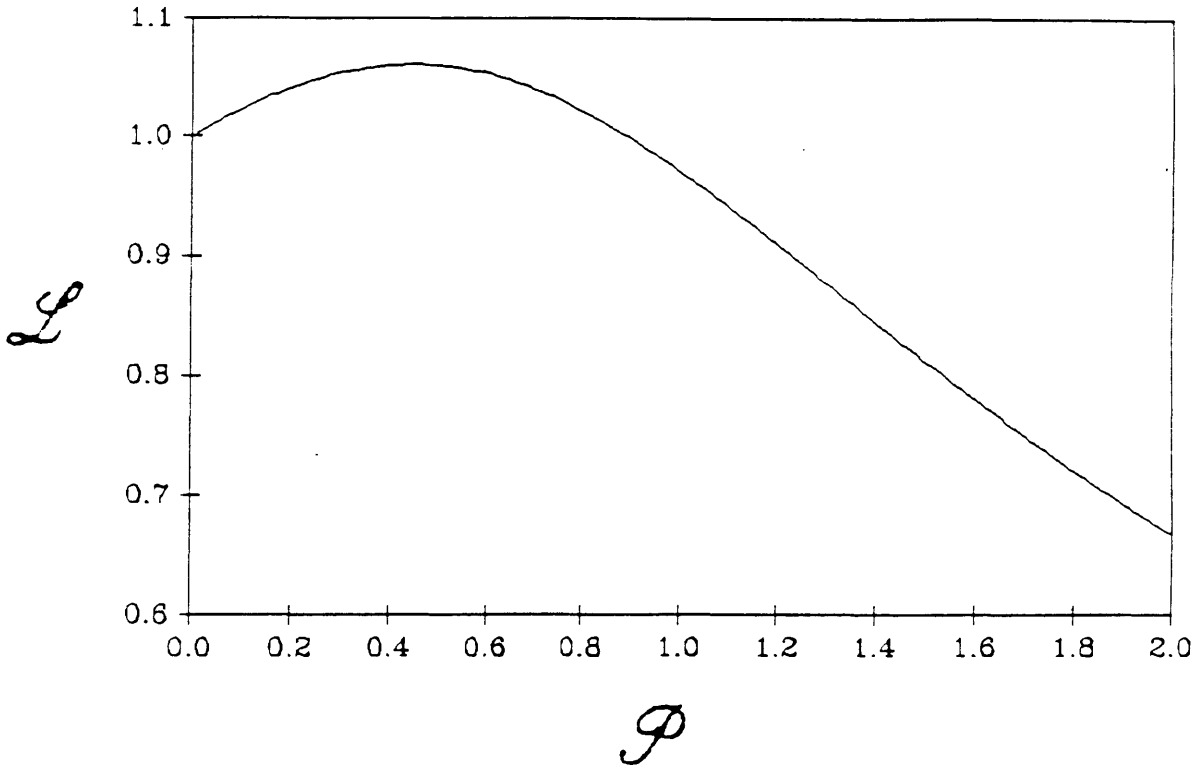

Fig. E.4 Soil saturation elasticity with respect to the climate parameter $\mathscr{P}$ for the GISS soil hydrology model

APPENDIX F: Outline of the screening model computer code

The computer program for the screening model contains over 3600 lines of standard FORTRAN code. It has been compiled and executed with the VAX/VMS FORTRAN Compiler. On a MicroVAX–II, each simulation experiment in series I and J (250 diurnal cycles; Δt_{rad} = 3 hours) requires nearly 7 hours of processor time. Since the radiation module is the chief consumer of CPU in the screening model, the processor time is approximately proportional to Δt_{rad}.

Figure F.1 illustrates the basic outline of subroutine call sequences for the highly modularized computer code. A listing of the module locations in various files is contained in Table F.1. The key parameters that are required in simulations with the screening model are listed in Table F.2. Those variables defined in the Main Program are located in the MOD_PARAMETERS.FOR file that is compiled, along with all the remaining independent files, using the *INCLUDE 'file.name'* command.

The FORTRAN code is stored on magnetic tape and may be obtained through the Ralph M. Parsons Laboratory.

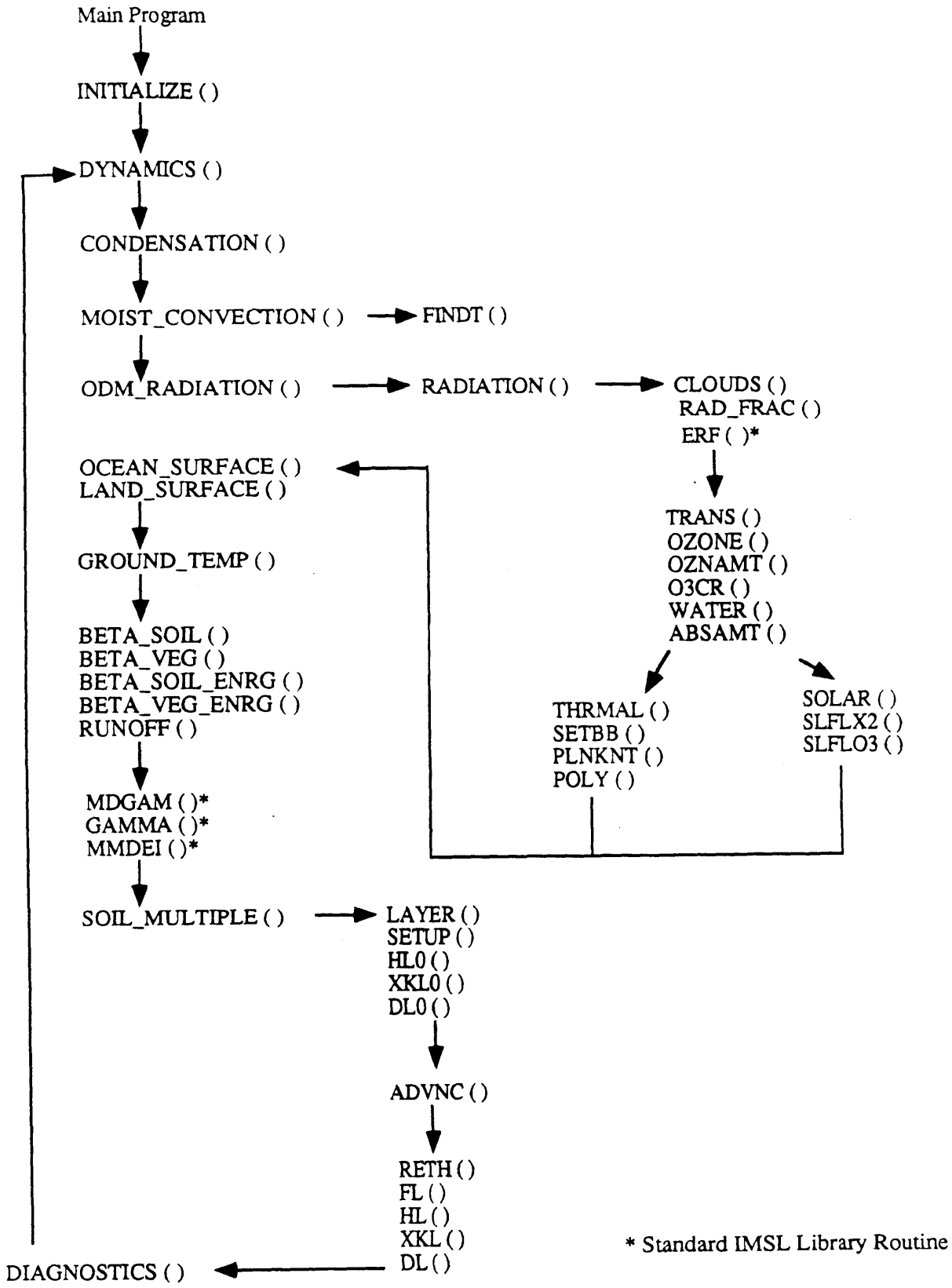

Fig. F.1 Outline of the sequence in subroutine calls in the screening model

Table F.1: Program directory and subroutine contents for the screening model

File Name	Subroutines
CYLINDER.FOR	Main Program
MOD_COMMON.FOR	COMMON
MOD_CONDENSATION.FOR	CONDENSATION ( )
MOD_DIAGNOSTICS.FOR	DIAGNOSTICS ( )
MOD_DYNAMICS.FOR	DYNAMICS ( )
MOD_INITIAL.FOR	INITIALIZE ( )
MOD_LAND_MULT.FOR	LAND_SURFACE ( )
MOD_LAND_SUBGRID.FOR	LAND_SURFACE ( )
MOD_LAND_SURFACE.FOR	LAND_SURFACE ( )
MOD_MOIST_CONVECT.FOR	MOIST_CONVECTION ( )
MOD_MOIST_THERMO.FOR	FINDT ( )
MOD_OCEAN_SURFACE.FOR	OCEAN_SURFACE ( )
MOD_PARAMETERS.FOR	Parameters of CYLINDER.FOR
MOD_RADIATIONW.FOR	ODM_RADIATION ( )
MOD_SUBGRID_COMMON.FOR	COMMON/SUBGRID/
MOD_TG.FOR	GROUND_TEMP ( )
MOD_SUBGRID.FOR	BETA_SOIL ( ), BETA_VEG ( ), RUNOFF ( ), BETA_VEG_ENRG ( ), BETA_SOIL_ENRG ( ), SI_GAMMA ( )
RAD_ABSAMT.FOR	ABSAMT ( )
RAD_CALENDER.FOR	TAU ( ), MON_CONV ( )
RAD_CLOUD.FOR	CLOUD ( )
RAD_CO2EM.FOR	CO2EM ( )
RAD_FRAC.FOR	CLOUD_FRAC ( )
RAD_MAIN.FOR	RADIATION ( )
RAD_O3CR.FOR	O3CR ( )
RAD_OZNAMT.FOR	OZNAMT ( )
RAD_OZONE.FOR	OZONE ( )
RAD_PLNKT.FOR	PLNKNT ( )
RAD_POLY.FOR	POLY ( )
RAD_RELHM.FOR	RELHUM ( )
RAD_SETBB.FOR	SETBB ( )
RAD_SLFX2.FOR	SLFX2 ( )
RAD_SLFXO3.FOR	SLFX3 ( )
RAD_SOLAR.FOR	SOLAR ( )
RAD_SPEC.DAT	Spectral Data
RAD_THERMAL.FOR	THRMAL ( )
RAD_TRANS.FOR	TRANS ( )
RAD_WATER.FOR	WATER ( )

File Name	Subroutines ...continued
SOIL_FUNCTION.FOR	SOIL_FUNCTION ( )
SOIL_ADVANCE.FOR	ADVNC ( )
SOIL_DL.FOR	DL ( )
SOIL_DL0.FOR	DL0 ( )
SOIL_FL.FOR	FL ( )
SOIL_HL.FOR	HL ( )
SOIL_HL0.FOR	HL0 ( )
SOIL_LAYER.FOR	LAYER ( )
SOIL_MULTIPLE.FOR	SOIL_MULTIPLE ( )
SOIL_RETH.FOR	RETH ( )
SOIL_SETUP.FOR	SETUP ( )
SOIL_XKL.FOR	XKL ( )
SOIL_XKL0.FOR	XKL0 ( )
SOIL_COMMON.FOR	COMMON/HYDRAULICS/, COMMON/BC/, COMMON/FLUX/

MATH_GAMMA.FOR	GAMMA ( )
MATH_MDGAM.FOR	MDGAM ( )
MATH_ERF.FOR	ERF ( )
MATH_MMDEI.FOR	MMDEI ( )

Table F.2: Listing and location of key screening model parameters

Variable	Location	Description [Units]
NSIM	Main Program	Duration of simulation [Hours]
INITC	Main Program	Hour to begin diagnostics collection [Hours]
LAT	Main Program	Latitude [Deg.]
JUL	Main Program	Julian day for perpetual simulation
FILE_NAME	Main Program	Name of diagnostics output file
TAUFRAC	Main Program	Parameter χ in exchange scheme [days]
FIX	Main Program	Logical variable for active/fixed ocean SST
DIFFUSION	Main Program	Logical variable for present GISS 2nd soil layer
SD	RAD_FRAC	Parameter σ_c in cloud model [^oC]
GDEPTH	INITIALIZE	Depth of surface soil layer [meters]
SDEPTH	INITIALIZE	Depth of surface ocean layer [meters]
SST	INITIALIZE	Fixed or initial ocean temperature [^oK]
NSURF	OCEAN_ & LAND_SURFACE	Number of minor time steps in module
ZS	OCEAN_ & LAND_SURFACE	Height of surface air layer [meters]
Z1	OCEAN_ & LAND_SURFACE	Height of first atmospheric level [meters]
Z0	OCEAN_ & LAND_SURFACE	Roughness height of surface [meters]
VS	OCEAN_ & LAND_SURFACE	Surface wind speed [meters sec^{-1}]
DHOUR	ODM_RADIATION	Δt_{rad} parameter [hours]
WGT(3)	SOIL_FUNCTION	Fraction Sand/Silt/Clay composition of soil
N	LAYER	Number of soil layers
ZB(N)	LAYER	Depth of soil layer surface [meters]